Establishment of a Test System for an Optogenetic Biohybrid Cochlear Implant

von der Fakultät für Mathematik und Physik

der Gottfried Wilhelm Leibniz Universität Hannover zur Erlangung des Grades

Doktor der NATURWISSENSCHAFTEN

Dr. rer. nat.

genehmigte Dissertation von

M.Sc. Patrick Heeger

Erscheinungsjahr 2021

Referent:	**Prof. Dr. Alexander Heisterkamp**
Koreferentin/Koreferent:	**Prof. Dr. med. Athanasia Warnecke**
	Prof. Dr. Holger Lubatschowski
Prüfungsvorsitz:	**Prof. Dr. Rolf Haug**
Tag der Promotion:	**03.09.2021**

This Work was funded by:

Deutsche Forschungsgemeinschaft (DFG, German Research Foundation) under Germany's Excellence Strategy – EXC 2177/1 - Project ID 390895286

Table of Content

Table of Content

Table of Content

List of Figures

List of Figures

List of Tables

Abbreviations

ATP	adenosine triphosphate
AuCS	gold-coated coverslips
ChR2	Channelrhodopsin-2
CI	cochlear implant
CMV	cytomegalovirus
CN	cortical neurons
ECM	extracellular matrix
FRET	Förster (or fluorescence) resonance energy transfer
GECI	genetically encoded calcium indicator
GEVI	genetically encoded voltage indicator
GFP	green fluorescent protein
HC	hippocampal neurons
hPSC	human pluripotent stem cell
Laser	light amplification of stimulated emission of radiation
LED	light-emitting diode
MEA	Multi-electrode array
MOI	multiplicity of infection
mPEG	poly(ethylene glycol) methyl ether thiol
MPM	multiphoton microscopy
NA	numerical aperture
PAA	polyacrylamide
ROS	reactive oxygen species
RyR	ryanodine receptors
SGN	spiral ganglion neurons

Abstract

The cochlear implant is the world's most successful neuroprosthetic device. The electrode directly stimulates the spiral ganglion neurons (SGN), the first neurons in the auditory system, in the cochlea at different places, which corresponds to a different characteristic frequency. A limiting performance factor of an electric cochlear implant (eCI) is the crosstalk of channel-interaction due to spread of excitation, resulting in poor speech perception in background noise and difficulty appreciating complex sounds such as music. An optical cochlear implant (oCI) may overcome these limitations, as light can be focused much more precise to activate a narrow band of SGNs.

This thesis presents a novel way of stimulating SGNs via a neuronal-tandem trigger approach, which was developed during this thesis. Inter-neuronal communication between spiral ganglion neurons and neurons of other functional units, in this case cortex neurons (CN) and hippocampus neurons (HN) is probed via an all-optical system, consisting of a blue-shifted channelrhodopsin variant (CheRiff) with a genetically encoded calcium indicator, namely jRCaMP1a, which has its emission spectra in the red light range. This enabled for simultaneous optical stimulation and recording from spatially separated small neuronal populations.

A manipulation LED was fixed directly above either a *CheRiff* transduced HN or a CN population. Three spots per population were stimulated with four different pulse durations (10 ms; 100 ms; 250 ms; 500 ms). Each recording consisted of 10 pulses of blue light separated by an interval of 5.5 s. Simultaneously, calcium imaging with continuous green light illumination (570 nm, 15 mW/cm^2) was performed.

The stimulation of SGNs via a neuronal-tandem approach was possible for the first time with both optogenetic manipulated HNs and CNs respectively. SGNs (that are not transduced with *CheRiff*) are activated when nearby populations of cortical or hippocampal cultured neurons are stimulated with light, indicating that the neurons of different origin are inter-connected and communication takes place between them. Another observation made was, that the stimulation efficiency of the SGNs generally increased with the stimulation length and reached a plateau at 250 ms, whereas longer stimulation pulses did not result in stronger calcium signals. This fact could indicate an effect called excitotoxicity. Further, a structured cell growth system based on gold-coated coverslips (AuCS) and poly(ethylene glycol) methyl ether thiol (mPEG) was established, to enable spatially directed signal generation. The mPEG generate a cell repellent surface on the AuCS and laser irradiation generates the specified direction of growth. First optogenetic stimulation experiments with HL-1 ChR2 cells showed propagating calcium waves

after LED irradiation within the designated structure, pointing out the great reliability of this method. Together, the neuronal-tandem approach developed during this thesis could pave the way to a completely new type of an oCI.

Keywords: Optogenetics, Neuroprosthesis, Cochlear Implant, Cell Communication

1 Introduction

1.1 Neurobiology – From Identification of Neurons to Probing Whole Neuronal Networks with Optogenetics

As early as 1872, the physiologist Camillo Golgi discovered individual neurons using silver nitrate staining. He claimed that neurons are forming a coherent network of fused cells, a so-called syncytium[1]. Fifteen years later, the Spanish physician Santiago Ramón y Cajal came to a different conclusion using the same method. He postulated that the brain consists of individual functional units that are connected but not fused with one another. Ultimately, Cajal was right and his efforts had laid the groundwork of modern neurobiology. Today, he is still known for his fascinating drawings of nerve cell preparations (**Fig. 1**) from that time[2].

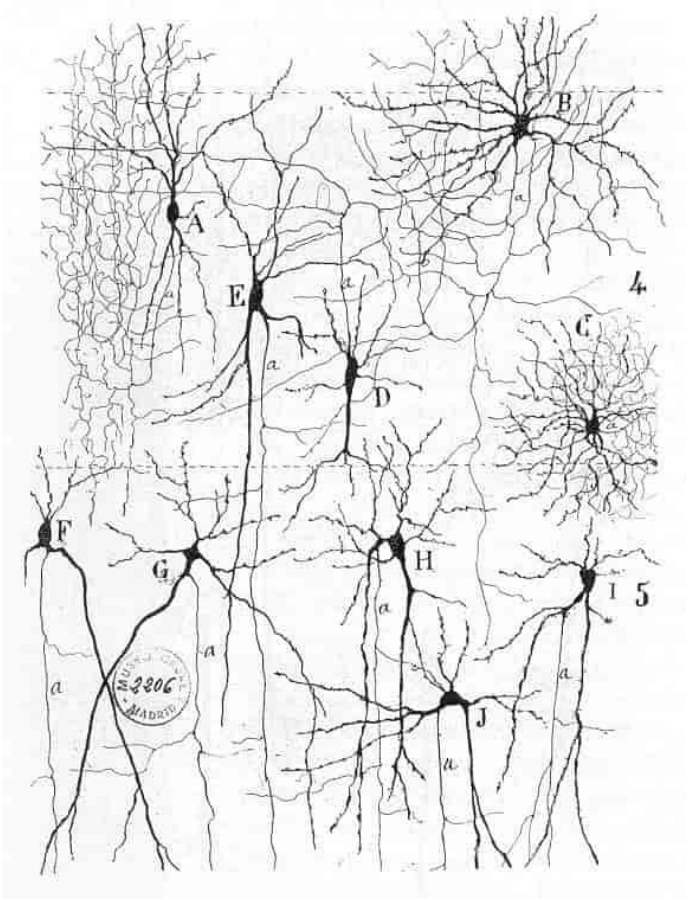

Fig. 1 Fine structures of the nervous system drawn by Santiago Ramón y Cajal

Illustration from Santiago Ramon y Cajal's "Texture of the Nervous System of Man and the Vertebrates", Santiago Ramon y Cajal, 1898. Central nervous system neurons were treated with a silver-nitrate solution, a histological staining technique.

In order to understand the complexity of the brain, multiple scales like molecular, subcellular, and cellular levels have to be taken into account. In addition, the large-scale level of neuronal populations and macroscopic regions up to behavior studies needs to be considered. In 2013, a European initiative "The Human Brain Project" started with the aim to decode the multilevel complexity of the human brain. It combines empirical neuroscience, information and communication technology (ICT), big data analytics, artificial intelligence (AI), and simulation[3]. The HBP already led to huge breakthroughs for example in understanding the neural basis of spatial memory[4], consciousness and sleep[5], perception and learning[6], and multisensory integration[7]. This highlights, exploring the brain on a multilevel scale opens new insights toward a better understanding of the brain's complexity.

Great efforts are also being made within a project called "The Human Connectome Project"[8] to investigate the totality of connections in the nervous system of healthy adults. The purpose is to acquire and share data about the functional and structural connectivity and variability of the human brain. Multiple noninvasive imaging modalities, for example, diffusion imaging (dMRI) for myelin and structural mapping, plus combined magnetoencephalography and electroencephalography (MEG/EEG) along with extensive genetic and behavioral data are used to achieve this ambitious goal[9]. The HPC has already provided data and discoveries that greatly enhance our understanding of the human brain structure, function, connectivity, and their relationships to behavior. Many new neuroimaging methods have emerged from this, including the Lifespan HCP[10] to examine brain circuits across the human lifespan and "Connectomes Related to Human Disease" projects[11] mapping patterns of diseases or disorders affecting the brain, for example, epilepsy, depression, or Alzheimer's disease.

These projects are vital in understanding the structure and activity of the human brain or how these networks are altered in the brain affecting diseases and helping to develop new treatments[12]. However, to gain a better insight into how multiple neurons in heterogeneous neuronal networks communicate with each other, it is often crucial to understand the underlying activity of those on single-cell level. For this, a culture system enabling both simultaneous stimulation and recording from large populations of neurons with single cell readout is the way to go. Optogenetics, in combination with calcium imaging, is a powerful tool enabling contact-free manipulation of specific neurons or defined regions and simultaneous readout of stimulated and non-stimulated neurons[13,14]. This is possible through the use of channelrhodopsin (ChR) and genetically encoded calcium indicators (GECI) or genetically encoded voltage indicators (GEVIs) variants with a non-overlapping excitation spectrum[15]. Moreover, GECIs or GEVIs

offer the possibility to target different types of neurons in co-culture systems by using specific promoters. This allows studying neuronal networks with the ability to selectively stimulate different subtypes of neurons or distinct populations within a network and gives the opportunity to investigate them in a new way. Since calcium imaging only provides indirect secondary signals, it would be best to combine it with voltage recordings. This would allow insights into key cellular processes, like activity-dependent transcription regulation in neurons[16] and synaptic plasticity[17]. However, voltage imaging comes along with high demands on technology and expertise speaking of multimodal readout, versatility, data acquisition, and more. It requires for example a high frame-rate scientific camera. High frame-rate leads to shorter exposure time, meaning that a camera used for voltage imaging must also have high sensitivity, in order to capture significant signals from GEVIs[18]. Though, there are attempts to enable calcium and voltage recordings while optogenetic stimulation at the same time[19]. The advantages and disadvantages of voltage and calcium imaging are explained in more detail in chapter 2.3

Not only the connectivity of neuronal networks can be probed with optogenetics, but optical stimulation might also provide a promising attempt for prosthetics like cardiac pacemakers[20] or cochlear implants (CIs)[21]. The conditions for the neural restoration of function in disorders like epilepsy[22], retinal degeneration[23], and deafness[24] have never been so promising before. Especially the optogenetic stimulation of the cochlea promises significant improvements for the CI user since the optogenetic toolbox nowadays allows cell-type specific neuronal control with high temporal and spatial precision to activate the auditory neurons within smaller tonotopic ranges as traditional electrically stimulating CIs (eCIs)[25]. However, in order to make the SGNs within the cochlea sensitive to light, they need to be genetically modified. Today, the method of choice for transducing SGNs is the local administration of non-pathogenic adeno-associated virus (AAV). However, transduction of SGNs has proven particularly challenging since the expression of the opsins is usually limited to a small number of neurons. Thus, to be functional, an optogenetically driven CI would require high expression levels along the cochlear axis[26].

To overcome this limitation, one could think about coupling already optogenetic activated neurons of other functional units, like the brain, to SGNs. A hydrogel would serve as a carrier providing all the nutrients and growth factors, like brain-derived neurotrophic factor (BDNF), needed for the neurons together with an optical fiber (**Fig. 2**). The growth factors should stimulate growth of residential SGNs towards the implant and thus to the neurons, facilitate the

connection of the different neurons. This way, a new sort of biohybrid CI could be engineered without direct genetic manipulation of the auditory nerve.

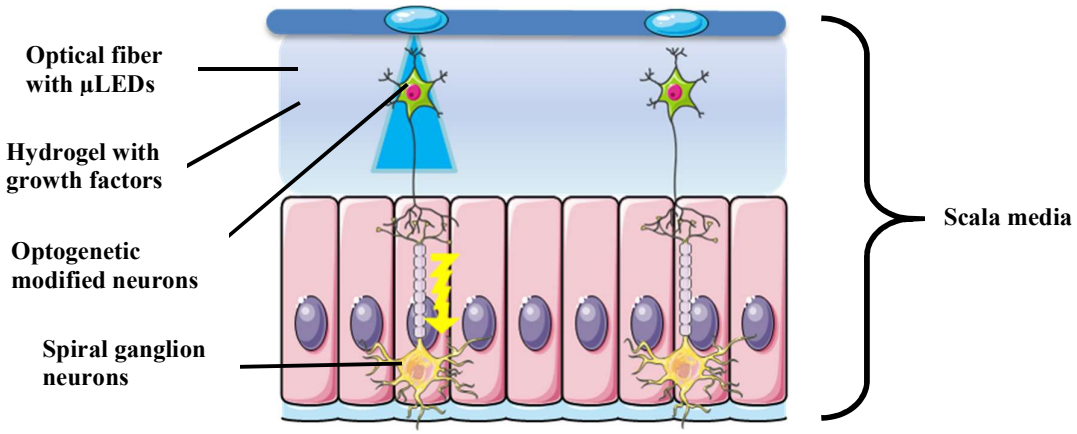

Fig. 2 Schematic drawing of the Biohybrid Cochlear Implant „The living CI“

Optogenetic active trigger neurons (green neurons) embedded in a hydrogel will be implanted along with an optical fiber into the cochlea, for example by directly injecting the cells into the scala media. The hydrogel serve as a carrier providing nutrients and growth factors needed for the neurons. The growth factors facilitate the connection between the implanted neurons and the SGNs (yellow neurons). µLEDs deliver the light to the trigger neurons and the resulting signal propagates to the residential SGNs (yellow flash).

1.2 Hypothesis and Work Plan

First ideas for biohybrid cochlear implants with releasing protective factors for SGN survival have already been published[27]. A biohybrid implant as discussed in this thesis would come with several advantages over conventional optical cochlear implant attempts. The critical step for delivering the opsin of choice to the patient by viral vectors would no longer be necessary and critical growth factors for SGN survival, (like BDNF) could be delivered right away within the carrier matrix (e.g. a hydrogel).

In order to make this kind of new biohybrid cochlear implant possible, one would first have to develop a simple trigger response system to probe the communication of single neuronal populations of different functional units like the brain and the cochlea. More precisely, is the communication between SGNs and brain-derived cells, in this case hippocampal (HNCs) and cortical neurons (CNs), possible and thus stimulation of the SGNs via optogenetically activated HNCs and CNs? Next, is it possible to achieve more reliable results by letting the neurons grow in predetermined structures? In addition, can we specify the direction of signals with this? Within this work, an all-optical, easily adaptable, cost-effective, and reliable optogenetic sensing and actuation test system to probe the spread of excitation in inter-neuronal networks shall be developed.

To establish such an all-optical system, the following steps are necessary:

- **Establishment of an Optogenetic Stimulus-Response System**
  A setup needs to be established to make the stimulation of cell populations through optogenetics and simultaneous readout by calcium imaging possible. Various constructs are to be tested, like a combination of a blue-shifted channelrhodopsin variant (CheRiff) and a genetically encoded red-shifted calcium indicator (jRCaMP1a). In this way, a spectrally independent stimulation and readout should be achieved.

- **A Neuronal-Tandem Approach to stimulate Spiral Ganglion Neurons**
  This all-optical stimulus-response system will further be applied on spatially separated primary neuronal populations to generate an optogenetic neuronal-tandem system. Optogenetic activated hippocampal and cortical neurons will serve as trigger-neurons and co-cultured with spiral ganglion neurons, carrying jRCaMP1a. The communication among these distinct neurons examined through light stimulation experiments.

- **Structured Cell Growth for directional Signal Transmission**
  In parallel a separation approach of cell populations by gold nano layers will be developed. A gold nano layer is sputtered on a glass surface. This layer will be treated with a poly(ethylene glycol) methyl ether thiol (mPEG) to generate a cell repellent surface. First cell adhesion experiments with HL-1 cells to examine the feasibility of this method are performed. To create defined structures for cell growth, certain areas will be ablated with a laser. In this way, not only the separation of distinct cell populations should be achieved, but also a predetermined direction of growth and thus signal transmission.

- **Structured Cell Growth can be combined with Calcium Imaging and Optogenetics to enable spatially directed Signal Generation**
  Finally, the structured cell growth approach will be combined with calcium imaging and optogenetics to enable spatially directed signal generation.

The following thesis is divided into several parts. Chapter 2 gives an overview of the discovery of optogenetics and the physiological properties of channelrhodopsin. Further, the relevance of calcium signaling in neurons is explained in detail in order to give an introduction to all-optical optogenetics in neurons. Chapter 3 briefly introduces neuroprosthetics, goes then into more detail about the physiology of hearing and compares a classical electrical cochlear implant with a possible optical cochlear implant. Chapters 4 and 5 contain the materials and methods used in this work. Chapter 6 summarizes the results that were produced in the course of this work. Chapter 7 then discusses the observations made, gives an outlook how future experiments could continue and how the transfer to the clinical application can be driven forward. Finally, a conclusion summarizes the observations made.

2 Optogenetics

This chapter describes the discovery of Channelrhodopsin (ChR) and the physiological fundamentals of *Chlamydomonas reinhardtii*. It goes into detail about the photocycle of Channelrhodopsin-2 (ChR2) and describes the underlying opening and closing mechanisms in more detail. Finally, calcium signaling within a neuron and the working mechanism of voltage and calcium sensors will be explained to understand how all-optical optogenetics in neurons can be achieved.

2.1 *Chlamydomonas reinhardtii* – How an Algae is Revolutionizing Neuroscience

Chlamydomonas reinhardtii, an unicellular green alga and plant model organism with a little eyespot for phototaxis, is one of the best-studied ChR origin (**Fig. 3**). The light-sensitive eyespot contains large amounts of carotenoids[28], a retinal chromophore embedded in Seven Transmembrane Helices (7TM) forms the functional unit[29]. Layers of carotenoid vesicles of low and high refractive index reflecting the incoming light on the photoreceptors depending on the direction of light incidence, resulting in the change of rotation of the alga and thus, approach or retreat from the light source. While ChR1 predominantly mediates proton conductance, ChR2 allows for the permeation of different cations, which makes especially ChR2 to an extremely useful tool to control neuronal activation in cultured cells and living animals[30,31,32]. Blue light stimulation causes a conformational change that allows distinct cations (H^+, Na^+, K^+, and Ca^{2+}) to passively enter the cell down their concentration gradients leading to a light-dependent modulation of the membrane potential by ChR2, which is reinforced by voltage-gated cation channels (VGCC) regulating flagellar movement[33].

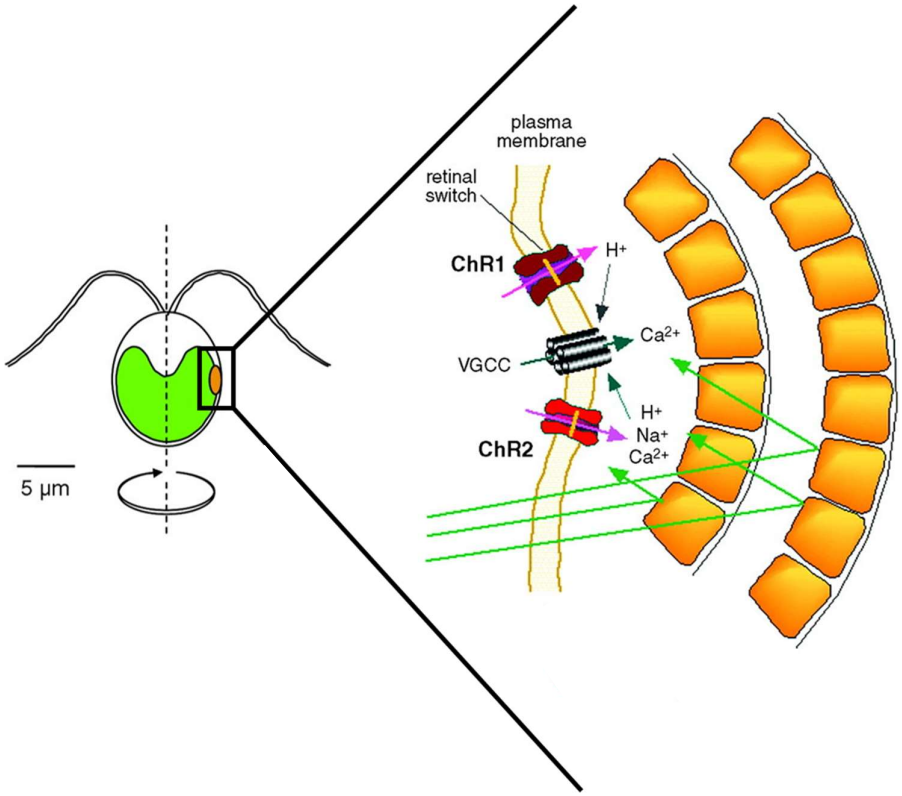

Fig. 3 *Chlamydomonas reinhardtii*: Organization of the eyespot

Schematic representation of a *Chlamydomonas* algae with its typical eyespot and two flagella. The layer arrangement of carotenoid-containing vesicles acts as an interference reflector and enables the direction of the incident light. The photoreceptors Channelrhodopsin-1 and -2 and a Voltage-Gated Cation Channel are located on the outside of the eyespot and represent light-activated cation channels. (Modified from Bamberg and Hegemann et al. 2004[28])

It was Peter Hegerman's lab figuring out that the photoreceptor and ion channel are intimately linked to each other, forming a single protein complex[34]. First explorations outside of *Chlamydomonas reinhardtii* were performed in collaboration with Georg Nagel by expressing the channelrhodopsin variants ChR1 and ChR2 in Xenopus oocytes, revealing direct light-gated cation channels. At the same time, ChR2 was also used in other cell types, like human kidneys and other mammalian cells to depolarize these cells[29,35]. This was the starting point for laboratories all around the world to start working with a truncated ChR2 version which was suitable for light-gated cation conductance, demonstrating functionality in the retina of blind mice, hippocampal neurons, the spine of living chicken embryos, mouse brain slices and transgenic worms[36,31,37,38]. The field of optogenetics was born. For the first time, it was now possible to photo stimulate neurons without adding any chemical compound such as caged ligands or electrical stimulation. This is known as one of the biggest breakthroughs in

neuroscience in the last decades[39,40]. It has the potential to cure epilepsy[22], blindness[23], deafness[24], and treat Parkinson's disease[41]. Before the discovery of ChR, scientists were limited to record the activity of neurons in the brain and correlate this with behavior. This has the disadvantage that one cannot really say if the recorded neural activity actually caused that behavior. Now the causal link between activity in a specific group of neurons and behavioral events like decision making is possible thanks to the optical control of genetically modified cells with light[42]. Due to the power, temporal precision of direct optical activation, specificity, speed, and no needs of any external chemical compound, it was henceforth microbial opsins like ChR that dominated the field of genetically targeted remote control of excitable cells like neurons[43]. The original ChR variants had some limitation downsides, like the one optimal excitation wavelength (~470 nm), extra spikes at high expression rates, and the relatively long recovery time limiting controlled neuron firing to 20 – 40 Hz. To overcome this, ChR2 has been continually optimized using genetic engineering. By creating chimeras of ChR1 and ChR2 and mutating specific amino acids, the resulting variants ChEF and ChIEF dramatically reduced desensitization and allowed the driving of action potentials up to 100 Hz[44]. Further mutation studies in ChR2 ultimately resulted in variants with faster on- and off- kinetics allows for control of individual action potentials at frequencies up to 200 Hz in neurons[30]. Not only mutations but also screening for other channelrhodopsin in other species led to astonishing discoveries for example VChR1 from the multicellular alga Volvox carter, with a red-shifted absorption spectrum compared to ChR2[45]. This allows for spectrally clean separated excitation of two neuronal populations at two different wavelengths, for example in the prefrontal cortex region, enabling probing of psychological disorders like schizophrenia and autism and the underlying circuit-physiology manifestations[46].

ChR2 is an optical excitation technology but in order to fully understand neural processes like action, emotions, and thought, a temporally precise optical inhibition of neural activity would also be needed. An archaeal light-driven chloride pump (NpHR) from Natronomonas pharaonis allows either knockout of single-action potentials, or sustained blockade of spiking by applying yellow shifted light[47]. Used together a NpHR/ChR2 system enables rapid bidirec-tional control of neurons on a millisecond timescale, facilitating emulation or alteration of the neural code and due to its spectral separation in activation maxima permitting elucidation of the roles of specific cell types in high-speed intact circuit function. Taken together, this could enable highly precise optical therapeutic treatments in diseases associated with neurons or other excitable cells for example Parkinson's disease[41]. Another milestone was the combination of ChR2 with

calcium imaging for all-optical contact-free experiments to investigate active synaptic contacts[24], which will be discussed in more detail in chapter 2.3.

2.2 *Channelrhodopsin 2* and its Photocycle

The best-studied ChR originate from *Chlamydomonas reinhardtii* as mentioned above. Its two isoforms of ChR (ChR1 and ChR2) were discovered first in the plasma membrane of the so-called "eyespot" equatorial to the flagellar axis. ChRs are typically composed of seven transmembrane helices consisting of about 700 amino acids, half of which belong to a hydrophilic domain that protrudes into the cytosol (**Fig. 4**). In optogenetics, only the first 300 – 350 amino acids of the N-terminus are used since the hydrophilic domain has no role in ion exchange and is believed to bind the cytoskeleton to ensure localization in the eyespot[29]. The native chromophore in the dark-adapted all-*trans* retinal is embedded within the hydrophobic center, covalently linked via a Schiff base to a conserved lysine, and undergoes a protein conformational change by light absorption, leading to an opening of the ion pore. This conductance of cations through the membrane is mediated by a cyclic reaction initiated by light absorption. During the dark ground state, nearly 100 % of the retinal shows an all-*trans* conformation. Spectral characteristics of ChR2 were examined by activating the channel with short laser pulses (470 nm, 10 ns) and measuring the absorbance changes in the visible range, as the molecule gets back to the ground state[48]. These measurements revealed four different kinetic intermediates with very different time constants called P_1, P_2, P_3, and P_4.[49]. In the following, a simplified unidirectional photocycle model of ChR2 is explained in more detail.

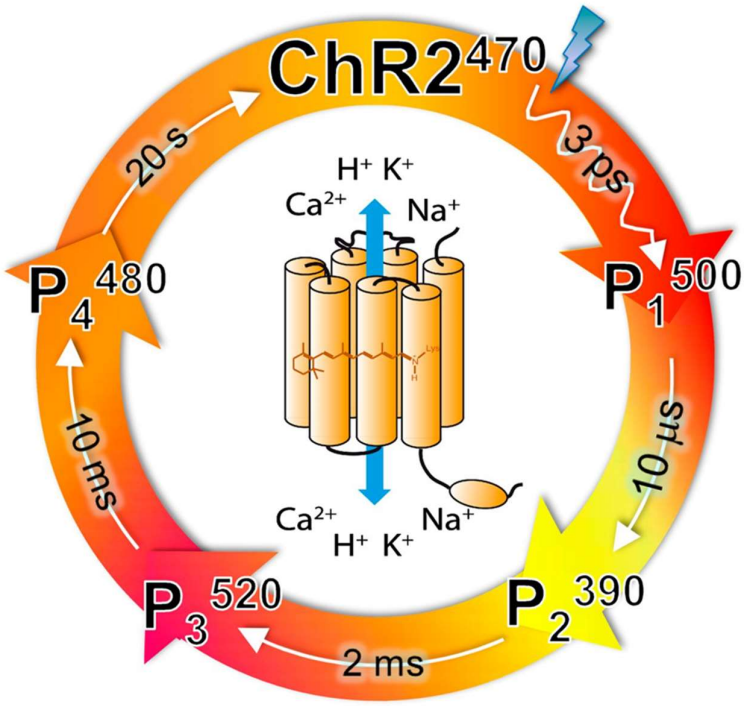

Fig. 4 Schematic Illustration of the Photocycle of ChR2 under Single Turnover Conditions

Each reaction intermediate indicates the wavelength of maximum absorption (P_1^{500}, P_2^{390}, P_3^{520}, and P_4^{480}). After illumination (blue flash), the retinal (orange molecule) isomerizes from all-*trans* to 13-cis retinal. The photocycle is initiated by the absorption of blue light (blue lightning). The time constants for the transitions from one intermediate to the other are characterized by the half-life ($t_{1/2}$). (Modified from Heberle et al. 2013[50])

After illumination, all-*trans* retinal isomerizes to 13-cis retinal. This absorption is red-shifted from the ground state of 470 nm to 500 nm in the first phase (P_1^{500}). P_1^{500} formation takes place within picoseconds after photon absorption. Subsequently, the retinal deprotonates and the blue-shifted P_2^{390} intermediate ($\lambda_{max} \approx 390$ nm) state is formed. The following re-protonation leads to the red-shifted P_3^{520} state ($\lambda_{max} \approx 520$ nm) with $t_{1/2} \approx 2$ ms. Finally, P_3^{520} decays predominantly to the initial ground state, and partially to the relatively long-lived P_4^{480} state with $t_{1/2} \approx 10$ ms[50]. The structure changes are reversed during the closing of the conducting pore and reversion to the dark ground state. This path distinguishes from the opening path and the kinetics of dark state recovery is many orders of magnitudes lower. Thus, understanding both the channel opening and closing is of fundamental importance for applying mutations to the same and increase the open states lifetime.

2.3 All-optical Optogenetics in Neurons

Calcium signaling is important in the versatility of different events in all cell types[51], like controlling the heart muscle cell contraction[52] or in regulatory aspects of the entire cell cycle, from proliferation to cell death[53]. In neurons, calcium has a variety of functions. Depending on the localization within the cell, Ca^{2+} triggers different pathways. For example, calcium influx through voltage-gated Ca^{2+}-channels triggers exocytosis of neurotransmitter in presynaptic terminals[54] and for the postsynaptic plasticity, a transient rise in calcium level within the dendritic spines is crucial[55]. Calcium also plays a very important role in regulating gene transcription[56]. Notably, only free unbound calcium is biologically active. At rest, the calcium concentration within a neuron is usually about 50 – 100 nM, which rises upon activation up to 100 times[51]. **Fig. 5** depicts some of the most important calcium sources in a neuron. The cytosolic calcium concentration is maintained by the balance between calcium efflux and influx, as well as by the exchange of calcium with internal stores. Also, calcium binding proteins as calbindin-D28k or parvalbumin contribute to maintaining the cytosolic calcium concentration, acting as calcium buffers to determine the dynamics of free Ca^{2+} inside a neuron[57]. To regulate the calcium influx from the extracellular space, the cell has multiple mechanisms including ionotropic glutamate receptors, voltage-gated calcium channels, nicotinic acetylcholine receptors (nAChR) and transient receptor potential type C (TRPC) channels[58,59]. For removing calcium ions out of the cytosol on the other hand, the calcium ATPase (PMCA) and the sodium-calcium exchanger are responsible[60]. Calcium release from internal stores, mostly the endoplasmic reticulum (ER), is mediated by ryanodine receptors and inositol trisphosphate receptors. The relatively high calcium concentration in the ER in comparison to the cytosol is maintained by the sarco-/endoplasmic reticulum calcium ATPase (SERCA), which delivers calcium from the cytosol to the lumen of the ER. Another important factor for calcium homeostasis is mitochondria. They act as calcium buffers by taking up cytosolic calcium during calcium elevations. This uptake is regulated by the calcium uniporter and by normalization of the cytosolic calcium, the so stored calcium is slowly released back to the cytosol through sodium-calcium exchange[61].

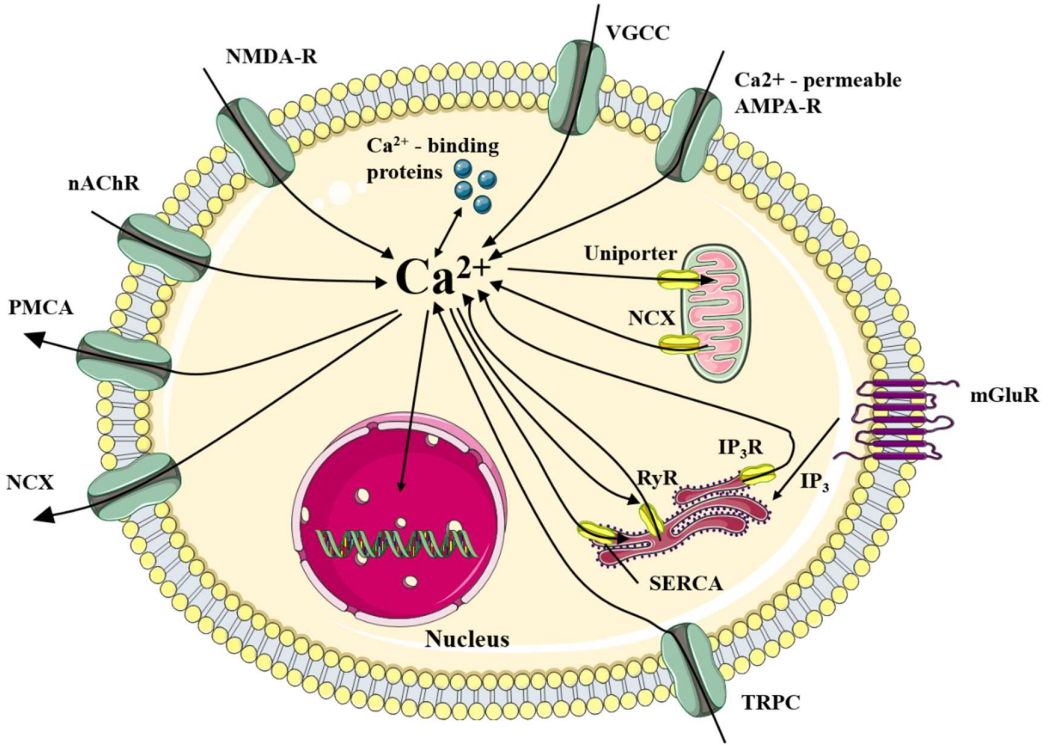

Fig. 5 Calcium Signaling in a Neuron

The most important mechanisms of Ca^{2+} influx and efflux of neurons, without taking into account their spatial organization within the different cell sub compartments. Sources of calcium influx are nicotinic acetylcholine receptors (nAChR), N-methyl-D-aspartate (NMDA) glutamate-type receptors, voltage-gated calcium channels (VGCC), calcium-permeable α-amino-3-hydroxy-5-methyl-4-isoxazolepropionic acid (AMPA), and transient receptor potential type C (TRPC) channels. Calcium release from internal stores is mediated by ryanodine receptors (RyR) and inositol trisphosphate receptors (IP_3R). Metabotropic glutamate receptors (mGluR) are capable of producing and delivery of inositol triphosphate (IP_3). The sodium-calcium exchanger (NCX), the plasma membrane calcium ATPase (PMCA), and the sarco-/endoplasmic reticulum calcium ATPase (SERCA) regulating the calcium efflux. Additionally, the mitochondria contribute to the maintaining of neuronal calcium homeostasis.

Throughout the last decade, the process of using light to control and monitor neurons has become a common practice in many neurological studies. A continuously expanding toolbox of molecular probes that activate / inhibit or map neural activity has made an enormous contribution to the direction of research and led to innovative experimental concepts[62,63]. To probe the connectivity of a neuronal network, for example, it is essential to have a neuronal culture system that facilitates simultaneous stimulation and recording from a large group of neurons and preferably with single-cell readout. Traditional electrophysiological methods are technically very challenging and time-consuming. Further, with electrophysiological tools the number of cells that can be studied is very limited and the cellular viability can be affected due to the need for physical contact with the tissue under investigation[64]. Light, on the other hand,

can examine neuronal networks without direct contact with the tissue and does not interfere with neuronal function. Additionally, light has several advantages over electrophysiological methods like excellent spatial resolution[65], simultaneous recordings across multiple spatial locations[66], and the possibility to probe specific cell types by optogenetics (for example channelrhodopsin and /or halorhodopsin) within the same network[67]. However, in contrast to electrophysiological measurements, probing of neuronal function with light requires typically a reporter that converts membrane potential into an optical signal. **Fig. 6** shows the principle of how a typical voltage or calcium sensor works.

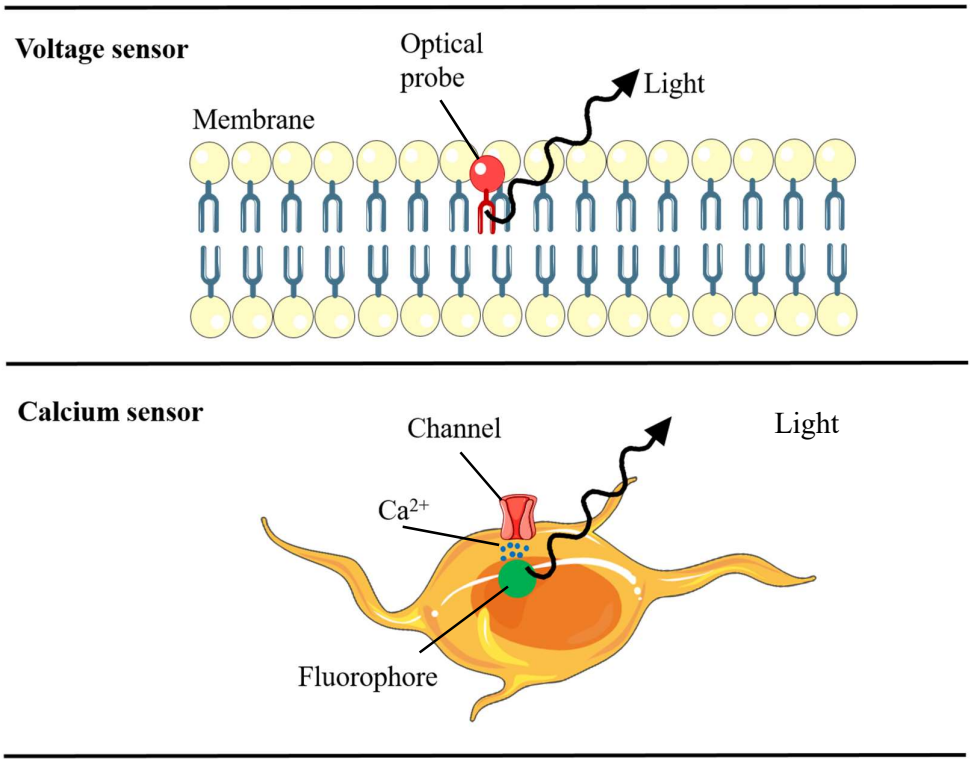

Fig. 6 Working Mechanism of Voltage and Calcium Sensors

Voltage-sensitive dyes (VSDs) generate fluorescence that depends on the change of the electric field across the membrane, making recordings of single-trial action potentials in neurons possible. Calcium sensors change their conformation by binding calcium, this, in turn leads to an increased fluorescence signal. (Modified from Scanziani and Häusser 2009[64])

Measuring Voltage Changes

Developing voltage sensors approaches with the required dynamic range, sensitivity, and speed to record minimal changes in membrane voltage (subthreshold and suprathreshold events) would be an enormous advantage over electrophysiology. It would allow the measurement of the spatiotemporal dynamics of membrane potential across the cell or even across a population of neurons, which is practically impossible for electrodes. First attempts focused on detecting electrical activity in cultured neurons by changes in their intrinsic optical properties[68]. Although it was already possible to image brain function for a resolution of about 100 µm, this method lacks an appropriate signal-to-noise ratio for cellular imaging[69]. The most promising reporter to detect single action potentials by change of membrane potential are voltage-sensitive dyes (VSDs). These split up into a portion on one side of the plasma membrane and generate fluorescence that depends on the change of the electric field across the membrane[70]. By injecting VSDs into single neurons, it was already possible to record single-trial action potentials in small neuronal compartments[71] and even in single-trial populations *in vivo*[72]. However, the resolution of subthreshold events is still difficult to detect with this method. Due to the small fluorescence change per unit in membrane potential and the fact that VSDs label not only the plasma membrane but also cell compartments, the signal-to-noise ratio is relatively low. To overcome the limitations of intracellular background fluorescence, genetically encoded voltage indicators (GEVIs) are the methods of choice. Since their expression can be genetically targeted to specific subpopulations of neurons and subcellular regions as the plasma membrane, these sort of sensors has an enormous advantage over conventional VSDs. There are two main design strategies for such sensors. The first one is a fusion construct of a modified GFP into a voltage-sensitive K^+ channel, so that voltage-dependent changes of the channel induces changes in the fluorescence of GFP, leading to a fractional fluorescence change of 5.1 %[73]. Another approach is the use of a hybrid GFP system, where resonant energy transfer (FRET) is used to report an interaction between a cytoplasmic anchored GFP and a dye that undergoes voltage-dependent redistribution between the inner and outer side of the membrane[74]. Whereas GFP-based probes have limited success in recording the electrical activity of neurons, because of their poor temporal resolution and low sensitivity, the hybrid approach and its FRET-based voltage sensor lead to large fluorescence signal (up to 34 % change per 100 mV) with a fast response and recovery time[75,76]. However, the biggest problems with GEVIs still are their slow kinetics (typically order of tens of milliseconds), making measurements of single-action potentials challenging. Another problem is the low brightness and poor targeting towards the plasma membrane, which in turn increases the background signal. The inclusion into the plasma

membrane can also lead to unwanted side effects due to the resulting increase of the membrane capacitance (so-called capacitive loading) and can even prevent action potential generation[77]. Nevertheless, there are new promising attempts for probing input-output properties of individual cells in cultured neurons with high throughput[78]. It would be very advantageous to have red-shifted GEVI variants in combination with blue-shifted channelrhodopsin variants like CheRiff[79], but this is still lacking. There is actually one red-shifted GEVI class, based on microbial rhodopsin proton pumps (QuasAr), shows weak changes in fluorescence of a retinylidene chromophore by changes in membrane voltage. The main advantage of those rhodopsin-based GEVIs is, that they are excited by red light and emit in the near infrared, showing response amplitudes of up to 90 % per 100 mV and response speeds of 0.05 ms[79]. This facilitates all-optical stimulation with optogenetic actuators, with minimal crosstalk of the reporter. However, due to the fact that voltage transients are ~100-fold briefer than Ca^{2+} transients for example, a voltage indicator must be excited with much greater illumination intensity to achieve similar photon counts, speaking of phototoxicity and photobleaching.

Calcium as an Indicator of Activity

Calcium signaling is important in the versatility of different events in all cell types. In neurons, it acts as a major signaling molecule, since membrane voltage fluctuations and synaptic input often triggers intracellular calcium concentration. There are different approaches available to probe Ca^{2+} changes over time, like chemical and genetically encoded calcium indicators. Chemical calcium indicators consist of a calcium chelator and a fluorophore. One of the first generation fluorescent calcium indicators was Fura-2, which became very popular among neuroscientists because of its high fluorescence change due to calcium binding and the fact that it allows more quantitative calcium measurements involving the ratio of the signals obtained with alternating the excitation wavelengths. By binding calcium, the molecule undergoes a conformational change, which causes a photon to emit. Chemical calcium indicators are divided into single wavelength and ratiomeric indicators. The ratiomeric Ca^{2+} indicators change their emission or excitation maximum by binding of calcium. This is often used to estimate calcium concentrations within a cell. Single wavelength calcium indicators on the other hand increase their fluorescence upon Ca^{2+} binding. A major advantage of chemical calcium indicators is that they are available in different forms, either membrane-permeable or membrane-impermeable form, depending on the type of calcium indicator, the scientific question, and the biological preparation[80]. The chemical calcium indicators are available in three different forms: dextran

conjugates, salts, or acetoxymethyl (AM) esters. Salts and dextran-conjugates are impermeable for the membrane and need invasive dye loading. This is often done while single-cell probing during patch-clamping. When salts are loaded properly, they often show compartmentation to membrane-bound vacuoles over long time durations. The AM ester calcium indicator can simply be added to the medium of the cells because the AM esters are hydrophobic enough to penetrate the plasma membrane. When the chemical calcium indicator with the AM ester enters the cell, the ester is cleaved by intracellular esterase and the dye is trapped within the cytosol. If chemical calcium indicators are used, it should be noted that they serve as additional calcium buffers in the cell, and thus can also influence the intracellular calcium signals[81]. Last, to say, these indicators are available at different spectral properties and different calcium affinities, allowing for simultaneous use. One more class is the genetically encoded calcium indicators (GECIs). They come in two different mechanisms of action, namely those involving Förster resonance energy transfer (FRET) and the single-fluorophore ones (**Fig. 7**).

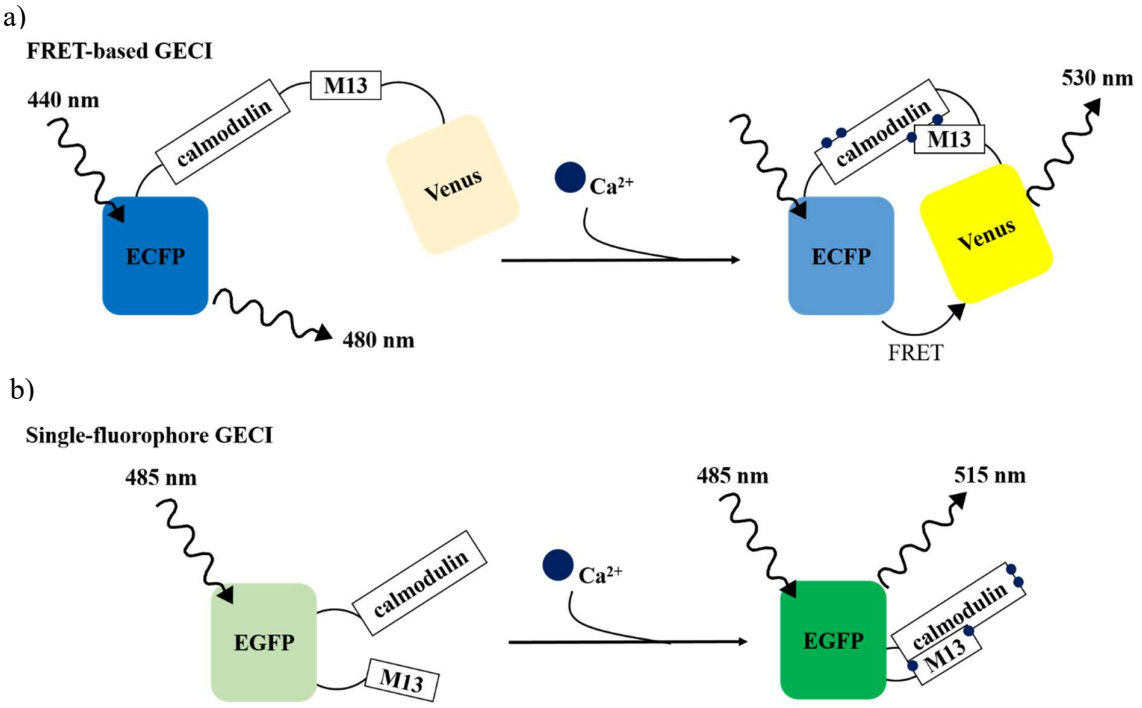

Fig. 7 Genetically Encoded Calcium Indicators (GECI)

(a) FRET-based GECI. In its Ca^{2+} unbound form, the enhanced cyan fluorescent protein (ECFP = donor) emits light at 480 nm. When bound to Ca^{2+}, calmodulin undergoes a conformational change, bringing the donor and the acceptor (Venus in this case) spatially closer together, enabling FRET and thus leading to light emission of 530 nm. (b) Single fluorophore GECI on the example of GCaMP. The enhanced green fluorescence protein (EGFP) is flanked by the Ca^{2+} binding protein calmodulin and the peptide M13. After binding of Ca^{2+} to GCaMP, a conformational change leads to an increased emitted fluorescence signal of 515 nm. (Modified from Grienberger and Konnerth 2012[80])

FRET is a method that relies on non-radiative energy transfer and includes a donator fluorophore and an acceptor fluorophore. If both fluorophores are spatially closer than 10 nm, the emission wavelength changes. This is made possible due to a calcium-binding link protein between a donor fluorophore and an acceptor fluorophore. Upon calcium binding, the conformation changes in a way that the distance between acceptor and donor is less than 10 nm so the emission of the acceptor can be recorded[82]. Single fluorophore GECIS consists most times of a fluorescent protein surrounded by a calcium-binding protein and a calcium-binding peptide. The best-known representative of single-fluorophore GECIs is the GCaMP family[83,84,85]. GCaMPs consist of an enhanced green fluorescent protein (EGFP), which is flanked by the calmodulin-binding peptide M13 and the calcium-binding protein calmodulin on the other side[86]. When calcium is bound by the protein and peptide, calmodulin-M13 interactions elicit conformational changes in the fluorophore environment that lead to an increase in the emitted fluorescence. Through protein engineering, many GCaMP variations, for example, GCaMP6, with improved signal-to-noise ratio, dynamic range, and response kinetics, allowing detection of single action potentials in many situations, have been created[87,88]. However, GCaMPs and GECIs, are limited by their excitation and emission spectra. If an *in vivo* application with transgenic animals is desired that already expresses GFP, GCaMPs are very difficult to use due to the resulting poor signal-to-noise ratio. Additionally, the blue excitation light used often causes photo damage and is highly scattered in tissue. Further is the GCaMP emission absorbed by the blood, which has a negative effect on the penetration depth for imaging within the tissue[89]. When combining with ChR2, the spectral overlap with GCaMP excitation makes the simultaneous use of green GECIs and optogenetics very challenging. There are already red fluorescent protein (RFP) based GECIs which share the overall architecture of the GCaMP sensors, coming along with a calcium-binding protein (calmodulin) and a binding peptide (M13 or ckkap)[15,90,91]. Red-shifted GECIs have three main advantages over GFP-based sensors: reduced photo damage, increased penetration depth, and the possibility of parallel use of a red GECI with light-sensitive ion channels, for example, ChR2, for all-optical neurophysiology experiments. To probe heterogeneous neural networks, it is often critical to understanding the activity and the way, how multiple neurons communicate with each other. A culture system that enables the simultaneous stimulation and recording from a large group of neurons with single-cell readout is essential to capture the connectivity of a 2D or even 3D network. Due to the achievements in designing new sorts of spectrally red-shifted GECIs, like jRCaMP1a, a GECI based on mRuby[92], with an excitation maximum of ~ 570 nm

and an emission maximum of ~592 nm[93] and the blue-shifted ChR variant CheRiff, it is now possible to spectrally independent photo stimulate and image optically evoked calcium activity in neuronal cultures. This is making network activity studies possible and thus could open new doors in the understanding of network function[94]. **Fig. 8** gives an overview of some state-of-the-art all-optical interrogation of neural circuits.

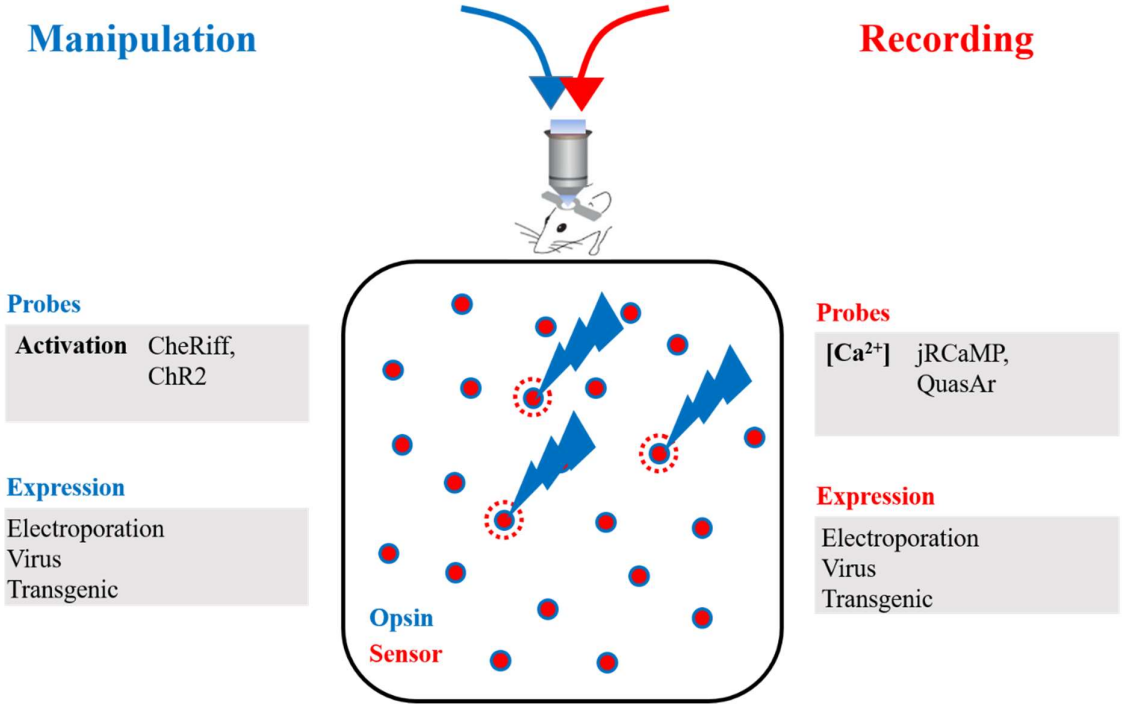

Fig. 8 Toolkits Available for all-optical Interrogation of Neural Circuits

A schematic drawing of different ingredients needed for an all-optical approach in neuronal networks is shown. For the manipulation side: the most common blue activatable channelrhodopsin variants ChR2 and CheRiff, with a blue-shifted action spectrum with a peak at $\lambda_{max} \sim 460$ nm. On the recording site: a red-shifted GECI based on mRuby, namely jRCaMP1a (λ_{ex} = 570 nm; λ_{em} = 592 nm) and the archaerhodopsin-based voltage indicator QuasAr (λ_{ex} = 590 nm; λ_{em} = 715 nm). Taken together, a blue-shifted actuator (ChR2 or CheRiff) plus a red-shifted sensor, either a GECI like jRCaMP1a or a GEVI like QuasAr, provide a powerful tool for all-optical interrogation of neural circuits. (Modified from Emiliani and Häusser et al. 2015[95])

3 Applied Optogenetics on the Cochlear Implant

This chapter contains a brief introduction to the current state of neuroprosthetics and then goes into more detail about the cochlear implant as the most successful neuro-implant in history. In the course of this, the physiology of hearing is explained in more detail and advantages and disadvantages of an electrical vs. optical cochlear implant are compared.

3.1 Neuroprosthetics Nowadays

In the last few decades of technological developments, the field of neuroprosthetics came up with dozen replacement strategies, rehabilitation procedures, and neuromodulation therapies to improve the life quality of individuals with neuromotor disorders like blindness[96], deafness[97], chronic pain[98] but also bladder control[99] and motor prosthetics for conscious control of movement[100]. A very prominent example of replacing a missing biological function is Neil Harbisson, founder of the Cyborg Foundation. He was born with an extreme form of colorblindness, allowing him to sense the world in grayscale only. He got an antenna implanted in 2004, a hybrid device of a camera and a bone-conducting hearing aid, allowing him to sense colors via audible vibrations not only in the visible range for human eyes but also UV light[101]. The so-called cyborg antenna is actually not a neuroprosthesis by definition, but it highlights the infinite possibilities in this area.

Neuroprosthetics is forming interfaces between the nervous system and the connection to an electronic component to partially restore body functions. Classically, individual microelectrodes or electrode arrays are used to correct or restore pathological or lost functions of the nervous system[102]. Today that already applies to a motor, sensory, or cognitive modality that might have been damaged as a result of an injury or a disease. In the field of vision restoration, the retina implant is the most successful under all attempts. A device like this consists of an external (or implantable) imaging system that acquires and processes the resulting video. The received digital data are then converted to an analog output which is further delivered via micro electrodes to the visual nerve circumventing the degenerated photoreceptors of Retinitis Pigmentosa patients[103]. Another prominent example for neuroprosthesis is motor prosthetics, devices that support the function of the autonomous nervous function for conscious control of movement, the so-called brain-computer interface. Implants like these, one day will help to restore movement and the ability for disabled persons to communicate with the outside world. For this purpose, microelectrode arrays have been developed that are smaller than a square centimeter, which is directly implanted in the skull to capture signals from the brain. These neuronal signals are then translated into movements, allowing patients already to move

computer cursors[104]. The technical advancements in the field of robotic exoskeletons are very exciting and making big steps toward the initial prototypes to assist human movement one day[105]. But for now, the most successful clinical neuroprosthesis is the cochlear implant (CI)[106].

3.2 The Optogenetic Cochlear Implant

Acoustic signals consist of various air pressure waves and are thus, defined by physical characteristics such as amplitude and frequency that fluctuate over time. When a soundwave hits the ear, it will be collected and focused by the pinna into the ear canal, where it is delivered to the tympanic membrane (**Fig. 9**). The pinna works thereby as a cue for sound source localization by changing the frequency spectrum.

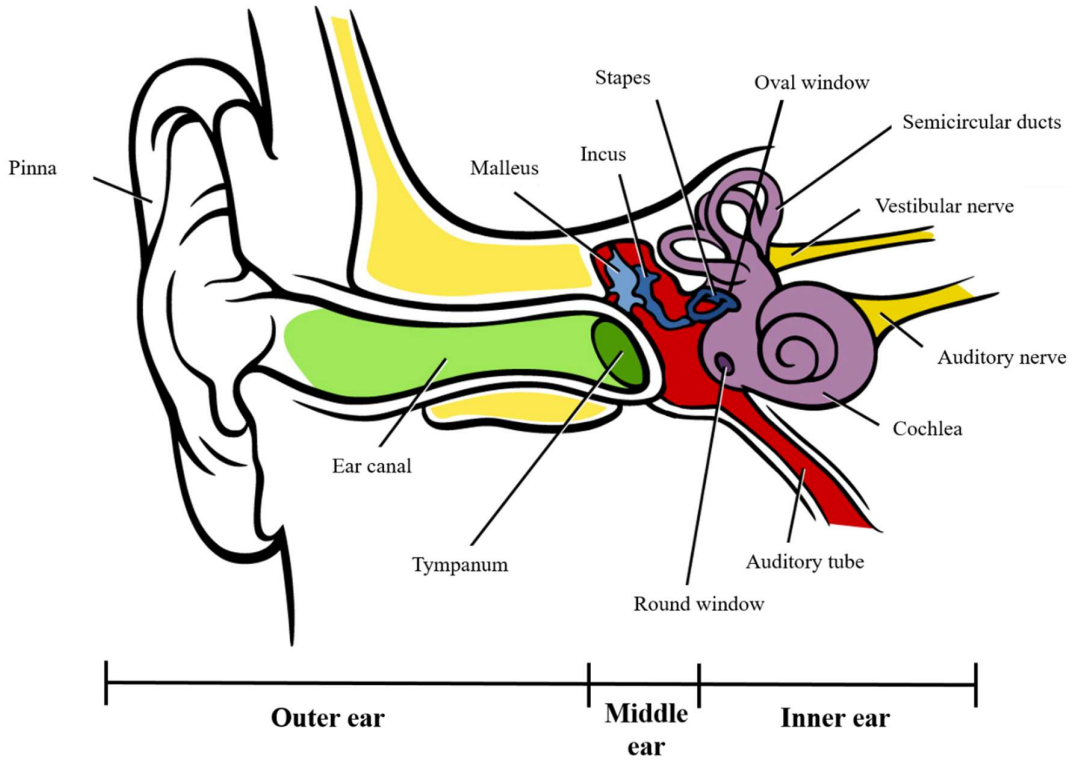

Fig. 9 Schematic Drawing of the Human Ear

The human ear can be divided into three main compartments: the outer, middle, and inner ear. The ossicle chain, consisting of the malleus, incus, and stapes, connects the tympanic membrane (Tympanum) with the oval window of the cochlea. (Modified from Rye et al. 2016[107])

Attached to the tympanic membrane are the ossicles, which act as conveyers of air vibrations to the fluid-filled cochlea. This change from low-impedance of the air to the much higher impedance of the cochlear is essential to prevent reflection of energy by cochlear perilymph. When vibrations enter the inner ear, the pressure will be increased almost 200-fold due to the

difference in surface area between the tympanic membrane and the smaller oval window[108]. The cochlea itself is a bony, snail-shaped structure divided by the flexible basilar membrane and the Reissner's membrane into three distinct fluid-filled cavities, the scala tympani, the scala media, and the scala vestibule (**Fig. 10**). The scala tympani and scala vestibuli contain the Na^+/Cl^--rich perilymph whereas scala media contain K^+-rich endolymph. At the cochlear apex, the scala tympani and the scala vestibuli are connected via the helicotrema. The outer two chambers are also contacted by the oval and round window and form a continuous channel that allows sound vibrations to travel through the cochlear fluids. The scala media lies between the two outer chambers and holds the organ of Corti, where the hair cells are located. If the soundwaves reach the base of the oval window, the stapes start vibrating and this is pushing the perilymph in the scala vestibuli towards the cochlear apex. That in turn, pushes the perilymph in the scala tympani via the helicotrema towards the round window, causes it to deflect outwards.

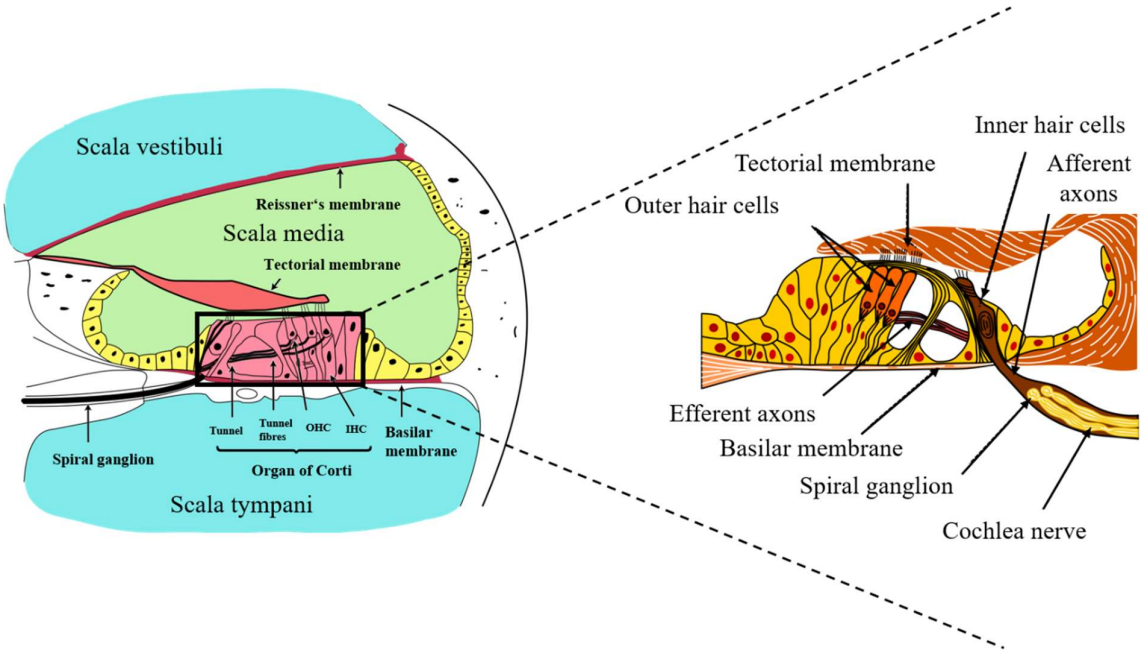

Fig. 10 The Cochlea and Organ of Corti in Detail

Schematic drawing of the cochlea-cross section and the organ of Corti (magnified). The cochlea-cross section shows its three compartments (scala vestibuli, scala media and scala tympani) and the position of the organ of Corti between scala media and scala tympani. The enlarged area depicts a detailed anatomical organization of the organ of Corti, showing its characteristic single row of inner hair cells (IHCs) and three parallel rows of outer hair cells (OHCs). Also shown is the tectorial and basilar membrane as well as afferent and efferent innervation. (Modified from Orahi 2004[109] and Madhero88 2009[110])

The basilar membrane has different mechanical properties along the cochlea axis. It gradual decrease in width and increase in stiffness from the cochlear apex towards the base, resulting in the frequency-dependent displacement of pressure waves. The basal, firmer end responds best to higher frequencies (perceived as high tones) while low frequency (perceived as deep tones) waves walking up to the cochlear apex and mainly deflect the wider and more flexible part of the basilar membrane (**Fig. 11**). This effect causes a topographical frequency gradient called tonotopy, determining the frequency hearing range of the cochlea[111].

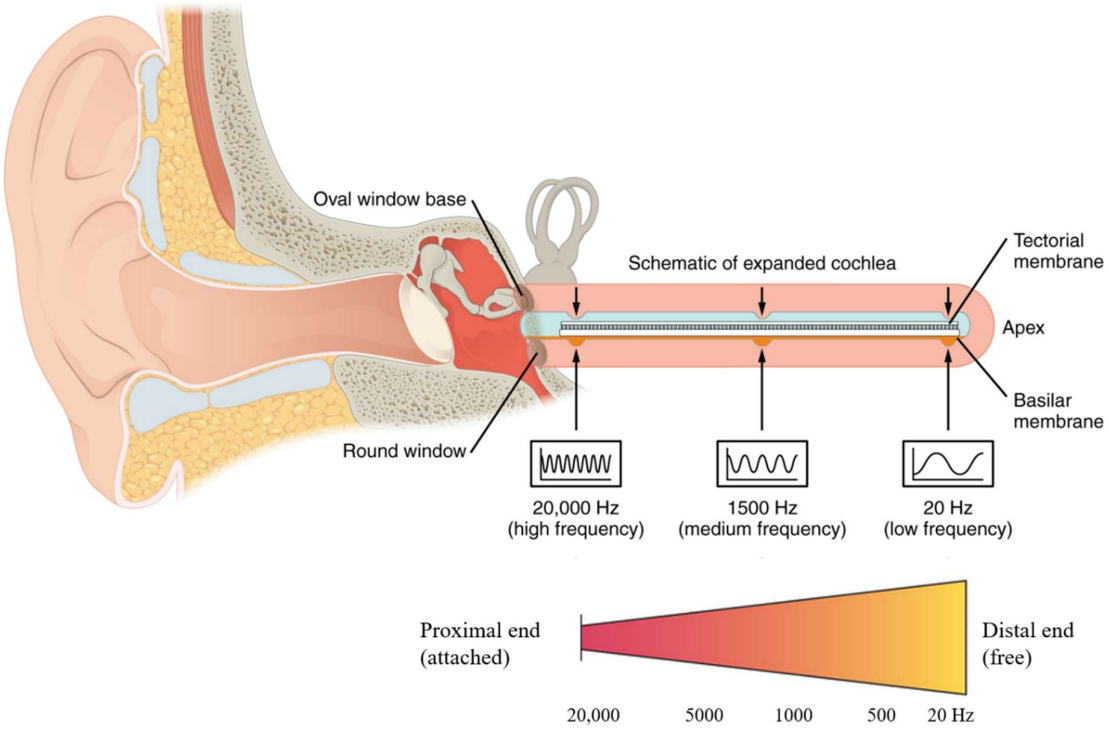

Fig. 11 Frequency Response of the Cochlea

Simplified schematic of an uncoiled cochlea showing how sound vibrations would propagate along the basilar membrane as a traveling wave from the proximal to the distal end. Due to the gradually changing mechanical properties of the basilar membrane, high frequencies (high pitch) are sensed near the base of the cochlea, whereas low frequencies (low pitch) are sensed near the tip of the cochlea, giving rise to its tonotopic distribution. (Modified from OpenStax 2016[112])

The responsible organ for mechanoelectrical signal transduction is the organ of Corti. It is located on the basilar membrane and harbors the hearing receptor hair cells, which detect cochlear vibrations via their stereociliar bundles. The hair cells are organized in three rows of outer hair cells (OHCs) and a single row of inner hair cells (IHCs), running parallel to the basilar membrane along its length. While OHCs regulate and adjust the sensitivity of neighboring of IHCs to sound levels the IHCs are the main sensory cells conveying the sound information to

type I afferent spiral ganglion neurons (SGNs) (~ 95 % type I fibers)[113]. A propagating wave along the basilar membrane deflects stereocilia against the tectorial membrane, which in turn leads to deflection of the hair cell bundles. Depending on the direction of movement, this leads to an influx of K^+, causing graded depolarization of IHCs and subsequently activate voltage-gated calcium channels. The calcium influx ensures the release of the neurotransmitter glutamate into the synaptic cleft, activating the afferent fibers of SGNs via AMPA receptors and if the signal is strong enough, fire action potentials (APs) propagate via the cranial nerve VIII to the cochlear nucleus. The somata of the SGNs are located in the Rosenthal's canal within the mediolus, with their peripheral neurites extending to the base of the IHCs. The bipolar SGNs can reach enormous spike rates of above 1 kHz at sound onset and maintain adapted discharge in the range of hundreds of Hz[114]. This is made possible by a special structure called ribbon synapse, which can also be found in photoreceptors[115]. As mentioned above, sound waves are characterized by their amplitude (intensity or pressure) and their frequency (number of cycles per time window). The incoming sound wave travels along the basilar membrane and deflects it at different locations leading to a specific IHC activation pattern. The following activation of neuronal populations by sound waves of different frequencies is maintained over the entire auditory pathway, over the inferior colliculus, up to the primary auditory cortex. This characteristic is called tonotopy. The following applies: the greater the deflection the more often the neurons fire, the louder a stimulus or sound is perceived. This is exactly where the system's weak point lies, which is not adapted to the high sound levels of the present. Too much stimulation can result in injuries and loss of hair cells and this is irreversible[116]. According to the WHO (1. March 2020) around 466 million people worldwide have disabling hearing loss, 34 million of these are children and this number is estimated to be doubled by 2050. This means even today, 1 out of 80 children is born with profound hearing impairment. Approximately one-third of people over 65 years of age are affected by disabling hearing loss and 15 % of the world's adult population experience at least mild hearing loss[117]. Hearing loss is thus to say a major public health issue, especially in aging societies. Multiple factors, including exposure to loudness, cancer treatment drugs, ototoxic antibiotics, and genetic mutations give rise to hearing loss. Sensorineural hearing loss (SNHL), defined by the presence of deafness-causing disease in the cochlea and the auditory nerve, represents the most common type of hearing impairment (approximately 90 %)[118]. Consequences of hearing loss can be dramatic and severe. During the critical window of the first 3.5 years of childhood development, the auditory system needs sensory input to establish a functional and mature auditory nerve[119]. Depending on the extent of hearing loss, ranging from mild (26 - 40 dB) to moderate (41 - 70 dB) or severe (71 - 90 dB)

form[120], patients might benefit from hearing aids, middle ear implants, or bone conduction implants. If this is not sufficient, for example in case of profound sensory hearing loss or deafness, the cochlear implant (CI) is currently the method of choice to partially restore hearing.

The common CI is an electronic medical device that works on the damaged part of the cochlea to carry audio signals to the brain providing a person with sensorineural hearing loss a modified sense of sound. It consists of an internal part with an intracochlear electrode array encapsulated in silicone linked to an extracochlear stimulator. CIs bypass the peripheral auditory system in the cochlea and replace it with electrical signals that in turn directly stimulate the SGNs. With the help of a physiological effect called neuroplasticity, the ability of the central nervous system to adapt and rebuild synaptic connections in a stimulus-dependent manner, a CI user is able to learn to interpret those artificial signals as sound and speech. Interestingly, large population studies in congenitally deaf children showed that this is most effective during the first 3.5 years of life where indeed auditory pathways show the maximal plasticity[119]. But studies suggest that the central auditory system has a striking capacity for plastic change due to changes in afferent input, even into adulthood[121]. The ability of reformation of neurons enables the brain to accept new input and restore functional perception[122,123]. Therefore, neural implants are most successful, the more peripheral they are connected to the central nervous system, and making use of the neural processing alongside the way up to the auditory cortex. However, the possibility of implanting a cochlear implant is limited to the question if there is a functional auditory nerve and residual SGNs left. Because of this, there are many attempts for implants along the auditory pathway like auditory midbrain implants (AMI) to stimulate the inferior colliculus[124] or the penetrating auditory brainstem implant (PABI)[125]. But, stimulation within the midbrain as well as within the inferior colliculus are facing, despite a severe surgical procedure, crucial issues regarding placing the electrodes in the right place. In addition, due to the lack of neural processing, the quality of hearing performance and speech perception is also very limited with current technologies.

However, successful transplantation of CIs enables open speech comprehension, albeit this is limited to a mostly quiet environment and music appreciation is generally reduced[126]. The CI allows for stimulating several independent channels along the tonotopic map[127]. However, CIs cannot cover the whole frequency range which is needed in normal hearing for several reasons. First, the commercial CI provides a maximum of 12 – 24 physical channels that can be used (32 would be needed for complex music perception[128]). This is due to the high ionic and thus, conductive perilymph of the scala tympani and the relatively high distance between the

electrode and the SGNs. That in turn results in a large current spread around each electrode contact and cross stimulation of neighboring neurons[129]. Another pitfall for an electrically CI is the placement of the electrode within the cochlea. Due to its coiled structure and decrease in diameter, the CIs barely cover the whole length of the scala tympani[130]. Many efforts are made toward a more spectrally resolved SGN activation, for example, direct electrode-neural interfacing[131] or multipolar stimulation[132] but it seems spread of excitation remains the biggest hurdle of electrically CIs. These obstacles could be tackled by an optogenetic cochlear implant (**Fig. 12**). Light can be spatially confined preventing channel cross-talk, resulting in a much higher number of independent stimulation channels and thus, increase of frequency resolution[133].

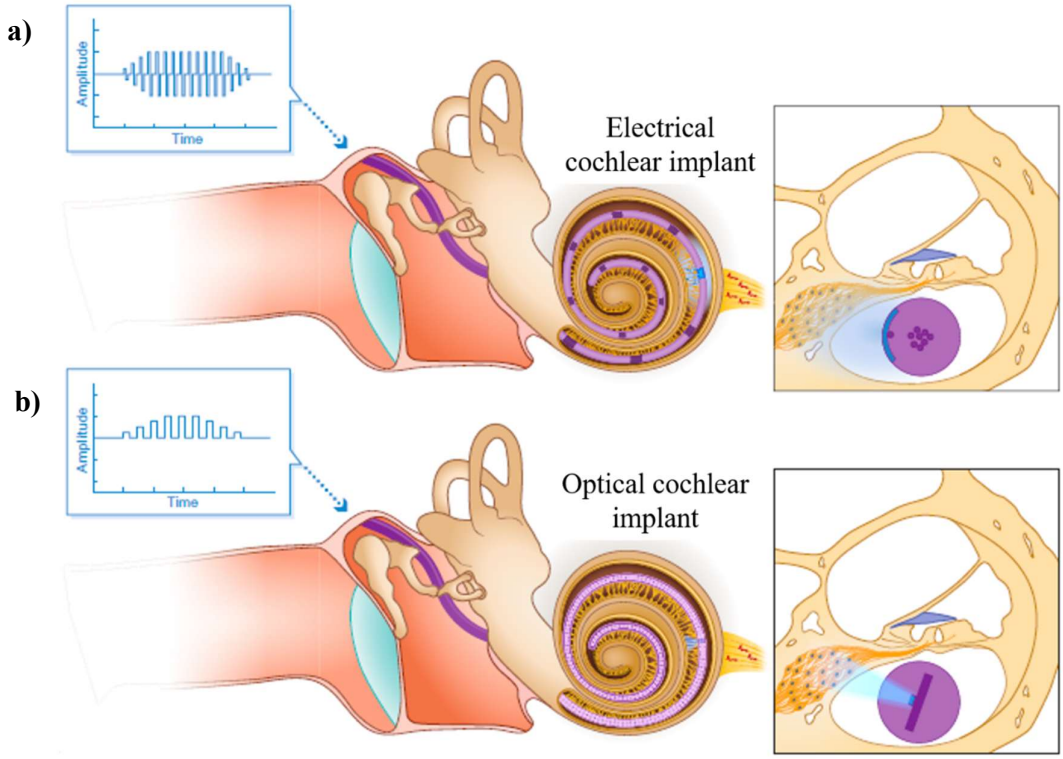

Fig. 12 Comparison of Electrical vs. Optical Stimulation of the Cochlea

Acoustic signals would normally travel along the ear canal and via the ossicles into the intracochlear fluid, where they are decomposed in a frequency-dependent manner. In the case of an electrical (eCI) or an optical (oCI) cochlear implant, the acoustic signals are first processed by an external processor to generate frequencies with the amplitudes of the corresponding signal. SGNs at the tonotopic region for a given sound frequency are then, either activated directly by an electric current (a) or light (b). Since light can be confined better in space (b) than electric current, which spreads widely in an ionic region like the cochlea (a), oCIs promise to activate SGNs with much higher spatial precision. This is the reason why eCIs typically are capable of 12 – 24 stimulation channels while oCIs promise an increase of stimulation channels by an order of a magnitude. (Modified from Dieter et al. 2020[134])

First experiments on optical stimulation of the cochlea were performed with high energy pulsed infrared lasers[135]. But a high-energy requirement for neural activation and the utility of direct infrared stimulation of the SGNs are quite challenging[136]. Nowadays, the optogenetic toolbox of potential candidate opsins for optogenetic hearing restoration has been extended tremendously and allows now for cell type-specific neural control with high spatial and temporal precision, fast enough for auditory coding[137]. Some of these tools, which might be interesting candidates for hearing restoration, are summarized in Table 1. In order to render the auditory pathway sensitive to light, this requires efficient, stable, and safe expression of the target opsin in the SGNs. The method of choice is currently the local administration of non-integrating, low immunogenic adeno-associated virus (AAV) to the cochlea to transduce the SGNs, mostly using a broad neuronal promoter, such as the human synapsin promoter, since within the cochlea the SGNs represent the only neuronal population with cell bodies[138]. AAVs can effectively transduce SGNs but still some side effects like unwanted immune response, reducing transduction efficiency are observed. Furthermore, gene transfer itself would be challenging to translate to clinical practice as well as evenly distribution of the virus within the cochlea[139]. The first evidence of optogenetic hearing restoration by animal behavioral studies has already been published[24]. However, there are still some bottlenecks regarding this technique before considering it for clinical translation as energy requirement, speaking of phototoxicity and biosafety assessments in long-term studies. As already discussed, ChRs with different spectral properties are available. A red-shifted ChRs like Chrimson with an absorption peak at 590 nm allows for deeper tissue penetration and no phototoxic side-effects, as described for blue light stimulation[140]. Even though there are already working animal models, this needs to be scaled up and transferred to non-human primates first. On the technical side, the emitter needs to be power-efficient but bright enough to activate the light sensitive neurons, flexible and small enough to fit in the cochlea and has to be more efficient compared to an electrically driven CI. So future optogenetic hearing restoration requires development of both, the optogenetic manipulation part and the medical device itself. First results are very promising and within the coming years, scientists will surely coming up with new solutions regarding technical and administration issues, making hearing colors real.

Table 1: Candidate Opsins for Optogenetic Hearing Restoration

ChR - variant	τ_{off} (ms)	λ (nm)	Description	References
ChR2	9.4 - 10	~470	The best known and widely used light-gated cation channel from *Chlamydomonas reinhardtii*	Klapoetke et al. (2014)[79], Keppeler et al. (2018)[138]
Chronos	3.0 – 3.6	~490	High-speed, light sensitive channel originated from *Stigeoclonium helveticum*	Klapoetke et al. (2014)[79], Keppeler et al. (2018)[138]
ChETA	4.4	~500	Channelrhodopsin with E123T mutation; faster kinetics but reduces photocurrent amplitude	Gunaydin et al. (2010)[30]
Chrimson	5.7	594	Red-shifted light drivable channel from *Chlamydomonas noctigama*	Mager et al. (2018)[141]
CheRiff	10	~460	Blue-shifted Channelrhodopsin from *Scherffelia dubia*	Hochbaum et al. (2014)[79]; Klapoetke et al. (2014)[14]

Summary of some ChR variants with their closing kinetics at room temperature and peak action spectrum for selected ChR variants.

4 Materials

4.1 Buffers and Solutions

Table 2: Buffers and Solutions Used

Buffer	Ingredients
1x TAE buffer	20 mL 50x TAE
	fill up to 1 L with Millipore water, pH 8.5
1x TE (Tris-EDTA) buffer	1 mM Tris
	1 mM EDTA pH 8.0
	in Millipore water
Bath solution	121 mM NaCl
	5.4 mM KCl
	25 mM HEPES
	0,8 mM $MgCl_2$
	5.5 mM Glucose
Hanks balanced salt solution (HbSS) with 10mM Ca^{2+}	140 mM NaCl
	5 mM KCl
	10 mM $CaCl_2$
	0.4 mM $MgSO_4 – 7\ H_2O$
	0.5 mM $MgCl_2 – 6\ H_2O$
	0.3 mM Na_2HPO_4
	0.4 mM KH_2PO_4
	6 mM Glucose
	4 mM $NaHCO_3$
50x TAE (Tris acetate EDTA) buffer	2 mM Tris
	57.1 mM acetic acid (99 % - 100 %)
	25 mM EDTA pH 8,0
HEPES buffered Tyrode's solution	119 mM NaCl
	5 mM KCl
	2 mM$CaCl_2$
	2 mM $MgCl_2 – 6\ H_2O$
	6 g/L Glucose
	25 mM HEPES (Stock 1M)
Pipette solution	125 mM K gluconate

	15 mM CsCl
	0.2 mM $CaCl_2$
	2.5 mM $MgCl_2$
	1 mM MgATP
	5 mM glucose
	0.5 mM EGTA
	4 mM Na2ATP
	0.1 mM cAMP
	10 mM HEPES (pH 7,4 and π 295 mosmol/L)
Solution A (1 L) for neuronal isolation	137 mM NaCl
	5.4 mM KCl
	0.17 mM Na_2HPO_4
	0.22 mM KH_2PO_4
Solution B (250 mL) for neuronal isolation	9.9 mM HEPES
Dissection medium (500 mL) for neuronal isolation	25 mL Solution A
	14 mL Solution B
	3 g D-Glucose
	7.5 g Sucrose

prepared in 400 mL water, then adjusted pH to 7,4 with NaOH, brought to final volume of 500 mL, sterilized with 0,2 µm filter

BSA 1 %	1 g Bovine serum albumin
	fill up with 99 mL DPBS
Fixing solution	2 mL Paraformaldehyd
	48 mL DPBS
10 % Triton X-100/PBS stock solution	10 g Triton-X-100 in 100 mL H_2O
Blocking solution	2 g BSA
	300 µL Triton-X-100
	100 mL DPBS
Poly(ethylenglycol)methyletherthiol (mPEG)	5 µM mPEG 6.000 Da in H_2O

4.2 Cells

Table 3: Mammalian Cells Used

Cell line	Origin	Culture Medium
N2a	Mouse neuroblastoma, kindly provided by Prof. Dr. rer. nat. Anaclet Ngezahayo	Complete DMEM[*1] Complete DMEM differentiation medium[*4]
HEK 293T	Human embryonic kidney cells, kindly provided by Prof. Dr. Kabesch	Complete DMEM[*1]
HEK Na_v 1.3 K_{IR} 2.1	Human embryonic kidney cells, stably transformed with voltage-gated Na+ and K+ channels	Complete DMEM[*1] + 500 µg/mL neomycine + 2 µg/mL puromycine
PC 12	Rat adrenal pheochromocytoma	RPMI 1640[*2]
Neonatal rat hippocampal neurons	isolated from Spraque-Dawley rats, kindly provided by AG Warnecke	BrainPhys Neuronal Medium[*3]
Neonatal rat cortical neurons	isolated from Spraque-Dawley rats, kindly provided by AG Warnecke	BrainPhys Neuronal Medium[*3]
Neonatal rat spiral ganglion neurons	isolated from Spraque-Dawley rats, kindly provided by AG Warnecke	BrainPhys Neuronal Medium[*3]

[*1] supplemented with 10 % FBS, 100 U/mL Pen/Strep

[*2] supplemented with 10 % horse serum (HS), 5 % FCS and 1% P/S;
for differentiation media was supplemeted with 1 % HS, 1 % P/S and 50 ng/ml hNGF

[*3] supplemented with NeuroCult SM1 (1 : 50) and 100 U/mL Pen/Strep, 25 µL of 200 mM L-Glutamine, 18.5 µL of 2 mg/mL L-Glutamic Acid to 500 mL BrainPhys Neuronal Medium

*4 supplemented with 0.5 % FCS, 100 U/mL Pen/Strep and non-essential amino acids (1:100)

Table 4: Bacterial Cells Used

Strain	Origin	Culture Medium
N2aOne Shot® Mach1™ T1 Phage-Resistant Chemically Competent E. coli	Thermo Fisher Scientific, USA	LB agar/medium
DB3.1 Chemically Competent E. coli	Thermo Fisher Scientific, USA	LB agar/medium

4.3 Chemicals and Reagents

Table 5: Chemicals and Reagents Used

Chemicals and reagents	Manufacturer
100 bp-DNA-Ladder extended	Carl Roth, Germany
10x Universal Buffer	Jena Bioscience GmbH, Germany
Agarose	Carl Roth, Germany
All-*trans* retinal	Sigma-Aldrich, Germany
Human BDNF Recombinant Protein	Thermo Fisher Scientific, USA
BrainPhys Neuronal Medium	STEMCELL Technologies Germany GmbH
Cal-630 AM	AAT Bioquest, Inc., USA
Calcein-AM	Thermo Fisher Scientific, USA
Carbenicilin Disodiumsulfat	Carl Roth, Germany
D(+)-Glucose (waterfree)	Carl Roth, Germany
Di-Sodium hydrogenephosphate dihydrate	Carl Roth, Germany
Dimethyl sulfoxide (DMSO)	Sigma-Aldrich, Germany
DMEM High Glucose	Pan Biotech, Germany
DNase I	Sigma-Aldrich, Germany
DPBS	Pan Biotech, Germany
Ethanol 70 %	Carl Roth, Germany
Ethanol 99 %	Carl Roth, Germany
Fetal bovine serum (FBS)	Merck Millipore, Germany
Fluo-4 AM	Thermo Fisher Scientific, USA
Hanks' Balanced Salt Solution 10x	Sigma-Aldrich, Germany
HEPES	Carl Roth, Germany
Hoechst 33342 trichloride trihydrate	Thermo Fisher Scientific, USA

innuSTAR 1 kb DNA Ladder Express	Analytik Jena AG, Germany
Kanamycin sulphate	Carl Roth, Germany
LB-Agar (Luria/Miller)	Carl Roth, Germany
LB-Medium (Luria/Miller)	Carl Roth, Germany
Midori Green Advance	NIPPON Genetics Europe, Germany
NeuroCul SM1 Neuronal Supplement	STEMCELL Technologies Germany GmbH
Neuronal Isolation Enzyme (with papain)	Thermo Fisher Scientific, USA
Opti-MEM	Thermo Fisher Scientific, USA
Penicillin/Streptomycin	Pan Biotech, Germany
Poly-D-Lysine	Sigma-Aldrich, Germany
Poly(ethylenglycol)methyletherthiol 6000	Sigma-Aldrich, Germany
Potassium chloride	Carl Roth, Germany
Potassium dihydrogen phosphate	Carl Roth, Germany
Propidium Iodide	Thermo Fisher Scientific, USA
Q5® Reaction Buffer	New England Biolabs GmbH, Germany
Roti®-Load DNA short-run (with glycerol)	Carl Roth, Germany
Roti®-Mix PCR 3 (dNTPs)	Carl Roth, Germany
Sodium chloride	Carl Roth, Germany
Sodium dihydrogen phosphate dehydrate	Carl Roth, Germany
SYBR Green I	Thermo Fisher Scientific, USA
Trypan Blue Solution, 0.4 %	Sigma-Aldrich, Germany
Trypsin 0.05 %/EDTA 0.02 %	Pan Biotech, Germany
Trypsin lyophilized powder	Sigma-Aldrich, Germany
ViaFect™	Promega, USA

4.4 Commercial Kits

Table 6: Commercial Kits Used

Kit	Manufacturer
FastGene® Plasmid Mini Kit	NIPPON Genetics Europe, Germany
innuPREP Plasmid MIDI Direct Kit	Analytik Jena AG, Germany
Monarch DNA Gel Extraction Kit	New England Biolabs GmbH, Germany
ZymoPURE™ Plasmid Maxiprep Kit	Zymo Research, USA

4.5 Equipment and consumables

Table 7: Consumables Used

Equipment and Consumables	Manufacturer
0.2 µm sterile filter	Sarstedt, Germany
10 x NA 0.3 air objective	Leica, Germany
20 x, NA 1.0 air objective	Olympus, Japan
60MEA100/10iR-Ti	Multi-Channel Systems MCS GmbH, Germany
40 µm Cell strainer, EASYstrainer™	VWR, USA
60 µ-Dish 35 mm, high	ibidi, Germany
Axiovert 40 C	Carl Zeiss AG, Germany
Avanti JXN30	Beckman Coulter GmbH, Germany
Bandpass Filter 470 nm/2	Thorlabs, USA
BioDrop™ DUO	SERVA Electrophoresis GmbH, Germany
Centrifuge 5427 R	Eppendorf, Germany
Centrifuge Z 206 A	HERMLE Labortechnik GmbH , Germany
Chameleon Ultra II	Coherent Inc., USA
cell culture dish 10 cm	Sarstedt, Germany
cryo tubes	Sarstedt, Germany
Culture-Inserts 3 Well	ibidi, Germany
Dissection tools	Carl Roth, Germany
disposable serological pipettes 2, 5, 10 mL	Sarstedt, Germany
Emission filter 655/40	AHF Analysetechnik, Germany
Excitation filter 606/15	AHF Analysetechnik, Germany
eppendorf reaction tubes 1.5 / 2 mL	Sarstedt, Germany
Eppendorf Research® plus pipettes 10/100/200/1000 µL	Eppendorf, Germany
falcon tubes 15 mL / 50 mL	Sarstedt, Germany
Fiber-Coupled LED M455F1 - 455 nm	Thorlabs, USA
Fluorescence microscope: Zeiss Axio Vert.A1	Zeiss, Germany
glass bottom dishes (35 mm)	ibidi, Germany
Heracell™ VIOS 160i CO_2/O_2-Inkubator	Thermo Fisher Scientific, USA

Materials

Incubator cells – HERAcell vios 160i	Thermo Fisher Scientific, USA
Inverse Leica microscope DMI6000B	Leica, Germany
Laminar flow hood – SAFE 2020	Thermo Fisher Scientific, USA
Lenses at imaging setup	Thorlabs, USA
Maxisafe 2020 Class II biological safety cabinet	Thermo Fisher Scientific, USA
MEA2100-Lite-System	Multi Channel Systems MCS GmbH, Germany
Neubauer hemozytometer	Carl Roth, Germany
Nikon Ti-E fluorescence microscope	Nikon, Germany
Nitril gloves	VWR, USA
OBIS-Laser (488 nm)	Coherent, USA
Parafilm®	Bemis Company Inc., USA
peqPOWER power supply E300	VWR, USA
peqSTAR 2X	VWR, USA
pipette tips 10/200/1000 µL	Sarstedt, Germany
ProScan II Advanced Controller	Prior Scientific, Germany
Rat tail collagen type I	Enzo, USA
Red light LED (680 nm)	Thorlabs, USA
scientific CMOS camera pco.edge 4.2	PCO, Germany
SOLIS-3C high power LED	Thorlabs, USA
SPROUT® MINI CENTRIFUGE 12V	Heathrow Scientific, USA
TSX600 Ultra-Low Temperature Freezer	Thermo Fisher Scientific, USA
XCite 120PC Q	Excelitas Technologies, USA
Zeiss Axio Observer D1	Carl Zeiss AG, Germany

4.6 Enzymes

Table 8: Enzymes Used

Enzyme	Manufacturer
BamHI	Jena Bioscience GmbH, Germany
EcoRI	Jena Bioscience GmbH, Germany
Gateway® BP Clonase® II Enzyme	Invitrogen, USA
Gateway® LR Clonase® II Enzyme	Invitrogen, USA

Materials

MluI	Jena Bioscience GmbH, Germany
Q5® High-Fidelity DNA Polymerase	New England Biolabs GmbH, Germany

4.7 Software

Table 9: Software Used

Software	Manufacturer
ImageJ	open source
MATLAB	MathWorks
Mendeley	Mendeley Ltd.
Microsoft Office Excel and Word 2016	Microsoft Corporation
Multi Channel Analyzersoftware	Multi Channel Systems MCS GmbH
Snapgene	GSL Biotech LLC

4.8 Oligonucleotides

Table 10: Oligonucleotides Used

Oligonucleotide	Sequence 5´-3´
*att*B ChR2-EGFP.FOR	GGGGACAAGTTTGTACAAAAAAGCAGGCTTAATGGACTATGGCGGCGC
*att*B ChR2-EGFP.REV	GGGGACCACTTTGTACAAGAAAGCTGGGTTTTACTTGTACAGCTCGTCCATGCCGA
*att*B Chronos-EGFP.FOR	GGGGACAAGTTTGTACAAAAAAGCAGGCTTAATGGAAACAGCCGCCACA
*att*B Chronos-EGFP.REV	GGGGACCACTTTGTACAAGAAAGCTGGGTTTTACTTGTACAGCTCGTCCATGCC
*att*B jRCamP.FOR	GGGGACAAGTTTGTACAAAAAAGCAGGCTTAATGCTGCAGAACGAGCTTG

*att*B	GGGGACCACTTTGTACAAGAAAGCTGGGTTCTACTTCGCTGTCAT
jRCamP .REV	CATTTGTACAAACT

all oligonucleotides were provided by Microsynth AG

Table 11: Oligonucleotides Used for Sequencing

Oligonucleotide	Sequence 5′-3′
*att*R1-CmR-ccdb-attR2-GFP SpeI fw	TAGTATCACTAGTGGCTAGTTAAGCTTGATCAAACAAGTTTG
*att*R1-CmR-ccdb-attR2-GFP AgeI rev	ACTTCGACCGGTTCATTATTTGTAGAGCTCATCCATGCCATGA
*att*B Insert.FOR	GGGGACAAGTTTGTACAAAAAAGCAGGCTTAATGGAAACAGCC GCCACA
*att*B Insert.REV	GGGGACCACTTTGTACAAGAAAGCTGGGTTCACTCCTCCCTCCT CCTCC

all oligonucleotides were provided by Microsynth AG

4.9 Antibodies

Table 12: Antibodies Used

Antibody	Category	Host	Manufacturer	Dilution
CamKII	primary	mouse	Abcam, USA	1:250
β-III-tubulin	primary	rabbit	Sigma-Aldrich, USA	1:2000
Synaptophysin	primary	mouse	Santa Cruz, USA	1:50
Anti-mouse Alexa fluor 555	secondary	goat	Dianova, Germany	1:3000
Anti- rab-bit Alexa fluor 488	secondary	goat	Dianova, Germany	1:4000

4.10 Plasmids and viral Particles

Table 13: Plasmids and Viral Particles Used

Plasmid and Viral Particles	Manufacturer
pDONR 221	Invitrogen
pLenti CMV Neo Dest	Addgene (17392)
pMD2.G	Addgene (12259)
pMDLg/pRRE	Addgene (12251)
pRSV-Rev	Addgene (12253)
FCK-ChR2-GFP	Addgene (15814)
pAAV-Syn-Chronos-GFP	Addgene (59170)
pMOS010: pLX304-CheRiff	Addgene (62986)
psPAX2	Addgene (12260)
pAAV.Syn.NES.jRCaMP1a.WPRE.SV40	Addgene (100848)
Ready-to-use AAV9 particles produced from pAAV.Syn.NES.jRCaMP1a.WPRE.SV40	Addgene (viral prep # 100848-AAV9)

5 Methods

5.1 Cell Culture Methods

Several cell types and lines, including competent *E.coli*, Human embryonic kidney (HEK 293T) cells, mouse neuroblastoma cell line N2a, rat adrenal pheochromocytoma cells PC 12, and primary neonatal rat hippocampal, cortica,l and spiral ganglion neurons were used in this work. HEK 293T cells for viral particle production; N2a, PC 12, and HEK Na_v 1.3 K_{IR} 2.1 cells were used to establish the optogenetic toolbox to finally probe it on primary neurons.

5.1.1 Isolation of Hippocampal and Cortical Neurons

Rat pups postnatal day three (D 3) were euthanized by decapitation. The hippocampus and cortex regions were removed and treated with Papain/DNase to receive single neurons. Single cells were purified with a cell strainer with a pore size of 40 µm and the concentration was set to approximately 1 million cells per milliliter. Neurons were cultivated in 10 µg/mL PDL coated 60 µ-Dishes. For coating, 2 mL of PDL was added to the dish and incubated for at least 1 h at 37 °C and 5 % CO_2 atmosphere. After at least 1 h, the coating solution was washed away with DPBS. The experiments were in accordance with the German Animal Welfare Legislation and approved by the local Institutional Animal Care and Research Advisory Committee and permitted by the Lower Saxony State Office for Consumer Protection and Food Safety (reference number 42500/1H).

5.1.2 Isolation of Spiral Ganglion Neurons

The dissection of the cochleae and the isolation of the SGN were conducted as described previously[142]. For enzymatic dissociation, spiral ganglion explants were incubated at 37 °C for 20 min in a solution containing 0.1 % trypsin and 0.01 % DNase I. Thereafter, mechanical dissociation was performed via trituration. After dissociation, the yield of viable cells was counted in a Neubauer cytometry chamber using the trypan blue exclusion test. Cells were set to 1 million per milliliter. Neurons were cultivated in 10 µg/mL PDL coated 60 µ-Dishes. Additionally 50 ng/mL BDNF was added to the media to ensure the survival of SGNs.

5.1.3 Cell Cultivation

All cells were cultivated at 37 °C and 5 % CO_2 atmosphere in an appropriate medium which was replaced by a new medium every third day. HEK, N2a, and PC 12 cells were cultivated in 10 cm dishes and split, if needed, every third day by washing once with DPBS, trypsinizing, resuspending in the appropriate volume of medium, and seeding into new 10 cm dishes. E.coli

cells were cultivated in LB medium or on LB agar plates at 37 °C and under specific selection pressure.

5.2 Molecular Biological and Biochemical Methods

5.2.1 Polymerase Chain reaction

To generate the destination plasmids for viral particle production, the Gateway cloning technology was used. This cloning method is based on the site-specific recombination system of the bacteriophage lambda which facilitates the integration of heterologous DNA sequences between vectors[143]. Initially, the amplification of the DNA template with specific attachment sites (*att*B) flanking primers (see Table 10) was performed employing a polymerase chain reaction (PCR) as described in Table 12. Therefore, 10x universal buffer was mixed with 0.2 mM dNTPs, 0.5 µM of forward (for) and reverse (rev) primers, 100 ng template DNA, 1 µL of high-fidelity polymerase, and filled up to 50 µL with Millipore water. Afterward, the PCR tubes were placed into the thermocycler and the PCR program was started (Table 14).

Table 14: Pipetting Scheme and PCR Program

Reagent	Volume
10x unviversal buffer	10 µL
High-fidelity	1 µL
10 mM dNTPs	1.25 µL
10 µM for primer	2.5 µL
10 µM rev primer	2.5 µL
Template DNA	100 ng
Millipore water	fill up to 50 µL

Step	Temperature	Time
initial denaturation	98 °C	30 sec
denaturation	98 °C	30 sec
annealing	60 °C	30 sec
elongation	72 °C	90 sec
		30 cycles
final elongation	72 °C	5 min
pause	4 °C	∞

5.2.2 Agarose Gel Electrophoresis and Gel Extraction

PCR samples were mixed with 1:6 loading buffer and loaded on a 1 % agarose gel/1x TAE with 1:1000 Midori green advance as a DNA dye. The current was set at 80 V for at least 40 min until the bands got clearly separated. The correct-sized *attB*-PCR products were cut out of the gel and purified using the Monarch DNA Gel Extraction Kit. In brief, 800 µL of dissolving buffer was added to the excised fragments. The fragments were incubated for 10 min at 50 °C on a shaker and loaded onto a column. After centrifugation for 1 min at 16000 x g, the flow-through was discarded and the column was washed twice with wash buffer. In the end, the

column was transferred to a clean 1.5 mL reaction tube, 10 µL elution buffer was added to the matrix and the tube was centrifuged for 1 min at 16000 x g after 1 min latency. The purity and DNA concentration was determined using the BioDrop photometer.

5.2.3 Gateway Clonation

To generate an entry clone, a BP recombination reaction was performed (**Fig. 13**) according to the manual from Invitrogen (Landy, Bernard, & Couturier, 1989[144]). In brief, 100 ng purified *att*B-PCR product was added to 150 ng *att*P containing donor vector (pDONR 211) and filled up with TE buffer to a total volume of 8 µL. To catalyze the reaction, a 2 µL BP Clonase™ II enzyme mix was added to the solution and incubated for at least 1 h at 25 °C. The enzyme mix contains the bacteriophage lambda recombination protein Integrase (Int) and the *E.coli*-encoded protein Integrase Host Factor (IHF) which mediates the generation of an *att*L-containing entry plasmid. To stop the recombination, 1 µL of the proteinase K solution was added and incubated for 10 min at 37 °C. The generated *att*L entry clone served as a template for the creation of the *att*R containing the expression vector. To do so, 100 ng purified *att*L entry clone were added to 150 ng *att*R containing destination vector (pLenti CMV Neo Dest) and filled up with TE buffer to a total volume of 8 µL. The destination vector also contains a *ccd*B suicide cassette, allowing for a negative selection of untransformed *E.coli*. To catalyze the reaction, 2 µL LR Clonase™ II enzyme mix was added to the solution, well mixed, and incubated for at least 1 h at 25 °C. The enzyme mix contains the Int and IHF proteins, as well as the Excisionase (Xis) protein which together mediate the generation of an *att*R-containing expression plasmid. For stopping the reaction, 1 µL of the proteinase K solution was added and incubated for 10 min at 37 °C. Competent *E.colis* were transformed as described in section 5.2.4. and selected for expression clones on petri dishes containing LB agar, supplemented with 200 µg/mL carbenicillin.

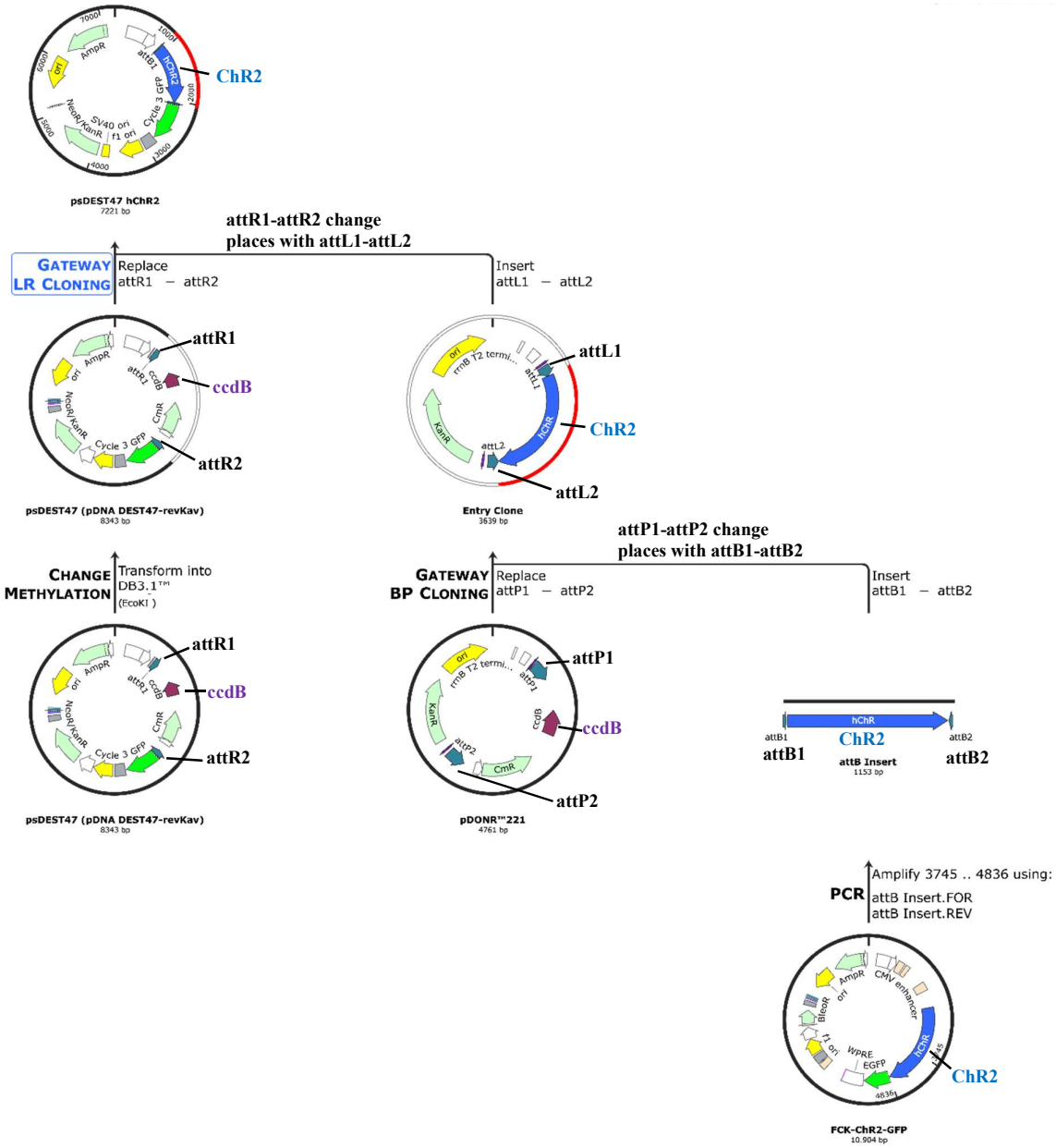

Fig. 13 BP and LR Recombination Reaction from the DNA Template to the Final Construct

The illustration from SnapGene displays exemplary the chronological process of the BP and LR reaction, starting from the FCK-ChR2-GFP DNA template, generation of an *att*B containing insert via *att*B primers, the integration of the insert into an *att*P containing donor vector (pDONR 211) via the BP Clonase™ II enzyme mix to obtain the *att*L containing entry clone. The LR reaction, whereas the LR Clonase™ II enzyme mix catalyzes the recombination from the *att*L containing entry clone with the *att*R containing destination vector (pLenti CMV Neo Dest) to generate the expression vector (psDEST47 hChR2). The *ccdB* suicide gene on the donor vector allows negative selection for untransformed E.colis In the same manner, the expression plasmid psDEST47 Chronos was produced.

5.2.4 Transformation of *E. coli*

An amount of 50 µL chemically competent *E.coli* was defrosted on ice and the whole BP reaction product was added to the bacteria suspension. After incubation on ice for 30 min, a heat shock at 42 °C for 45 s was performed. Afterward, 250 µL of LB medium were added and the mixture was incubated for 1 h at 37 °C on a shaker. 100 µL of the bacteria suspension were plated on a petri dish containing LB agar, supplemented with 50 µg/mL kanamycin, and incubated at 37 °C overnight. The presence of the *ccd*B suicide gene on the donor vector allows negative selection for untransformed E.colis.

5.2.5 Plasmid Isolation – Mini Preparation

Bacteria colonies were picked from the LB agar dish and incubated in 10 mL LB medium supplemented with 50 µg/mL kanamycin for 24 h at 37 °C on a shaker. By means of the FastGene® Plasmid Mini Kit, around 3 mL of the overnight cultures were transferred into 2 mL reaction tubes and centrifuged for 2 min at 11000 x g. The supernatant was discarded, the pellet resuspended in 200 µL cold mP1 buffer and another 200 µL mP2 buffer were added. After inverting the tubes and an incubation time of less than 5 min, 300 µL of mP3 buffer were added and the samples were centrifuged for 2 min at 11000 x g. The clear supernatant was transferred onto a column and centrifuged for 30 s. Hereafter, the membrane of the column was washed with 400 µL mP4 and 600 µL mP5 and completely dried due to spinning for 2 min. Finally, the entry clone plasmids were eluted with 25 µL mP6 by centrifugation for 2 min and the DNA concentration was measured.

5.2.6 Plasmid Isolation – Maxi Preparation

Bacteria colonies were picked from the LB agar dish and incubated in 200 mL LB medium under the selection pressure of 200 µg/mL carbenicillin for 24 h at 37 °C on a shaker. By means of the ZymoPURE™ Plasmid Maxiprep Kit, 200 mL of the overnight cultures were transferred into 50 mL falcons and centrifuged for 10 min at 4000 x g. The supernatant was discarded and the bacteria pellet resuspended with 14 mL P1 buffer until pellets were resolved. 14 mL of P2 buffer were added to the solution, the falcon inverted and incubated for less than 5 min at RT. Then 14 mL of P3 buffer were mixed with the suspension and the lysate loaded into the ZymoPURE™ Syringe Filter. After 5 min, the Luer lock plug was removed and the solution was pushed through the filter. Hereafter, 14 mL of binding buffer were mixed with the flow-through and stepwise loaded onto the V-P column. After centrifugation at 500 x g for 2 min, the V-P column was first washed with 5 mL Wash1 and then with 5 mL Wash2. To remove any residual wash buffer, the V-P column was placed into a 1.5 mL reaction tube and centrifuged

for 1 min at 11000 x g. Finally, the DNA was eluted from the column matrix twice with 200 µL elution buffer by centrifugation for 1 min and the DNA purity and concentration were measured.

5.2.7 Lentivirus Production

For lentivirus production, 5 x 10^6 HEK 293T cells were seeded in a 10 cm dish with complete DMEM and incubated at 37 °C and 5 % CO_2 atmosphere. The next day, the medium was replaced with 10 mL complete DMEM supplemented with 25 µM chloroquine and 20 mM HEPES. All components of the lentiviral split packaging system: 20 µg psPAX2 (contains the HIV-*pol*, HIV-*gag,* and HIV-*tat* genes), 11 µg VSV-G (pMD2.G), and 18 µg of the expression vector (pMOS010: pLX304-CheRiff). The three plasmids are transfected in equimolar amounts (approximately 2.9 pM) with polyethylenimine (PEI), so that the same number of copies of each plasmid are present in the transfection medium. For the transfection, the DNA was mixed in 1.5 ml of OptiMEM. 80 µl of PEI (1 mg/ml) was diluted in 1.5 ml of OptiMEM. After 5 min incubation at RT, the diluted PEI was added to the mixed DNA. The DNA-PEI mixture was incubated for 20 min at RT. In the meantime, the medium on the HEK 293T cells was changed to 5 ml OptiMEM. After incubation, the DNA-PEI mixture was added dropwise to the cells and the dish was rocked carefully so the DNA-PEI complexes could spread evenly on the cells. Then the cells were incubated for 5 h at 37 °C at 5 % CO_2 in a humidified incubator. Afterward, the transfection medium was changed to 11 ml full growth medium and the transfected cells were incubated for 48 h. After incubation, the viral supernatant was harvested and fresh media was added to the cells for further incubation. The harvested supernatant was first centrifuged at 3400 x g 15 minutes at 4 °C to remove cell debris. The supernatant was further filtered through a 0.22 µm filter unit and centrifuged for 2 h at 100.000 x g. The supernatant was discarded and the tube was inverted and stored on a tissue to become dry. The pellet is solved with 300 µL DPBS and stored in 10 µL vials at - 80 °C. This procedure was repeated after 72 h of incubation.

5.2.8 Viral Transduction

For transduction of cell lines (HEK 293T, PC 12, and HEK Na_v 1.3 K_{IR} 2.1) infectious transgenic lentviral particles were produced. A total amount of 2 x 10^5 cells in 1 mL corresponding media was mixed with one viral vial (refer to 5.2.7) and 6 µM polybrene to enhance transduction efficiency. The cells were then seeded into a 35 mm glass-bottom dish. After 24 h of transduction, the medium was changed to a full growth medium. Experiments were performed 5 days after transduction. To deliver the opsin CheRiff to the primary neurons, they were cultured in a poly-D-Lysine coated 35 mm imaging dish with a polymer coverslip,

usually in 3 well silicone chambers. On DIV 1, one viral vial was mixed with 300 µL of media, and 70 µL of the virus-containing suspension was added to the cells. After 24 h of incubation, the virus-containing solution was removed and after a washing step, to remove residual lentivirus, replaced with fresh media. Further, the silicone inserts were removed and the three populations were infected with ready-to-use AAV9 particles (refer to 4.10) in a ratio of 1:100 (Titer $\geq 1\times10^{13}$ vg/mL).

5.2.9 Immunostaining of Neurons

To determine the amount of glutaminergic excitatory neurons of one isolation, freshly isolated hippocampal neurons were stained with antibodies against β-III-tubulin and CamKII. The immunofluorescence staining was performed by an indirect two-step method. The samples were fixed in 4 % paraformaldehyde for 1 h and permeabilized with 0.5 % Triton X-100/PBS. Nonspecific antibody binding was inhibited by applying a 2 % bovine serum albumin/PBS solution for 2 h at 37 °C. After blocking, the samples were incubated with the primary antibodies (refer to table 12) and diluted 0.5 % Triton X-100/PBS overnight at 4 °C. After several washing steps, the samples were incubated with a fluorescence-conjugated secondary antibody at an appropriate dilution (refer to table 12) for 2 h at 37 °C. Cell nuclei were stained with Hoechst 33342. Neuronal samples were washed three times and stored in PBS prior to confocal microscopy.

5.3 Electrophysiological Methods

5.3.1 Whole-Cell Patch-Clamping

For patch-clamp experiments, 3 x 10^4 ChR2 transfected N2a cells were cultured on collagen I-coated coverslips in 24-well plates. One hour before patch-clamp experiments, 100 nM retinal was added to the cells. The cell-covered coverslip was transferred into a perfusion chamber filled with 400 µL of bath solution (refer to 4.1), which was mounted on an inverse fluorescence microscope. The patch pipettes were filled with a pipette solution (refer to 4.1). Filled pipettes had an electrical resistance of 2–5 MΩ. Whole-cell patch-clamp experiments were performed with the EPC 10 USB double patch-clamp amplifier. After establishing a whole-cell configuration on the cells, blue light pulses of different time intervals were applied to the cells, and changes in membrane voltage were recorded.

5.3.2 Multi-Electrode Array

For extracellular recordings and thus broader network dynamics of neural activity, primary neurons were seeded directly on PDL-coated MEA surface. Hippocampal and cortical neurons were isolated as described in 5.1.1 and ~5000 cells/mm^2 were plated onto the recording field of

the MEA. The cells were incubated at 37 °C and 5 % CO_2 for 5 days before recording experiments. After 24 h of incubation, cells were transduced with CheRiff. For optogenetic stimulation experiments, a blue LED was placed over the sample and 100 ms pulses with 60 Hz were applied, controlled by a shutter. The growth media was changed every two days. MEA data was analyzed with the Multi-Channel Analyzer software.

5.4 Optical Methods

5.4.1 Calcium Imaging

Calcium staining was performed to record changes of intracellular Ca^{2+} upon channelrhodopsin (ChR2, Chronos, and CheRiff) mediated action potentials (refer to 2.3). For staining with Fluo-4 AM for N2a cell experiments, 3 x 10^5 ChR2 or Chronos - N2a cells/dish were seeded into 35 mm glass-bottom dishes. On the day of measurement, cells were incubated with 100 nM all-*trans* retinal 1 h before staining. Thereafter, cells were washed with OptiMEM once and the dye solution, consisting of 1.8 µM Fluo-4 AM and OptiMEM was added to the cells. After 20 min of incubation, the dye solution was removed and replaced by Tyrode's solution. After a further 20 min of incubation, imaging experiments took place. For calcium imaging experiments with PC 12 and HEK Na_v 1.3 K_{IR} 2.1 cells, Cal-630 AM, a red-shifted chemical calcium dye, was used. The staining process of HL-1 cells will be explained in detail in section 5.6. Five to seven days before calcium imaging, the cells were transduced with a virus containing the pLX304-CheRiff plasmid (refer to 5.2.8). Successful transduction was verified by observed GFP expression, as *GFP* is the reporter gene linked to CheRiff. Before staining, the cells were treated with 100 nM all-*trans* retinal and incubated for one hour. For dye loading, 50 µg of Cal-630 AM were diluted in 8 µl dimethyl sulfoxide (DMSO) to obtain a 5 mM stock solution. Two µl of the stock solution were diluted in 1 ml of growth medium. The cells were seeded at a density of 3 x 10^5 cells in glass-bottom dishes or collagen-coated µ-dishes 35 mm and were stained with 10 µM Cal-630 AM, respectively. The cells containing the staining solution were incubated for 1 h at 37 °C in a humidified incubator with 5 % CO_2. The staining solution was then changed to 1 ml Tyrode's solution or HBSS with 10 mM Ca^{2+} and the cells were further incubated for 30 min before imaging. Calcium imaging with the GECI jRCaMP1a will be explained in detail in section 5.5.

5.4.2 Experimental Setup Calcium Imaging with Cal-630 AM

The setup used for calcium imaging experiments with Cal-630 AM was built in cooperation with Prof. Czarske and Felix Schmieder (TU Dresden)[145] and kindly provided by Dr. Maria Leilani Torres. **Fig. 14** depicts a detailed schematic drawing of the setup. Briefly, the stimulation

laser is guided through the setup by a fiber. A neutral density filter adjusts the laser power. Subsequently, the laser beam passes through several lenses (L1-3), which magnifies the beam until it finally arrives in a spatial light modulator (SLM). The SLM is a ferroelectric liquid crystal that responses depending on the polarization of the light. To adjust the laser light properly, lambda halfway plate (λ/2) and linear polarizer (LP) are built between L1 and L2. The SLM rotates the light phase by $\pi/3$, which then allows it to go through the polarizing beam splitter (PB). Then the laser beam is again focused by L4 on the substrate/cells. Before the laser beam hits the EMCCD camera, it is sent through an emission filter (EmF, 655/40), so it does not damage the camera. An additional LED is installed to get a bright-field image of the cells and is guided through the dichroic mirror (DM) 1 into the setup and focused through L4. Then the light is corrected by an objective before it is recorded by the EMCCD camera. The XCite 120P is a broadband light source, which is used to excite the Cal-630. The light is filtered through an excitation filter (ExF) (606/15) so only desired wavelength to excite the Cal-630 AM reaches the cells through DM2. This light is then absorbed by the Cal-630 and it emits light with a maximum of 625 nm, which in turn is collected by an objective and filtered through the same EmF as the Laser before it is captured by the EMCCD. The recordings were made with the Andor Solis software with an exposure time of 0.05 s and a 2x2 binning to reach a recording rate of 14.041 Hz. Six hundred pictures were taken and saved as Tagged Image File Format (tiff) stacks. The cells were excited every 5 s with a 10 ms laser beam.

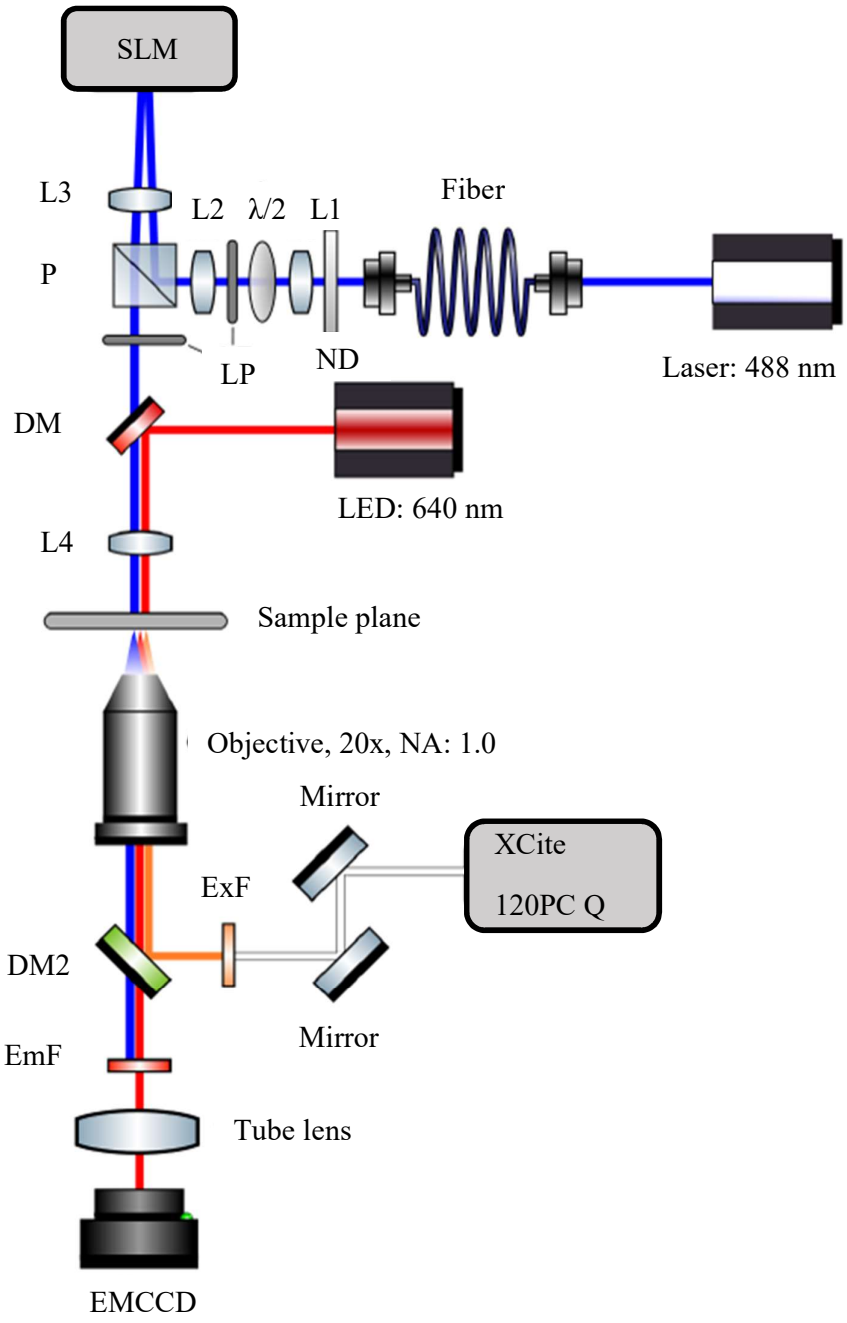

Fig. 14 Setup for Calcium Imaging with Cal-630 AM

Schematic representation of the imaging setup to probe calcium changes in cells via optogenetic stimulation. The Laser excites the cells on the sample plane at 488 nm. The Cal-630-AM dye is excited by an XCite 120PC Q lamp through an excitation filter (ExF) with 606/15 nm and the images are taken through an emission filter (ExF) with 655/40 nm. The images are taken with an EMCCD camera. L1-4: Lenses; ND: Neutral density filter; λ/2: Half-way plate; LP: Linear polarizer; PB: Polarizing beam splitter; SLM: Spatial light modulator; DM1-2: Dichroic mirror; EmF: Emission filter; ExF: Excitation Filter.

5.5 Probing Inter-Neuronal Connections via Optogenetic Stimulation

To examine the nature of inter-neuronal communication, for example of hippocampal and spiral ganglion neurons, a setup had to be established enabling both, stimulation and recording from spatially separated populations of neurons with single-cell readout. With the spectrally blue-shifted channelrhodopsin CheRiff in combination with the red-shifted GECI jRCaMP1a, it is possible to stimulate a sub-section of a neuronal network and record the calcium response in both stimulated and non-stimulated neurons at the same time[146]. Following this idea, a 35 mm imaging dish with a polymer coverslip was coated with PDL for 24 h. The PDL was removed the next day, usually the day of cell isolation, and the dish was washed three times with water. After a drying step of one hour in the laminar flow hood and a 3 well silicone chamber was placed in the middle of the dish. For better visualization, a schematic scheme of the experimental setup is shown in **Fig. 15**. During the drying process, primary neurons were isolated as described in 5.1.1 and 5.1.2 respectively. 70 µL of cell suspension, either hippocampal (HN), spiral ganglion (SGN), or cortical neurons (CN), were pipetted in the predetermined silicone chamber. After 24 h of incubation, cells were washed one time with DPBS to get rid of dead cells and cell debris, and fresh media was added. The media of HNs and CNs was at this point supplemented with lentivirus containing the opsin CheRiff. The following day, the virus-containing solution was removed and, after a washing step with DPBS, replaced with fresh media. Further, the silicone insert was removed and the three neuronal populations were infected with ready-to-use AAV9 particles to deliver the GECi jRCaMP1a. Every two to three days half of the media was removed and replaced with fresh media. To ensure the survival of SGNs, 50 ng/mL BDNF was added to the media. After 10 days of incubation, all-*trans* retinal was added once to the media. The stimulation and imaging took place on DIV 12 – 14 in Tyrode's Solution.

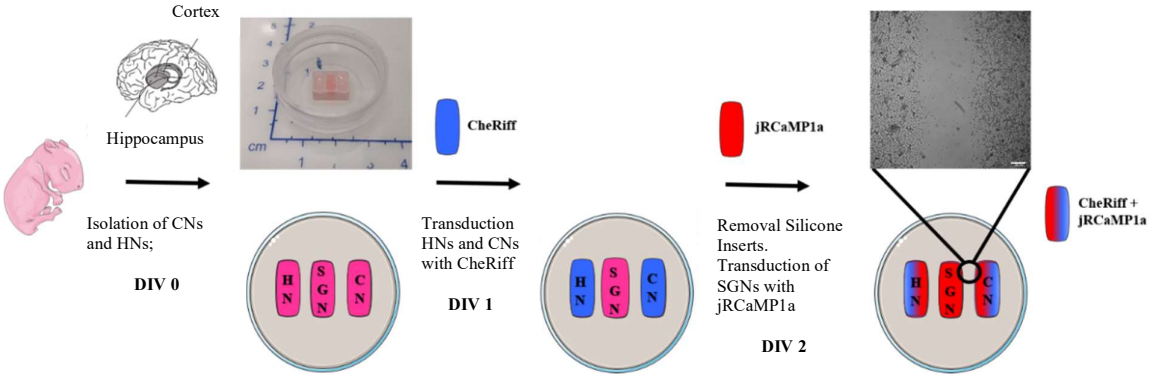

Fig. 15 Schematic Representation of the Experimental Setup to study Inter-neuronal Communication

Cortex neurons (CN) and hippocampus neurons (HN) were isolated and, together with spiral ganglion neurons (SGN), cultivated in separated silicone chambers (inserts) for 24 h. The following day (DIV 1) the HNs and CNs were loaded with lentivirus carrying CheRiff. On DIV 2 the silicone inserts were removed and all three neuronal populations were transduced with the calcium sensor jRCaMP1a via an adeno-associated vector AAV. A bright-field image of the neurons shows the gap between two neuronal groups (SGN and CN) after incubation with a 3 well silicone insert. The stimulation and imaging experiments took place at DIV 12 – 14. (Heeger et al. 2021). Scale bar indicates 100 µm.

5.5.1 Experimental Setup Calcium Imaging in Neurons

For the neuronal imaging experiments with the genetically encoded calcium indicator jRCaMP1a, the neurons were transferred to an imaging setup consisting of an inverse Leica microscope equipped with a scientific CMOS camera, high power LED for fluorescence imaging, and a fiber-coupled LED (25 mW; 470 nm) for stimulation (**Fig. 16**). To ensure that the LED delivers the right wavelength to the sample, a bandpass filter (BF) of 470 nm was coupled between the sample plane and LED. The samples were magnified using a Leica 10x NA 0.3 air objective and for recording an sCMOS camera was used. An Arduino control unit ensured synchronization of the camera and the LED. The manipulation LED was fixed directly above either an HN or a CN population. Three spots per population were stimulated with four different pulse durations (10 ms; 100 ms; 250 ms; 500 ms;). Each recording consisted of 10 pulses of blue light separated by an interval of 5.5 s. Simultaneously, calcium imaging with continuous green light illumination (570 nm, 15 mW/cm^2) through a filter (long pass emission filter > 590 nm) at 10 fps for a total duration of 1 min took place in the region of interest. More precisely, a section showing the change in fluorescence from jRCaMP1a, either HN or CN, as well the responding SGNs. Following the acquisition, the recordings were processed using an in-house built Matlab script. For each curve, a low order polynomial was fitted to remove any trend in the baseline. The peaks were detected based on the difference of the maximal and average fluorescence values with a customized threshold level.

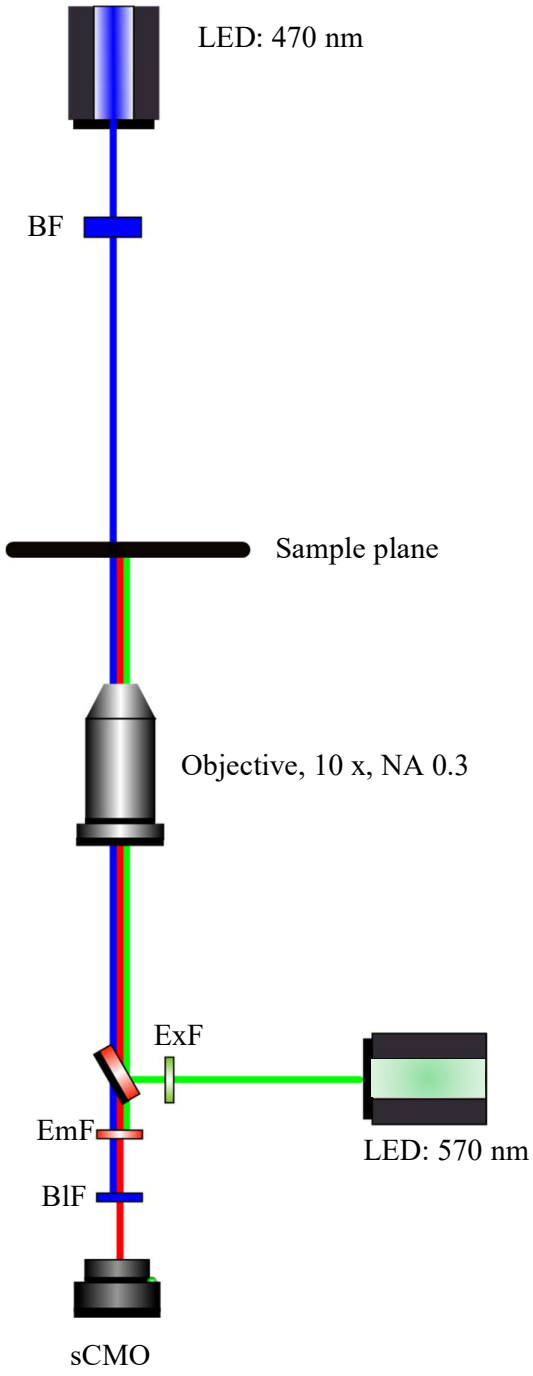

Fig. 16 Imaging Setup to probe Inter-neuronal Communication

Schematic drawing of the imaging setup for all-optical stimulation and readout. The imaging setup is based on an inverted Leica confocal microscope. The blue LED stimulation light, filtered by a 470 nm bandpass filter (BF), excites the cells on the sample plane. The GECI jRCaMP is excited by a high power-LED through an excitation filter (ExF) with 565/24 nm. The so produced fluorescence light is filtered through an emission filter (EmF) cut off >590 nm. An additional blocking filter (BlF) ensures the safety of the camera. Recordings are performed with 10 fps using a PCO sCMOS Camera.

5.6 Gold Nano Layers for structured Cell Growth

5.6.1 Generation of Gold-Coated Cover Slips (AuCS) for structured Cell Growth

To ensure structured cell growth and thus directed signal transmission for later neuronal propagation experiments, an acetone cleaned glass cover slip was sputter coated with a thin gold layer and subsequent treated with poly(ethylenglycol)methyletherthiol (mPEG). mPEG forms covalent bonds with the gold film and creates a hydrophobic layer that is repellent to hydrophilic cells[147]. To generate a simple mask for sputtering a 3D printer (Ultimaker 2) was used. It deposits layers of a thermoplastic polyactic acid (PLA) to build 3-dimensional (3D) objects. The object was modeled using computer-aided-design (CAD) software and translated into movement instructions for the 3D printer in a process called slicing. The companion software to the Ultimaker 2 extended+ 3D printer was used to ultimately print the parts.

For the generation of laser-ablated structures, a pulsed picosecond laser with wavelength of 532 nm and a maximum output power of about 80 mW was used. The pulsed laser enable ablation of the gold film through precise heating and resulting evaporation. The same setup was previously used for gold nanoparticle mediated laser transfection (GNOME) in our labs[148]. The accompanying software is design to ablate repetitive rectangular shapes. Typically, an output power of 50 mW was used for the ablation of 30 nm thick gold monolayers.

5.6.2 Cell Attachment Experiments on Laser-patterned Gold Cover Slips

The generated gold-coated coverslips (AuCS) were then seeded with HL-1 cells. Due to its cardiac morphologic, biochemical, and eletrophysiological properties, it is a suitable and convenient model for communication and calcium wave propagation studies[149]. For cell growth experiments the AuCS were placed in a 24-well plate and covered with 400 µl of varying concentrations (0.1 - 5 µM) mPEG with different sizes (Mn 1000 Da; 6.000 Da; 50.000 Da) diluted in H_2O. The cover slips were then placed in an incubator for three hours at 37 °C and 5 % CO_2. The mPEG forms a covalent bond with gold via its thiol group, making the gold coated areas hydrophobic, thereby repellent for cells. After a washing step with PBS the gold slides can be seeded with cells and drying should be prevented. From a prepared cell suspension of HL-1 cells (1 mio/mL) 150.000 cells in 160 µL were applied to the prepared gold slides. The colonized cover slips were incubated at 37 °C and 5 % CO_2 for 24 h as not other mentioned. On the following day, the media was removed along with non adherent cells and filled up with fresh media. After 72 h of incubation, images and recordings were taken.

5.6.3 Optogenetic Stimulation in Combination with Laser-patterned Gold Cover Slips

For optogenetic stimulation experiments ChR2-HL-1 cells were seeded on the gold structures generated as described above. The samples were imaged using a 5x air objective. To detect changes of intracellular Ca^{2+} concentration upon cell communication, calcium staining was performed with Cal-630 AM. By entering the cell the AM is cleaved by esterases facilitating fluorescence with an excitation maximum at 608 nm and emission maximum at 625 nm. A 5 µM stock solution in DMSO was prepared and cells were stained in growth media with 10 µM Cal-630 AM for 1 h in 37 °C in a humidified incubator with 5 % CO_2. The staining solution was then removed and replaced by HBSS with 10 mM Ca^{2+}. For imaging, the cells were moved to the imaging setup used before (5.5.1). The manipulation LED was fixed directly above the stimulation area. One spot per trail was stimulated with a pulse duration of 100 ms. Each recording consisted of 10 pulses of blue light separated by an interval of 5.5 s. Simultaneously, calcium imaging with continuous green light illumination at 10 fps for a total duration of 1 min took place. The whole area was imaged, showing the change in fluorescence from Cal-630 AM.

6 Results

The goal of this thesis was to establish a system to study spread of excitation and thus communication in inter-neuronal networks between different cell types coming from different functional units. For this, an all-optical stimulation and readout system consisting of a blue excitable channelrhodopsin variant (CheRiff) and a red shifted calcium indicator (jRCaMP1a) needed to be established first. Next, optogenetically activated excitatory hippocampal neurons (HNs) or cortical neurons (CNs) where connected to spiral ganglion neurons (SGNs) carrying jRCaMP1a, resulting in an optogenetic neuronal-tandem trigger system. Finally, the signal transmission should take place in a directional manner. For this, a simple structured cell growth system based on gold-coated coverslips (AuCS) and cell repellent mPEG was constructed. Probing of moving calcium waves of optogenetically triggered HL-1 cells proved the functionality of this system.

6.1 Establishment of an Optogenetic Tool Kit for the Stimulation of separated Cell Populations

For the first optogenetic proof of concept studies, a mouse neural crest-derived cell line Neuro 2A (N2a) was chosen. A suitable vector was assembled via the Gateway cloning System (refer to 5.2.3). The ChR2 fragment was amplified from FCK-ChR2-GFP and inserted into a vector with a broad expressing the CMV promoter, a commonly used promoter for the production of high-level recombinant protein in mammalian cells[150] and thus cell lines like N2a cells. The resulting vector has an additional antibiotic resistance marker giving cells resistance to Neomycin and a *GFP* tag. The same procedure was done with Chronos, a fast member of the ChR family (Table 1). To verify the functionality of the cloned plasmids (psDEST47 hChR2 and psDEST47 Chronos), N2a cells were transfected and the expression of the reporter GFP was verified (**Fig. 17**).

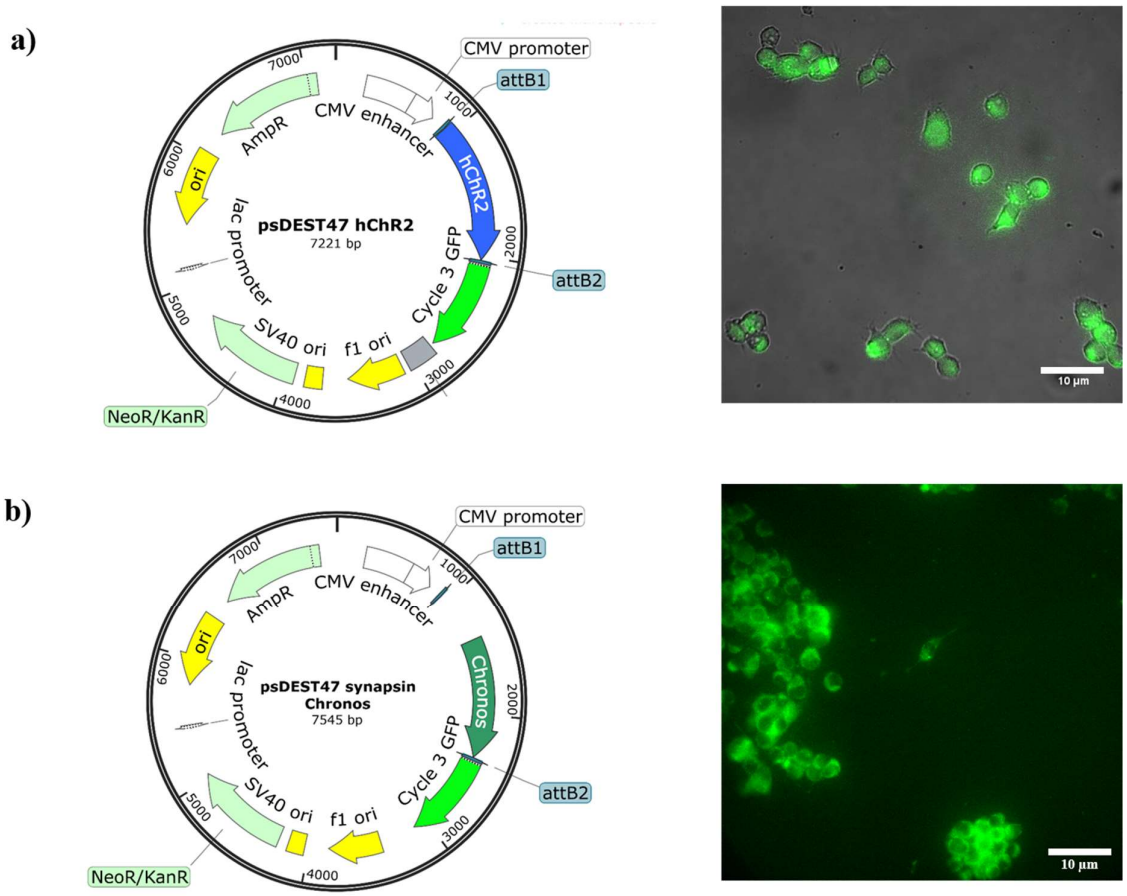

Fig. 17 Expression of ChR2 and Chronos in N2a Cells

Plasmid cards of the Gateway cloning assembled Chr2 (a) and Chronos (b) vectors and the corresponding GFP expression in N2a cells. A broad CMV promoter facilitates the expression of the gene of interest, either ChR2 or Chronos. The reporter gene *GFP* enables later detection of the transgene. Transfection of N2a cells with the assembled plasmids shows broad expression in all cells, both in ChR2 and Chronos. Scale bar indicates 10 µm

As already mentioned, the N2a neuronal-derived cell line allowing it to differentiate, in response to environmental factors, into neuronal like cells. The differentiated cells have many properties of neurons, like a resting potential of approximately -75 mV, the presence of neurofilaments, plus they show substantial endogenous TTX-sensitive Na_V currents making it a good candidate for first electrophysiological experiments[151]. For differentiation, the cells were incubated 48 h in growth media with 0.5 % FCS and non-essential amino acids (1:100). One hour prior to patch-clamp recordings, cells were supplemented with 100 nM retinal. In order to validate the functionality of the constructs, voltage-clamp recordings of ChR2 and Chronos transfected N2a cells to fluorescent light stimulation were performed (**Fig. 18**).

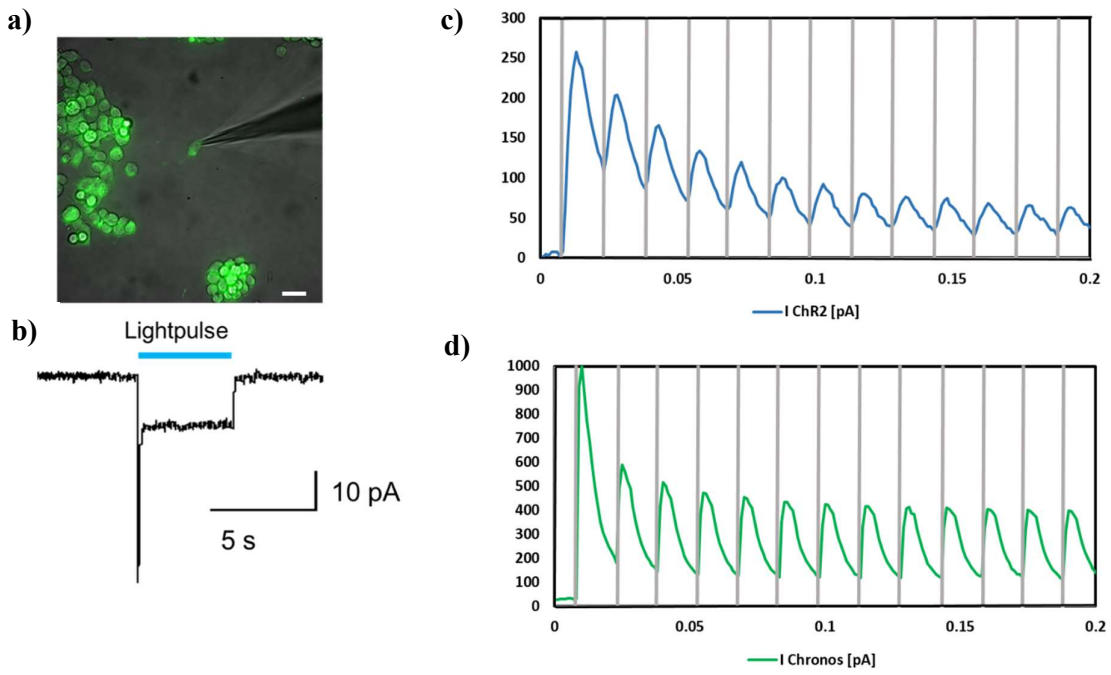

Fig. 18 Voltage-Clamp Recordings of ChR2 and Chronos transfected N2a Cells

Transfected N2a cells with ChR2 with an attached patch pipette (a) and the recorded answer to a 5 s blue light stimulus (b). N2a cells transfected with ChR2 (c) and Chronos (d) were measured with 60 Hz stimulation pulses. Scale bar indicates 10 µm.

The experiments were conducted in dark and pulsed fluorescent light (~ 10 mW/mm^2) either 470 nm for ChR2 or 550 nm for Chronos experiments were applied. By applying 60 pulses/s light pulses and current answers were synchronous as well for ChR2 and Chronos cells (**Fig. 18 c**). The maximum measured current was 1000 pA for Chronos and 260 pA for ChR2 respectively. From there, the current decreases constantly and reaches a plateau at 200 pA after 30 s (not shown). For ChR2, the maximum measured current was 260 pA. The measured current rapidly desensitizes to a still large steady-state photocurrent of 80 pA.

In order to yield contact-free measurements, the first proof of concept calcium imaging of N2a cells with Fluo-4 AM dye was performed at this point. Calcium imaging is widely used to probe neuronal connections. Calcium works here as a second messenger, since voltage-gated Ca^{2+} channels open during an action potential and a calcium-dependent-calcium release is induced. By entering the cell, the non-fluorescent acetoxymethyl ester is cleaved, giving free the fluorescent Fluo-4, which enhances its fluorescence intensity by binding Ca^{2+}. Under continuous blue light illumination, a short laser pulse of one second (532 nm; 40 mW) was applied after 20 s to either one N2a cell transfected with ChR2 or Chronos and the response was

recorded (**Fig. 19**). After the stimulation pulse, both recorded cells show an increased fluorescent signal. However, this effect is more profound in the N2a-Chronos cell than in N2a-ChR2. In addition, in the N2a-ChR2 cell, an increasing fluorescent signal can be observed even before stimulation with the laser pulse. Together, these findings confirm the feasibility of functional optogenetics in a mammalian cell line like N2a.

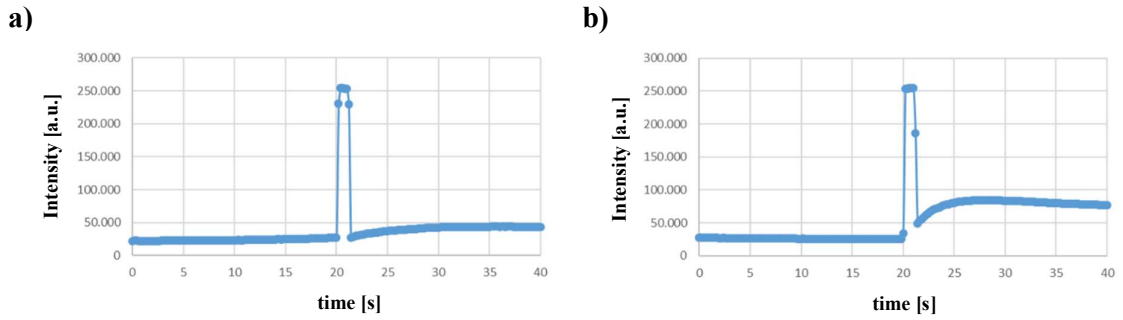

Fig. 19 Calcium Imaging of Optogenetic N2a Cells with Fluo-4 AM

Optogenetic N2a cells, either transfected with (a) ChR2 or (b) Chronos, were stimulated with a 1 s lasting laser pulse (532 nm) after 20 s of continuous blue light illumination to excite the fluorescent dye. ChR2 cells show a low response after laser stimulation, whereas Chronos shows a more intense increase in fluorescence after stimulation with the laser pulse.

6.2 Introduction of an all-optical Stimulus-Response System

As the next step towards a contact-free approach for probing cell communication was to establish a blue-shifted ChR, namely CheRiff, in combination with the red chemical calcium indicator Cal-630 AM to allow for simultaneous stimulation and recording without unwanted cross stimulation of the opsin during imaging. Since no action potentials were observable during patch-clamp measurements of N2a, it was decided to change the cell line to PC 12 cells. PC 12 cells, in their differentiated state, are a well-studied model for neuronal networks and established methods on these cells should be easily transferable to primary neurons later on[152]. By adding hNGF into the growth media, PC 12 cells start to differentiate and after three days of differentiation, a network formation becomes visible, which extends during the next days (**Fig. 20**).

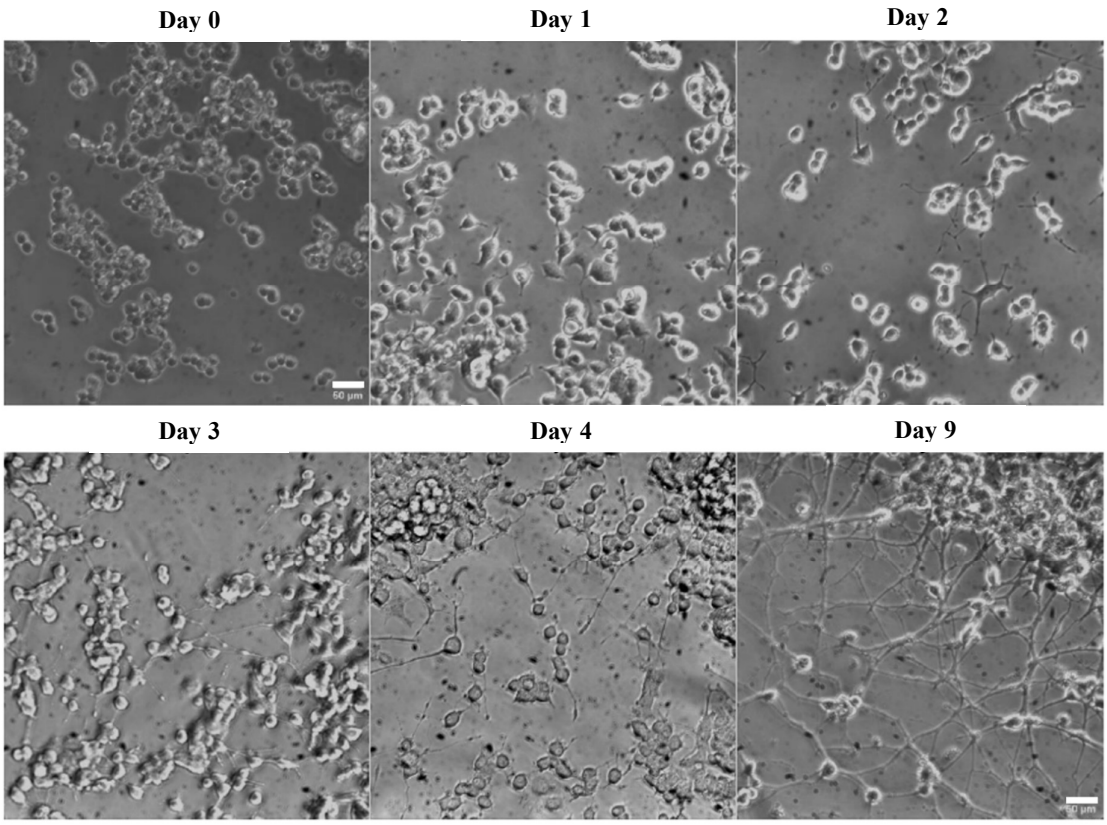

Fig. 20 Differentiation of PC 12 Cells

PC 12 cells during differentiation with 50 ng/ml hNGF from 4 h after seeding (Day 0) up to 9 days in differentiation media. Already on the second day of the differentiation process, the cells start to form protrusions and start to form connections on day 4. After 9 days of incubation in the differentiation medium, a network formation is already visible. Scale bar indicates 50 µm.

In parallel, a lentivirus transduction system was introduced, since viral genes can be transferred into non-dividing cells like neurons, which is difficult with common transfection methods like lipofection. Additionally, viral transduction has the advantage that the gene transfer is more stable due to integration into the host genome. Virus was produced with the plasmid pLX304-CheRiff in HEK 293T cells. The CheRiff has a GFP tag, so it could be detected visually and a qualitative statement of the expression can be made. After harvesting and concentration of the viral supernatant, it was further tested on the HEK 293T cells. Five days after transduction, the cells were stained with Hoechst and the percentage of transduced cells was calculated. A representable example of transduced cells is shown in **Fig. 21**. In this example, a total of 224 cells and 107 GFP positive cells were counted. This results in 47.77% transduced cells in this image. Additionally, a stronger GFP signal is detectable at the edge of the cells, rather than

in the cytosol, indicating the successful transportation of CheRiff to the plasma membrane. The GFP expression rate though is unevenly distributed.

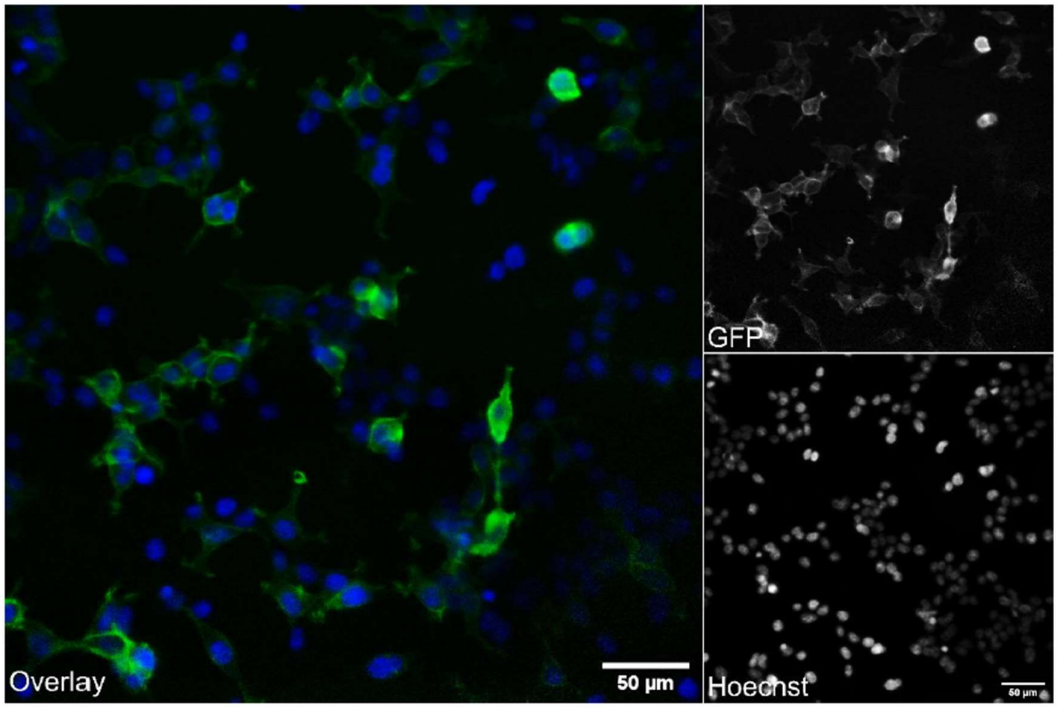

Fig. 21 Transduction Efficiency of CheRiff in HEK 293T Cells

Example of transduction efficiency in HEK 293T cells with CheRiff. The transduction rate was determined by counting. The Hoechst signal represents the nuclei of all cells and the GFP signal represents the transduced cells. Scale bar indicates 50 µm.

After the positive evaluation of the lentivirus transduction system in HEK 293T cells, *CheRiff* was also introduced into PC 12 cells. After differentiation, the cells were transduced with a virus carrying *CheRiff*. After six days of transduction and five days of differentiation, the cells showed a transduction rate of 80 % (**Fig. 22**). Additionally, the GFP signal is localized at the plasma membrane, indicating integration of the opsin into the membrane. The expression is also more profound in somatic regions than in the extensions.

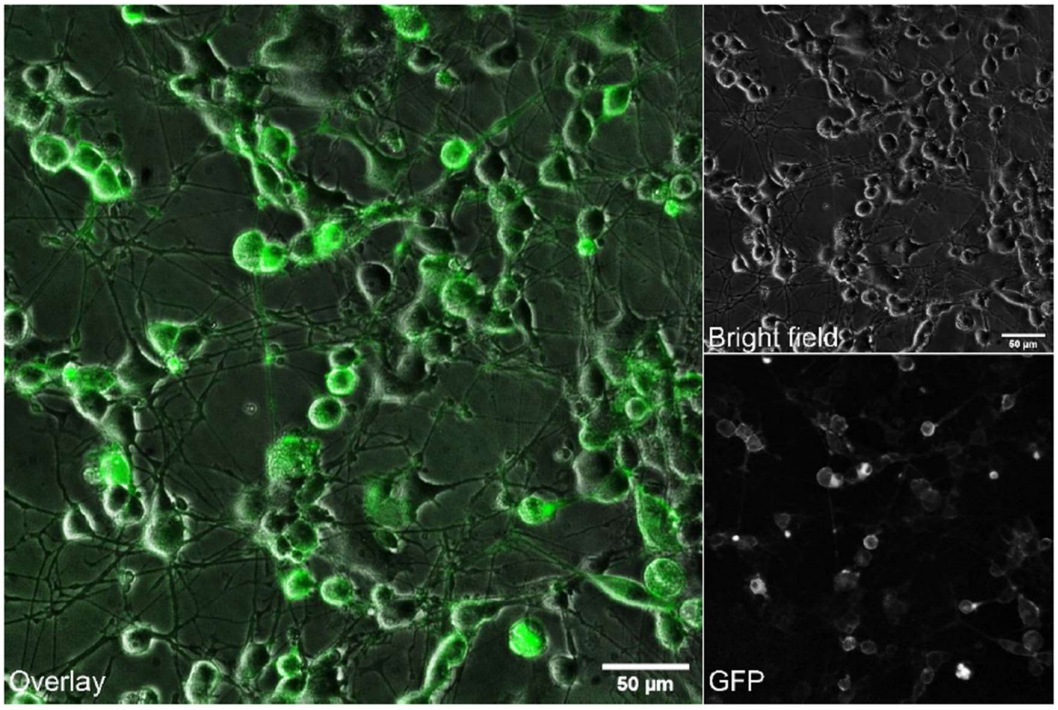

Fig. 22 Transduction of PC 12 Cells with CheRiff

PC 12 cells six days after transduction with CheRiff and five days in differentiation media. The transmitted light image is shown in grey and the GFP signal in green. The GFP signal represents the CheRiff expression. The GFP expression indicates a transduction efficiency of the virus of 80 %. Scale bar indicates 50 µm.

In the next step, the communication between transduced and non-transduced PC 12 cells should be carried out via calcium imaging with Cal-630 AM to capture changes of intracellular Ca^{2+} upon an action potential or activation of CheRiff. Cal-630 AM is a red-shifted (excitation maximum 608 nm; emission maximum 625 nm) chemical calcium dye with an AM ester, similar to Fluo-4 AM. PC 12 cells were transduced with virus-containing *CheRiff*. After six days of transduction and five days in differentiation media, the cells were treated with 4 µM all-*trans* retinal and then stained with Cal-630 AM. For imaging, the cells were incubated in Tyrode's solution for one hour. The CheRiff should be activated by a 488 nm laser with 10 ms laser pulses every 5 s. Unfortunately, the staining of PC 12 cells worked poorly. Rather the plasma membrane than the cytoplasm seemed to be dyed (**Fig. 23 (a)**). Longer incubation time and a higher concentration of the dye did not improve the quality of the images. The cells transduced with Cheriff were stimulated with blue light while simultaneously the calcium signal was recorded. The resulting measurements showed no activation of PC 12 cells after stimulation, only a bleaching effect is noticeable. The change of fluorescence (ΔF/F0), the

bleaching though, seems stronger in some cells (ROI 1 and ROI 2) than in other cells (ROI 3 and ROI 4). But the stronger bleached regions (ROI 1 and ROI 2) had a generally brighter fluorescent signal than the regions that bleached less (ROI 3 and ROI 4) and the normalization was always done. In the next step, it should be carried out if a higher calcium concentration would lead to the desired effects. After transduction, differentiation, and staining, the PC 12 cells were incubated in HBSS with 10 mM Ca^{2+} for one hour. Cells were stimulated with blue light while simultaneously the change in fluorescence was recorded (**Fig. 23 (b)**). This time, the staining worked well and cells show a clearer Ca^{2+} signal. Again, no activation of PC 12 cells is observable, just a slight bleaching effect as seen in the trial with Tyrode's solution.

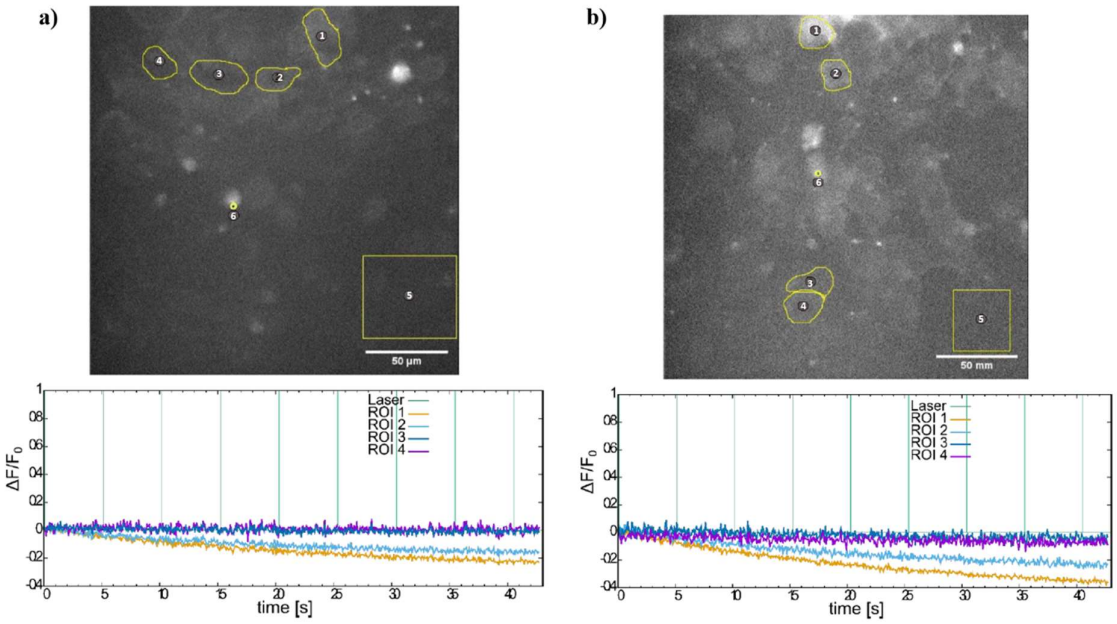

Fig. 23 Calcium Imaging of PC 12 Cells after Laser Stimulation in Tyrode's Solution

Calcium signal of PC 12 – CheRiff cells in Tyrode's solution (a) and HBSS (b) with the analyzed ROIs. ROI 5 displays background for analysis and ROI 6 indicates the position of the laser spot. The associated graph shows the change of fluorescence (ΔF/F0) in ROI 1-4 over the time. In both cases, no responses to light stimuli are observed. The laser pulse (every 5 s) is represented in green lines. Scale bar indicates 50 µm.

Since the stimulation of PC 12 cells did not work out another cell line, namely HEK Na_v 1.3 K_{IR} 2.1 was used at this point. These cells have been transformed with voltage-gated Na^+ and K^+ channels. Through the additional Na^+ and K^+ channels the HEK Na_v 1.3 K_{IR} 2.1 cells

produce at an 80 - 95 % confluency a functional syncytium with the ability for repetitive action potentials[153]. The cells were transduced with *CheRiff* as described before for the PC 12 cells. Before staining with Cal-630 AM, the cells were treated with all-*trans* retinal. The imaging was performed in Tyrode's solution (**Fig. 24 (a)**) and HBSS with 10 mM Ca^{2+} (**Fig. 24 (b)**) to compare stimulation with different extracellular Ca^{2+} concentrations. In the case of measurements in Tyrode's solution, some cells (ROI 1, 2, and 3) show a clear response with increasing fluorescence to the laser stimulus. This signal was reliable for every measured cell over the whole measurement period. Some cells (ROI 4, 5, and 6) showed no calcium oscillations and rather bleaching. When incubated in HBSS with 10 mM Ca^{2+} before imaging, the cells showed brighter calcium signals. Additionally, more cells in total seem to respond to the laser stimulation compared to measurements in Tyrode's solution. The cells were reliably trigger able over the whole time period of measurement (ROI 1 – 5) with a signal intensity compared to those measured in Tyrode's solution. Some cells measured did not show calcium signals (ROI 6, 7, and 8) respectively.

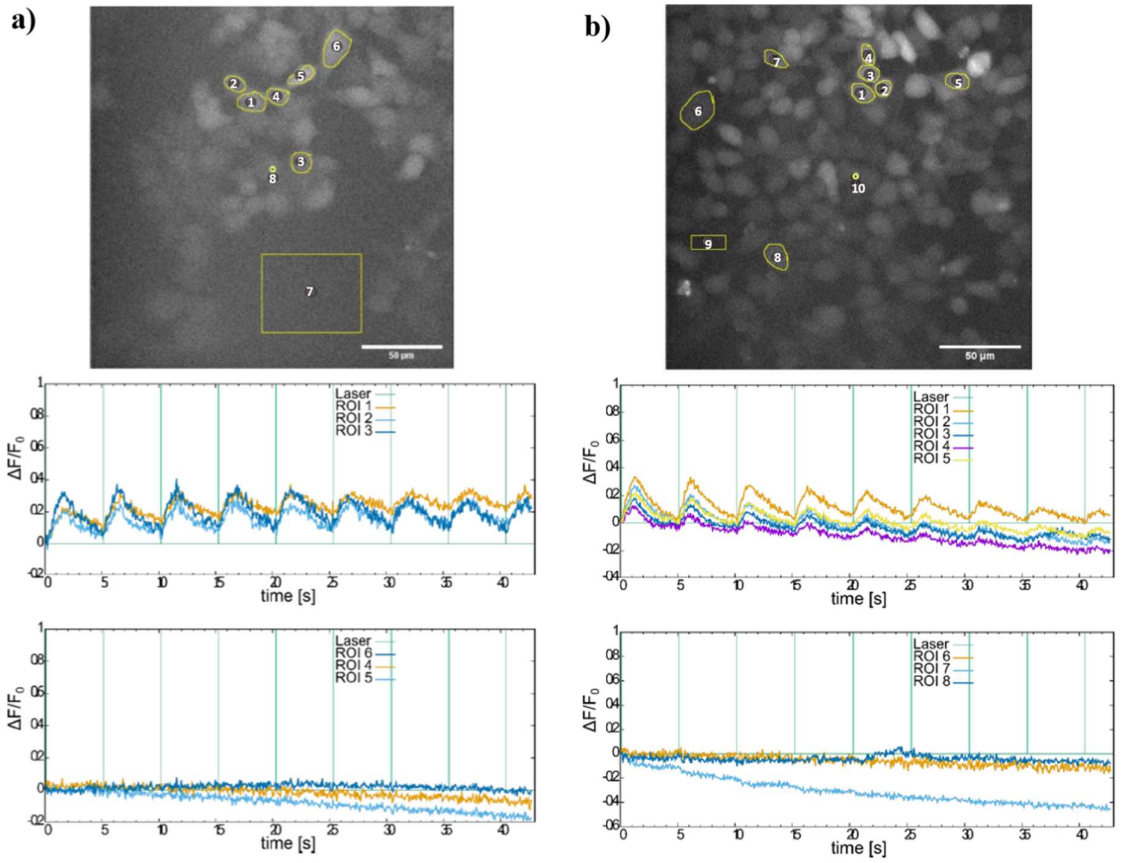

Fig. 24 HEK Na_v 1.3 K_{IR} 2.1 – CheRiff Cells in Tyrode's Solution and HBSS

Calcium signals of HEK Na_v 1.3 K_{IR} 2.1 – CheRiff in Tyrode's solution (a) with the analyzed ROIs. ROI 7 was the chosen background and ROI 8 is the point where the laser pulse hits the cells. The graphs plots the change in fluorescence (ΔF/F0) of stimulated cells (ROI 1 – 3) and not stimulated cells (ROI 4 – 6) over the time. Stimulated cells (ROI 1 – 3) show calcium signals according to applied light pulses, whereas cells of ROI 4 – 6 show no influence of stimulation. For cells incubated with HBSS 10 mM Ca^{2+} (b), ROI 9 is the background used for analysis, and ROI 10 represents the laser spot. The first graph plots the change of fluorescence (ΔF/F0) of stimulated cells (ROI 1 – 5) and not stimulated cells (ROI 6 - 8) over the time. ROI 1 – 5 are showing calcium responses in dependence of light stimuli, whereas ROI 6 – 8 shows no calcium oscillations. The laser pulse (every 5 s) is represented in green lines. Scale bar indicates 50 µm.

To examine if the laser has an influence on the cells by itself, negative controls without the opsin CheRiff were performed (**Fig. 25**). Cells were treated like described above, but without transduction of the opsin to the cells respectively. The staining in combination with HBSS 10 mM Ca^{2+} resulted in an overall brighter fluorescence signal than in comparison to stained cells in Tyrode's solution. Laser stimulation did not evoke calcium responses in cells incubated with either Tyrode's solution or HBSS. Just a steady photo bleaching is observable in both experiments. During measurement in HBSS, one cell show a spontaneous very bright and long-lasting increase in fluorescence (**Fig. 25 (b)** ROI 1).

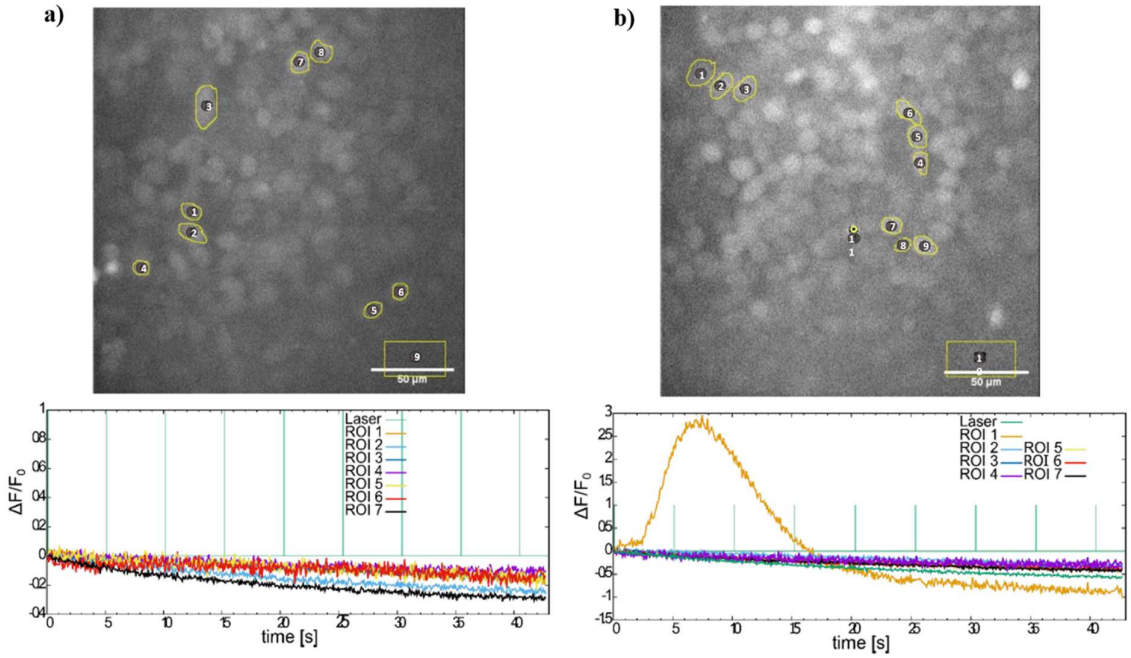

Fig. 25 Negative Control of HEK Na_v 1.3 K_{IR} 2.1 Cells without CheRiff in Tyrode's Solution and HBSS

Calcium signals of HEK Na_v 1.3 K_{IR} 2.1 without CheRiff in Tyrode's solution (a) and HBSS 10 mM Ca^{2+} (b). The graphs plots the change in fluorescence (ΔF/F0) against a chosen background ROI 9 in (a) and ROI 10 in (b). No stimulation effect of the light is noted. The laser pulse (every 5 s) is represented in green lines. Scale bar indicates 50 µm.

Additionally, the influence of all-*trans* retinal on the stimulation should be carried out. HEK Na_v 1.3 K_{IR} 2.1 cells were treated like described before, but no all-*trans* retinal was added. For imaging purposes, cells were incubated one hour in HBSS 10 mM Ca^{2+} before stimulation. The resulting measurements are depicted in **Fig. 26**. Surprisingly, some cells showed a slight response to laser stimuli (ROI 1, 2, and 3). Those were not as robust and strong compared to measurements with added all-*trans* retinal.

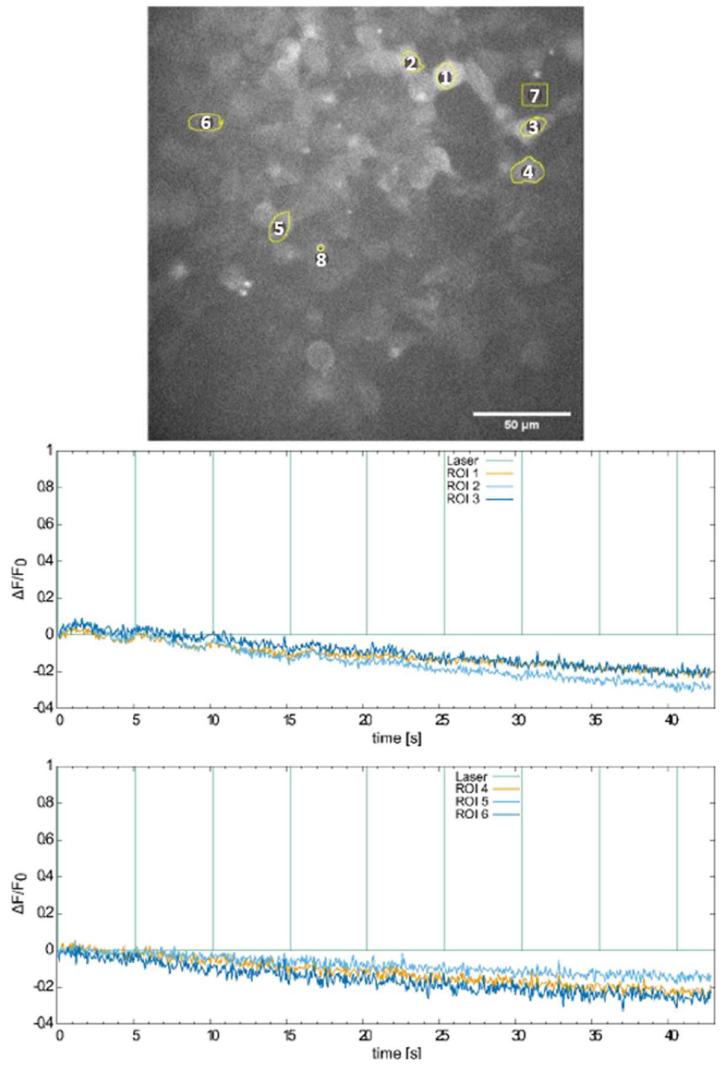

Fig. 26 Negative Control of HEK Na_v 1.3 K_{IR} 2.1 Cells in HBSS without All-*trans* Retinal

Calcium signals of HEK Na_v 1.3 K_{IR} 2.1 – CheRiff cells in HBSS 10 mM Ca^{2+} without the addition of retinal. The graphs show the change in fluorescence (ΔF/F0) against a chosen background ROI 7. ROI 1 – 3 shows low calcium responses to light stimuli over 25 s. After that, no clear signal is detectable anymore. ROI 4 – 6 shows no calcium oscillations. The laser pulse (ROI 8) hits every 5 s and is represented in green lines.

6.3 Application of a Stimulus-Response System to Neuronal Cell Populations

The goal of the previous chapter was to establish an all-optical optogenetic approach with the blue-shifted opsin CheRiff in combination with the red calcium dye Cal-630 AM into neuronal-like cell lines, more specifically PC 12 and HEK Na_v 1.3 K_{IR} 2.1 cells. First calcium imaging measurements showed the feasibility of this approach (refer to 6.2). The next step would be the translation of this method to primary neurons. Rat cortical neurons were isolated from postnatal Spraque-Dawley rats (P2 - P5) of both sexes as previously described (refer to 5.1.1). The

isolated cells were maintained in culture for a total amount of seven days to allow for network formation and subsequently prepared for immunostaining. The neurons were stained with β-III-tubulin and synaptophysin, two commonly used neuronal markers to verify the successful isolation process. β-III-tubulin plays a critical role in proper axon guidance and maintenance, synaptophysin, on the other hand, is involved in the regulation of synaptic plasticity and targeting vesicles to the plasma membrane. **Fig. 27** shows the immunostained neurons.

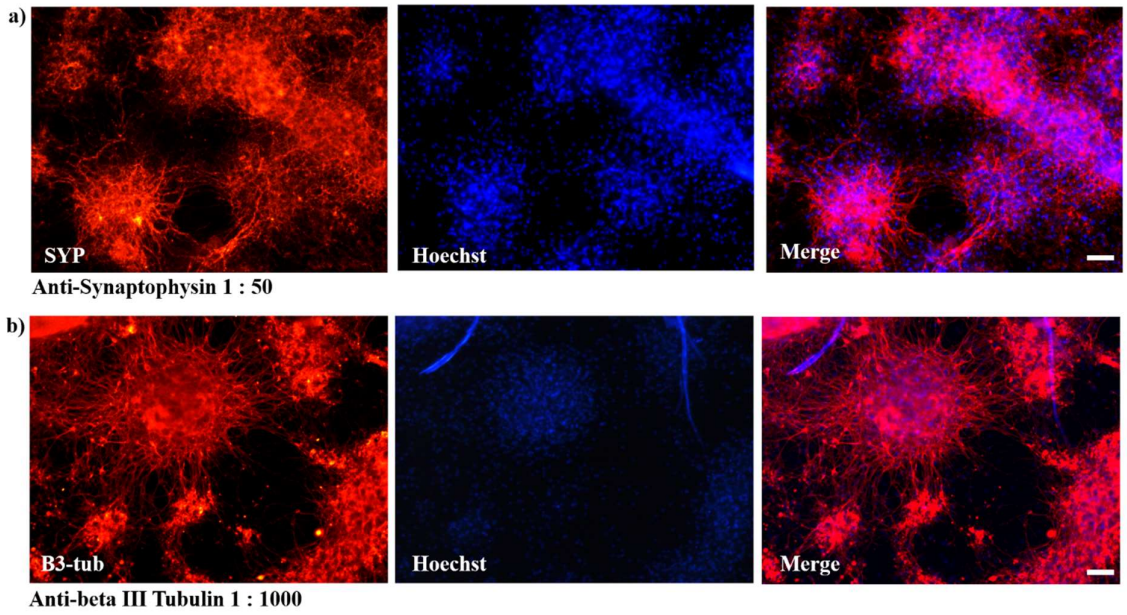

Fig. 27 Immunostaining of Primary Cortical Neurons

Isolated cortical neurons from rat pups postnatal D 3. Neurons were incubated seven days in vitro and stained with antibodies against synaptophysin (a) and β-III-tubulin (b). The nuclei of all cells were stained with Hoechst (blue). Scale bar indicates 100 µm.

Further, it should be determined how many excitatory neurons are present in one isolation. Excitatory neurons can be depolarized by the influence of CheRiff and thus generate action potentials. Fresh isolated hippocampal neurons were stained with antibodies against β-III-tubulin and Ca^{2+}/calmodulin-dependent protein kinase II (CaMKII). CaMKII is an essential player in the N-methyl-D-aspartate receptor-mediated increase in conductance at glutamatergic synapses, therefore it is a suitable marker to identify excitatory neurons. Several pictures of the immunostained neurons were taken, one representable example is found in **Fig. 28**. The total cell number (Hoechst stained) was counted and put into the relation of β-III-tubulin and CamKII positive cells. Five images were counted and resulted in an average of 10.7 % β-III-tubulin positive cells. Only 6.2 % of the entire cells were double positive for beta-III-tubulin and

CamKII. This means that only about 10.7 % of the isolated cells were neurons and only 6.2 % were excitatory neurons.

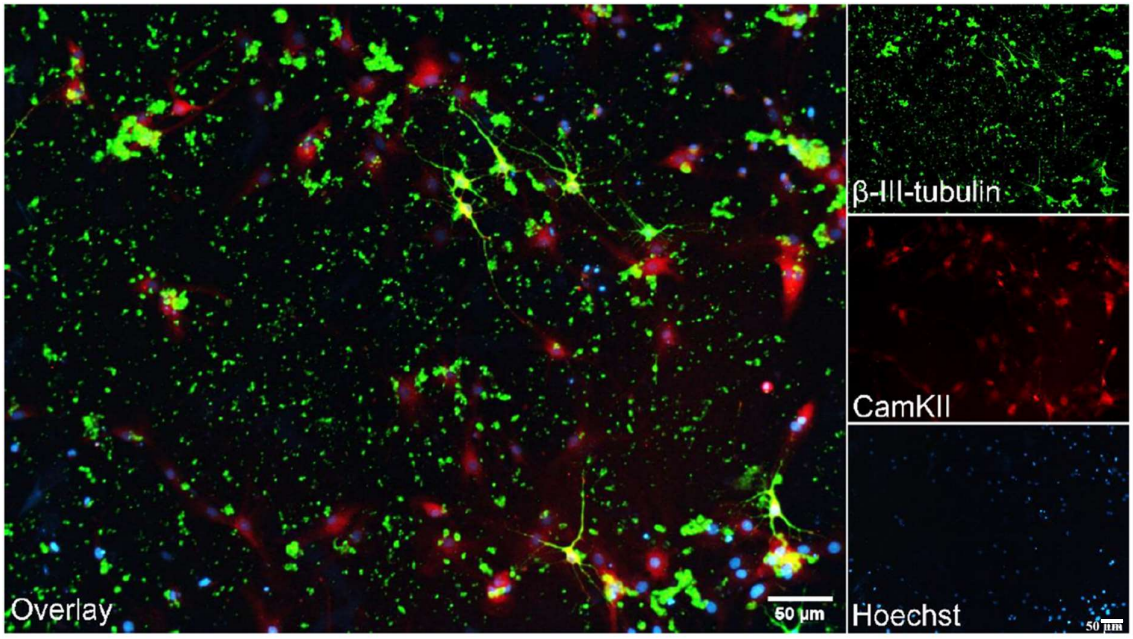

Fig. 28 Immunostaining of Excitatory Neurons

Isolated hippocampal neurons were kept for seven days in culture and subsequently stained with antibodies against β-III-tubulin (green) and CamKII (red). The nuclei of all cells were stained with Hoechst (blue). In the overlay image cells that are positive for CamKII and β-III-tubulin appear yellow. Scale bar indicates 50 µm.

To allow for both, optical recording with imaging and simultaneous electrical recording, a Multi-Electrode Array (MEA) should next be combined with calcium imaging of the isolated hippocampal neurons. This way, the induced calcium oscillations by optogenetic stimulation should be correlated to action potentials. Fresh isolated hippocampal neurons were seeded on PDL-coated MEA chips with 60 electrodes in total (**Fig. 29**). On DIV 1 lentiviral transduction of hippocampal populations was performed to deliver FCK-CheRiff-eGFP to the neurons. The promoter was chosen for transgene expression to obtain preferential gene expression in excitatory neuronal populations. The measurement took place after network formation 12 - 14 days *in vitro*. The neurons were transferred to an imaging set-up consisting of an inverse Leica microscope and a fiber-coupled LED for stimulation. Unfortunately, no action potentials of the neurons were recorded during several measurements. Only light-induced artifacts generated by photovoltaic were visible and interfered with the recordings (data not shown).

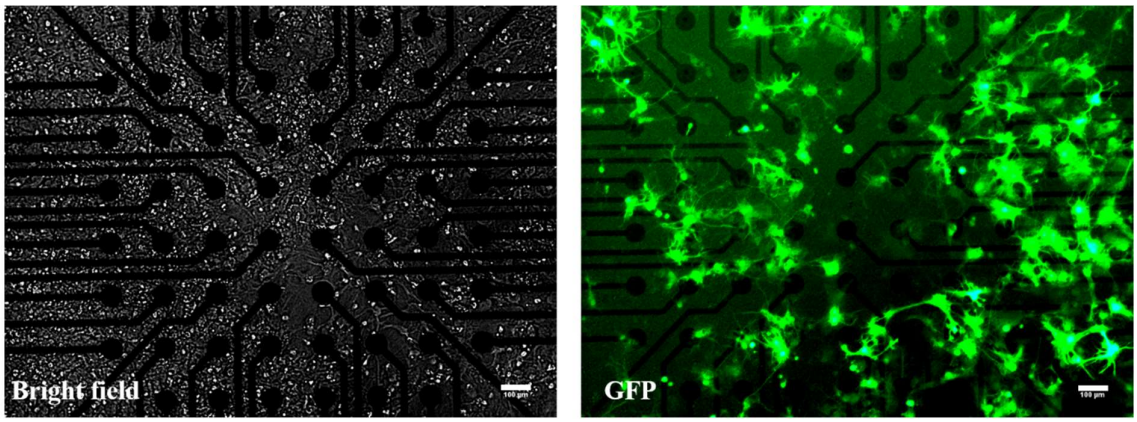

Fig. 29 CheRiff Hippocampal Neurons on a Multi-Electrode Array

Left: A bright-field image of hippocampal neurons cultured on Multi-electrode arrays. The neurons formed a maturated network all over the growth area including the electrodes (appear as black dots). Right: Fluorescence images of positive transduced neurons with *CheRiff-GFP*. Scale bar indicates 100 µm.

This thesis aim to establish an optogenetic test system to probe inter-neuronal communication of different functional units, for example, the brain (hippocampal and cortical neurons) and the cochlea (spiral ganglion neurons). By using a combination of the blue-shifted channelrhodopsin variant CheRiff and the genetically encoded calcium indicator with red-shifted excitation and emission spectra, namely jRCaMP1a, all tools to stimulate and image spectrally independent separated populations of neurons *in vitro* are available. Since the measurements with the calcium dye Cal-630 AM in former experiments with neuronal-like cell lines lead to issues regarding the brightness of staining and evenly distribution of the dye, jRCaMP1a was chosen instead for further experiments. **Fig. 30** depicts an example of the expression of CheRiff and jRCaMP1a in isolated hippocampal neurons.

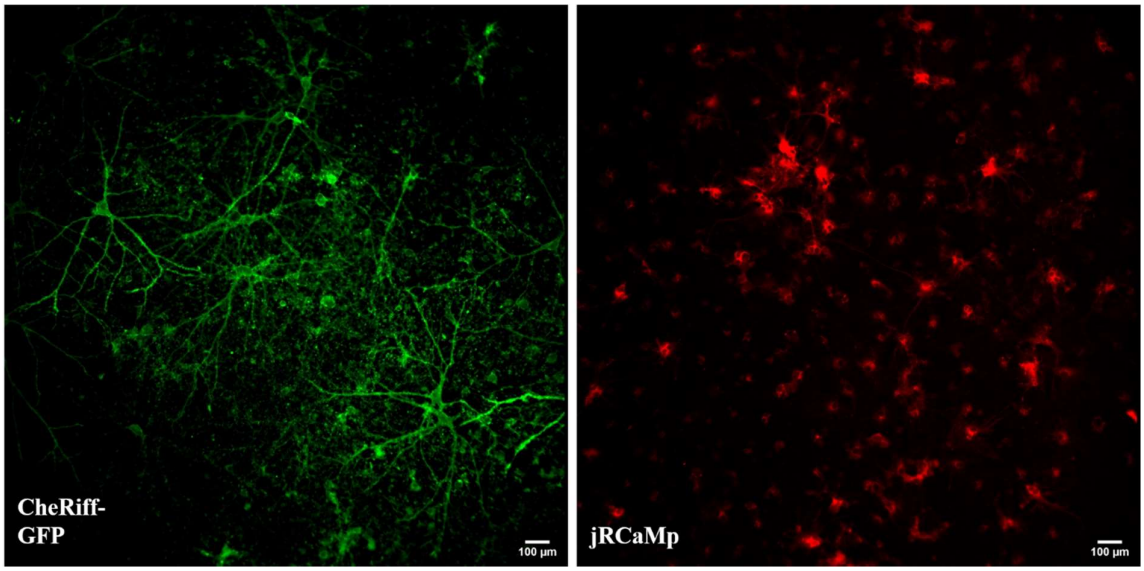

Fig. 30 Expression of CheRiff and jRCaMP in Primary Hippocampal Neurons

Left: Hippocampal neurons after 7 DIV showing GFP expression as well in soma as in neurites of transduced cells. Right: The same neurons showing jRCaMP expression in red. The signal is localized rather somatic, the cell nuclei are visible as black spots. Scale bar indicates 100 µm.

In the next step, a system to study the spread of excitation in inter-neuronal networks should be established. To achieve this, hippocampal, cortical and spiral ganglion neurons were co-cultured. Cortical (CN) and hippocampal neurons (HN) were double transduced with *CheRiff* and *jRCaMP1a*, whereas SGNs were only transduced with *jRCaMP1a* to avoid accidental activation by stimulation light. The optogenetic HNs and CNs should act as a signal transmitter to the SGNs, thus to say as a neuronal-tandem trigger-system. The spatial separation was achieved by using a 3 well silicone insert. **Fig. 31** shows a 3 well silicone chamber with the three neuronal populations. The silicone insert was used for the first two days of incubation, resulting in a gap between neuronal populations of 1 mm after removing the silicone chambers. For a better understanding of the complete process, a schematic drawing from the isolation process until stimulation experiments is shown in **Fig. 15**. A high-resolution bright field and fluorescence image of the CheRiff and jRCaMP1a expression in HNs, CNs, and SGNs is shown in **Fig. 31** respectively. The image was taken on 14 DIV. Only HNs and CNs retain their shape given through the silicone chambers. Although, HNs tend to dissolve their shape on the SGN facing side. The SGNs widely distribute and form partially cell clumps during incubation. The jRCaMP1a expression is very dominant in all types of neurons, even though there is a very limited number of positive SGNs. This is due to the nature of the isolation process. Most of the

cells visible in the middle line (bright field) are glia cells like Schwann cells. The CheRiff expression is more dominant in HNs in comparison to CNs.

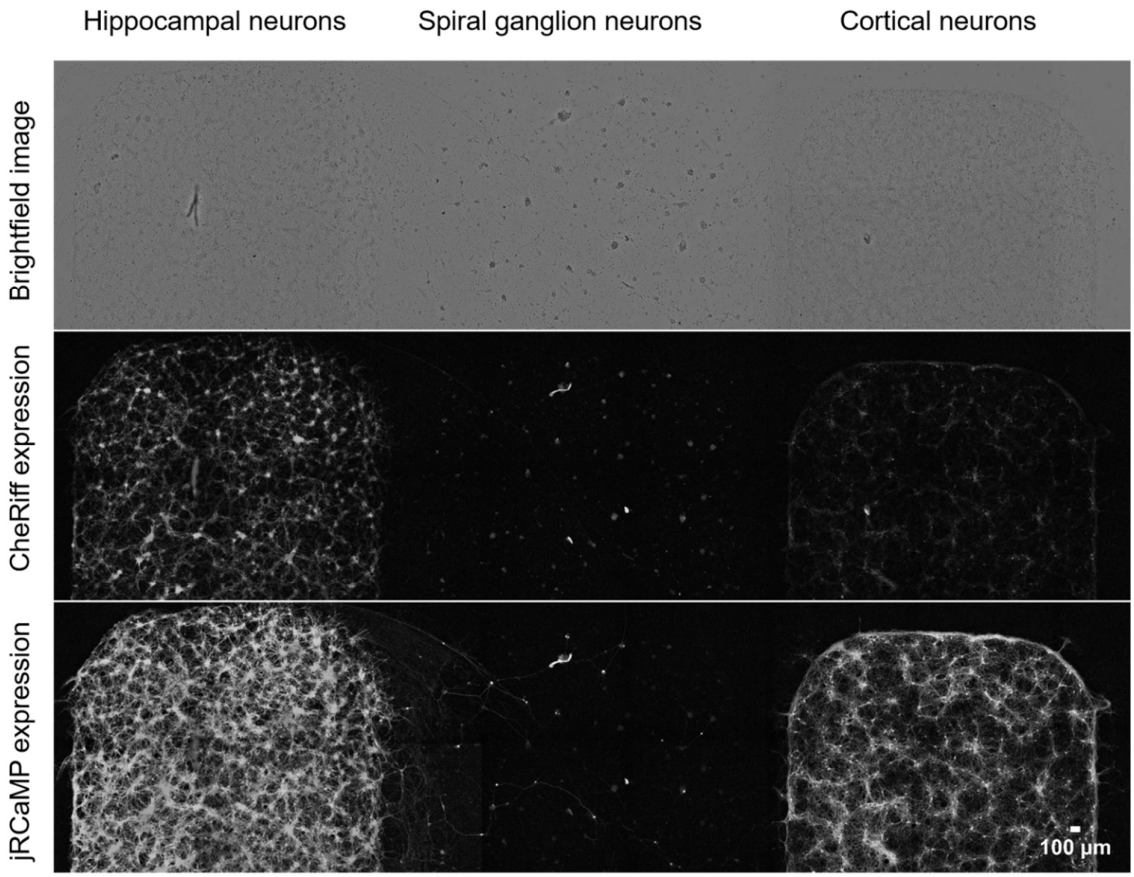

Fig. 31 High-Resolution Bright Field and Fluorescence Image of a Set of Inter-Neuronal Populations

Hippocampal (HN), cortical (CN), and spiral ganglion neurons (SGN) in co-culture after 14 DIV. Images were taken in Tyrode's solution. Top: Bright field image of the three neuronal populations shows network formation between HNs and SGNs as well as for SGNs and CNs. HNs and CNs maintained their patch form resulting from incubation with silicone chambers, whereas SGNs distributed widely. Middle: Fluorescence image of the resulting CheRiff expression. HNs and CNs show GFP expression all over the imaged area. SGNs show auto fluorescent effects due to clump formation while incubating. Bottom: Fluorescence image of jRCaMP1a expression. HNs and CNs show strong jRCaMP1a signals. Only a few scattered SGNs show jRCaMP1a expression. SGNs are recognizable by their comparatively long neurites. Scale bar indicates 100 µm. (Heeger et al. 2021)

The co-cultured neurons were transferred to an imaging setup after 12- 14 DIV, consisting of an inverse Leica microscope equipped with a scientific CMOS camera, a high power LED for fluorescence imaging and a fiber-coupled LED for stimulation. The manipulation LED was fixed directly above either an HN or a CN population. Three spots per population were stimulated with four different pulse durations (10 ms; 100 ms; 250 ms; 500 ms). **Fig. 32** shows

a typical fluorescence time series of a blue light-activated CNs population (right) triggering a response in a single SGN (left). The link to the corresponding video can be found in the Appendix (**Video S 1**). After a stimulation pulse (blue dotted line), the fluorescence signal in an SGN increase within 0.4 s to its maximum and decreases to its basal level after 5 s respectively.

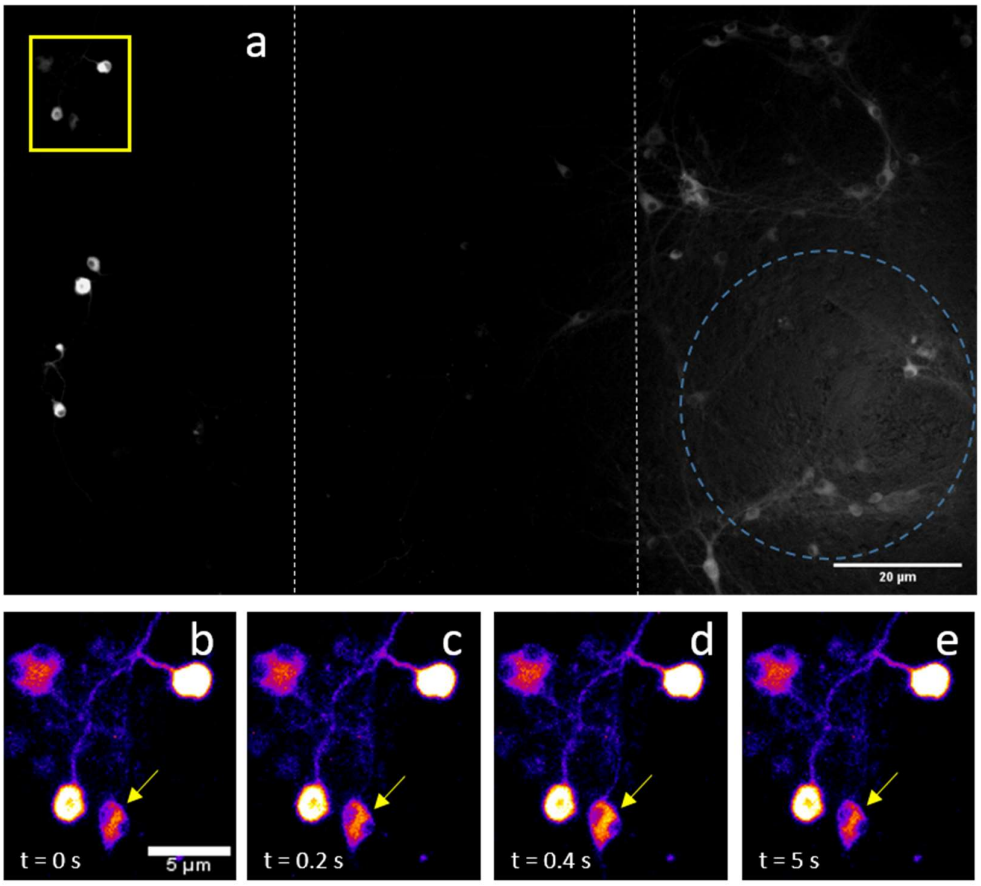

Fig. 32 Fluorescence Series of a Spiral Ganglion Neuron activated by Light triggered Cortex Neurons

(a) A representative fluorescence image showing a population of SGNs (left) transduced with the GECI jRCaMP1a and CN (right) double transduced with CheRiff and jRCaMP1a. Yellow square points out responding SGN. The neurons are separated by a gap of 1 mm due to the properties of the silicone inserts. The blue dotted circle indicates the position of the stimulation LED. (b) – (e) Time series of a responding SGN after blue light stimulation of the CNs with a 250 ms pulse respectively. (b) SGN of interest (yellow arrow) shows the basal level of fluorescence at beginning of stimulation. (b) - (d) Fluorescence signal increases within 0.4 s after the stimulation pulse to its maximum. (e) Five seconds after the stimulation pulse the SGN fluorescence drops down to its basal level again. Scale bar indicates 20 µm. (Heeger et al. 2021)

On each day of measurement, three dishes were processed in the experimental setup as shown in **Fig. 32** with the above-mentioned parameters. In total, five test series were performed (n = 5). An example of the corresponding Matlab graph is shown in **Fig. 33**. Every 5.5 s, a stimulation

pulse of the LED (gray solid line) triggers either HNs (**Fig. 33 (a)**), (blue spikes) or CNs (**Fig. 33 (b)**), (orange spikes). This in turn stimulates connected SGNs (green spikes). Peak maxima were marked with dots to simplify the counting process. Every light pulse in these two examples resulted in a stimulation of the HNs or CNs leading to an immediate response of the SGNs. The SGN peaks which occurred in correlation with the HN or CN peaks of all stimulation series were counted and plotted to get a quantitative statement of the stimulation efficiency. Even with very short stimulation pulses of 10 ms, the stimulation efficiency of the SGNs reached roughly 60 % for both, HNs and CNs. With increasing stimulation pulse length, the stimulation efficiency of both HNs and CNs increased rapidly and reached a plateau at 250 ms. The overall stimulation efficiency of the SGNs triggered by the HNs reached over 90 % with 250 ms and 500 ms pulses respectively, whereas SGNs triggered by CNs show slightly lower efficiency (~80 %) with the same parameters.

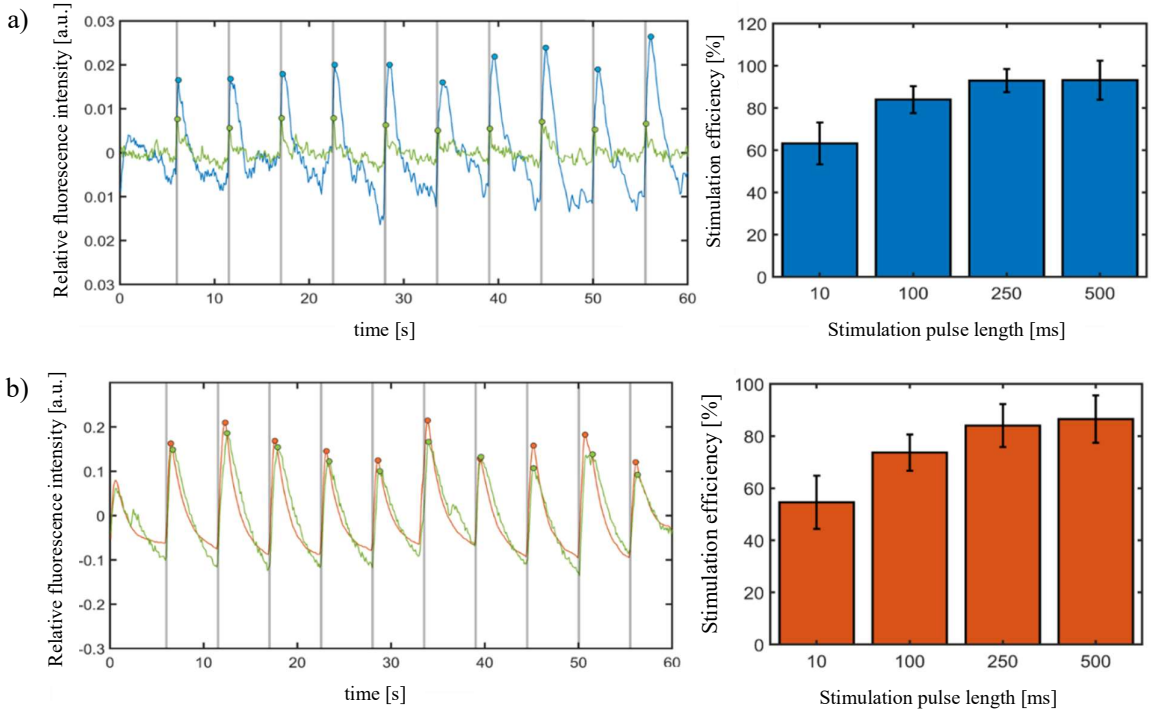

Fig. 33 Calcium Signals of Inter-stimulated SGNs and Stimulation Efficiency dependent on Stimulation Pulse Length

a) Left: One example of calcium signals of LED stimulated hippocampal neurons (HN) (blue peaks) and responding spiral ganglion neurons (SGN) (green peaks). HNs, as well as SGNs signals rise in accordance to the light pulses of the LED (gray lines). Compared to the fluorescence of the HNs, the SGN signal is weaker. Right: The bar chart of compiled peak counts of the entire series of measured SGNs in dependence of the pulse duration. With increasing pulse length, the stimulation efficiency increases. b) Left: One example of calcium signals of LED stimulated cortical neurons (CN) (orange peaks) and responding SGNs (green peaks). CNs, as well as SGNs peaks, rise also in accordance to the light pulses of the LED (gray lines). The fluorescence intensity of SGNs is almost as high as the light-stimulated CNs. Right: The bar chart of compiled peak counts of the entire series of measured SGNs in dependence of the pulse duration. With increasing pulse length, the stimulation efficiency increases.

6.4 Establishment of a Cell Growth System for spatially directed Signal Generation

The first successful measurements show the feasibility of our neuronal-tandem trigger-system, consisting of optogenetic activated HNs and CNs transmitting received light signals forward to adjacent SGNs. The chosen co-culture system by silicone chambers, however, lacks on defined cell outgrowth regions, thus the signal transmission is somewhat undirected and depends on random network formation. To address this problem, a simple structured cell growth system for spatially directed signal generation based on AuCS should be established. To first generate easy and fast patterned AuCS, glass plates were sputter-coated with gold nanoparticles of desired thickness. An in-house 3D printed PLA motive placed on the coverslip leads to the desired cell growth area (**Fig. 34 (a)**). A planetary gear rotates the sample during the sputtering process,

enabling optimal distribution of the gold. The device has been set to a gold layer thickness of 30 nm. After the sputtering process and removal of the PLA motive, a structure in the shape of the mask appears on the gold surface. Furthermore, the gold is evenly distributed throughout the coverslip and forms a continuous layer (**Fig. 34 (b)**). The 3D printing approach enables a rapid and inexpensive manufacturing process with customized designs. However, the thickness of the PLA mask and the resulting angles of incidence during the sputtering process lead to a blurry print.

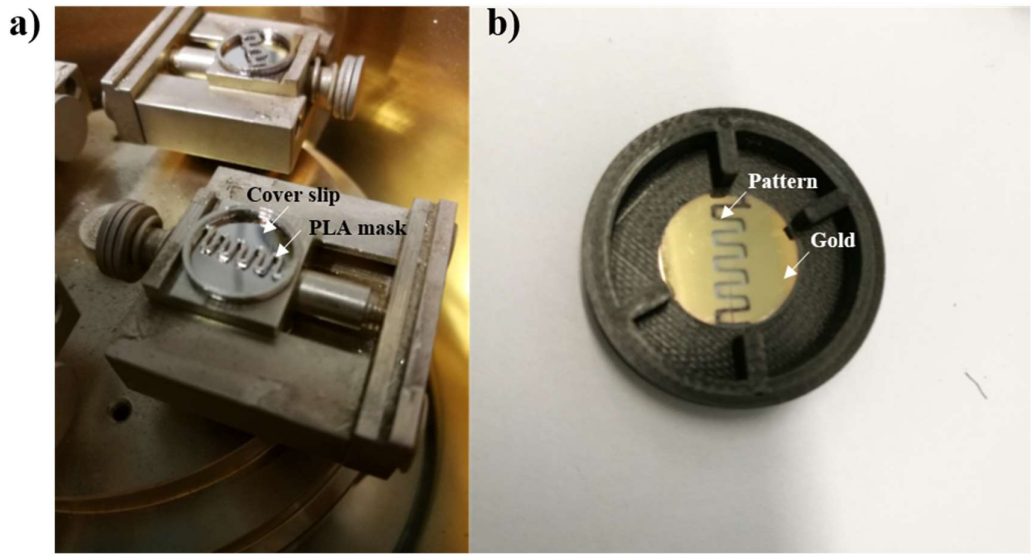

Fig. 34 3D printed PLA Mask can be used to enable structured Gold Monolayers

(a) A cover slip coated with a gold monolayer. The PLA mask prevents the desired area from the gold coating and reveals the desired pattern, in this case, a triangular motive (b).

Because of the blurry contours of the gold monolayer after sputtering with a PLA mask, it should be carried out if laser ablation of the gold film is feasible to ensure structures that are more precise and finer feature size that cannot be reached with a PLA mask. Gold nanoparticles have absorption peaks at 520 – 530 nm[154] thus, a thin layer of 30 nm should have similar physical characteristics in terms of absorption. To validate this assumption, spectral analysis with different layer thicknesses of gold layers was performed (**Fig. 35 (b)**). Indeed, the resulting maximal absorption lies between 510 nm for a thickness of 50 nm and 533 nm for 10 nm thickness. For the laser ablation part, it was decided to use a homebuilt laser setup called GNOME (Gold Nano Particle Mediated Laser Transfection). It uses a pulsed picosecond laser with a wavelength of 532 nm and maximum output power of about 80 mW. The pulsed laser

enables ablation of the gold film through precise heating and resulting evaporation. Three different layers in thickness of gold (10, 20, and 30 nm) with five different settings in laser power (10 – 50 mW) and a scanning speed of 5 mm/s were tested. **Fig. 35 (a)** shows the resulting ablated areas on the gold films. With increasing laser power, the ablated area gets broader and the edges become sharper in all cases. To verify this, the resulting line width of each layer thickness (n = 3) was measured and the mean value of the measurement results plotted as a function of the laser power (**Fig. 35 (c)**). The graph shows clearly the tendency of broader cutting width with increasing laser power. However, the effect and thus the resulting lines decrease with an increasing layer thickness of the gold. In addition, the 50 nm gold layer absorbs much more light, resulting in black appearing non-ablated areas. Based on these results, for further optical experiments, 30 nm thickness of gold and 50 mW laser power were used.

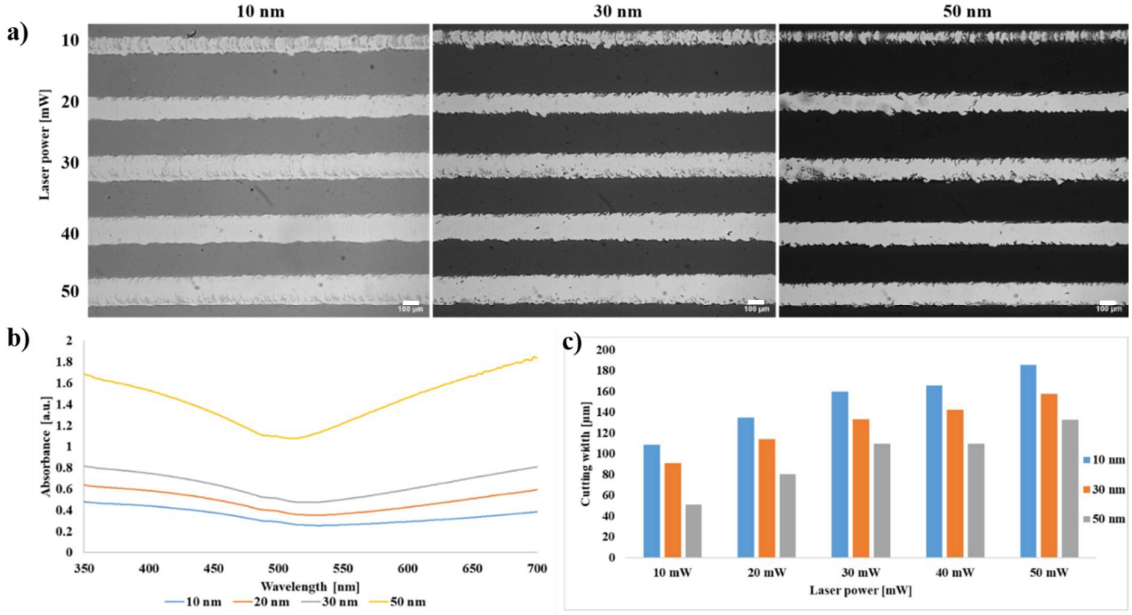

Fig. 35 Laser Irradiation as an Alternative to structure Gold Monolayers

(a) Microscopic visualization of gold monolayers after laser manipulation. The thickness of the gold layer varies from 10 to 30 nm (left to right) and the laser power from 10 to 50 mW (top to bottom). With increasing laser power, the cutting width gets broader and sharper. (b) The spectrum of gold monolayers with varying thicknesses (10 – 50 nm). Points of maximal absorption are in the expected range of 510 – 530 nm. An absorption shift due to the thickness of the gold layer is observable. (c) Dependency of efficiency of structured gold monolayer thickness and laser power. In general, with increasing laser power, broader cutting width is to see. But with increasing gold layer thickness, this effect diminishes. Scale bar indicates 100 µm.

In the next series of experiments, it should be carried out if it is possible to let the cells selectively grow in the laser-ablated structures. For this purpose, the laser-ablated gold slips are

further incubated with mPEG, a polymer conjugated with a thiol group, ensuring a covalent bond between the gold and the polymer. This way, a hydrophobic and thus cell repellent surface is generated on the gold film. The cells seeded out on the gold slips are only able to bind on the gold-free structures. To test the long-term stability of our system, we used three different mPEG sizes (1000 Da; 6000 Da; 30.000 Da) with increasing concentrations of mPEG (0.01 µM – 5 µM) plus water control, where no mPEG is added. The cells were incubated for a total amount of 72 h. On the day of imaging, cells were loaded with Calcein-AM to check the viability and increase the visibility. **Fig. 36** shows the resulting fluorescence images. In all cases, the H_2O control shows unspecific cell attachment over the whole image section. With increasing mPEG concentration, the number of cells attaching to the gold decreases until finally at 5 µM no more cells stick unspecific to the gold and instead are growing on the laser-ablated region. All used sizes of mPEG work evenly well as no differences in cell attachment are detectable. It is thus to see, with increasing mPEG concentration, the density of the cells within the laser-ablated areas also increasing, recognizable by the higher confluency. Finally, at a concentration of 5 µM the cells are fully packed and probably fused to a syncytium.

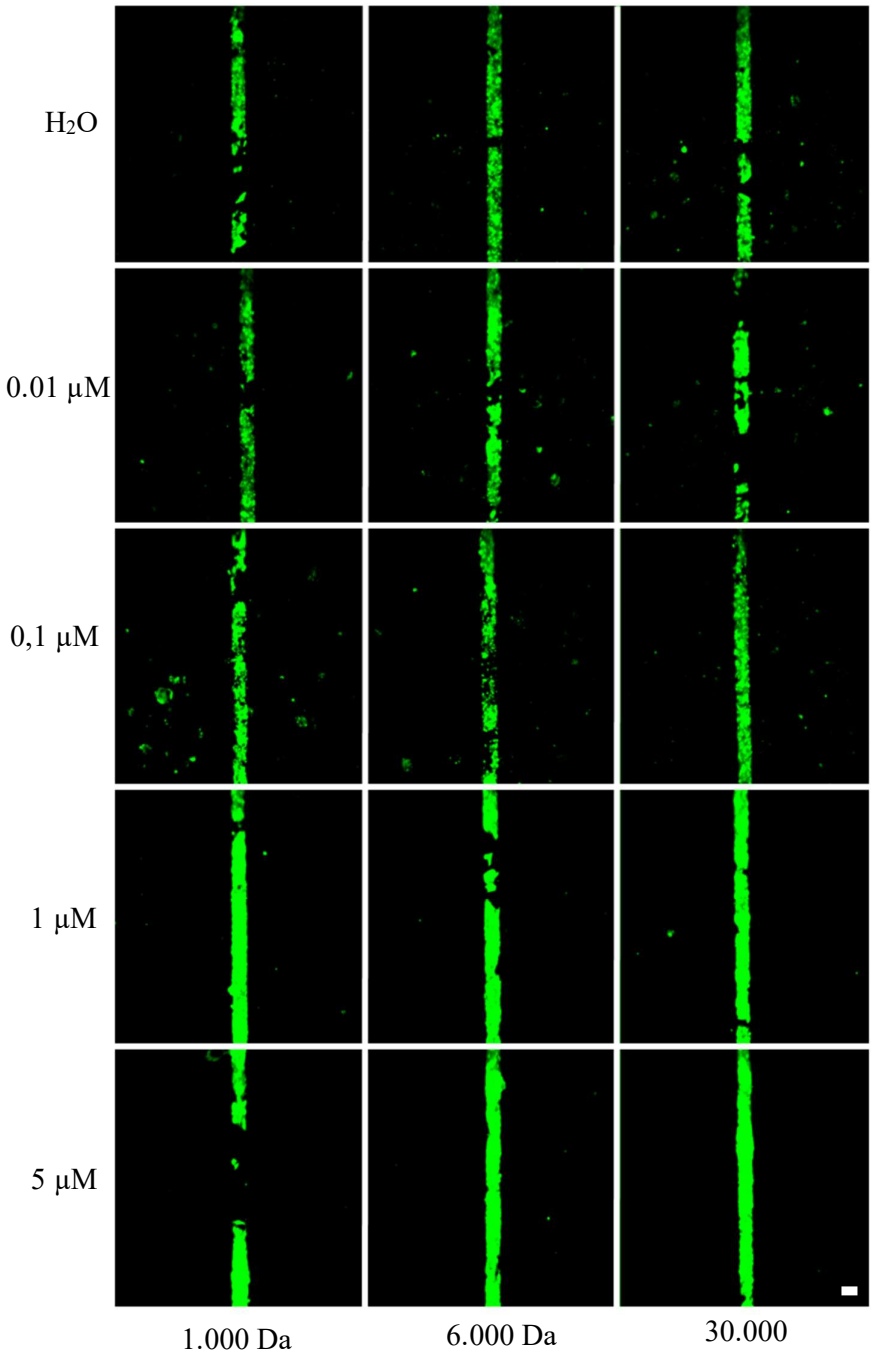

Fig. 36 Gold Nano Layers combined with mPEG enables selective Cell Growth with long-term Stability

Montage of fluorescence images of HL-1 cells incubated for 72 h on laser-ablated gold surface. Cells are dyed with Calcein AM, three different mPEG sizes (1.000 Da; 6.000 Da; 30.000 Da) with increasing concentration (0.01 µM – 5 µM top to bottom) were tested. From a concentration of 1 µM of mPEG, unspecific cell attachment on the gold surface is largely prevented. The size of the mPEG seems to play no role. Scale bar indicates 100 µm.

Results

To further validate the feasibility of our method we designed a more complex pattern and combined the selective cell growth approach with calcium imaging and optogenetics to probe the formation of electrical conduction between the excitable cells. HL-1 cells were used for establishment experiments since they are able to form a functional syncytium with the ability to transmit excitation from cell to cell, resulting in propagation of the excitation waves[155], making it the ideal candidate for preliminary calcium signal propagation experiments. The excitation waves were observed and recorded by staining with Cal-630 AM. To be able to stimulate HL-1 cells by light, the cells were already stably transduced with ChR2 carrying the H134R mutation, making it more feasible for electrophysiological measurements because of its higher current amplitudes[32]. In addition, the ChR2 is equipped with the ubiquitously active promoter elongation factor 1α (EF1α) driving expression of ChR2 infusion with EYFP. In a confluent cell layer, the excitation waves and their propagation after LED-stimulation was observed (**Fig. 37**). The stimulation took place via a fiber-coupled LED (white dotted circle) as used for the neuronal-tandem experiments (5.5.1). After a short stimulation pulse of 100 ms on the bottom side of the structure (t = 0 s) a propagating calcium signal from the bottom (t = 0.1 s) is expanding to the top of the structure (t = 0.2 s) and finally illuminates the whole structure (t = 0.3 s). After 5 s the cells fluorescence drops down to its basal level again. This effect was repeatable during the whole measurement process.

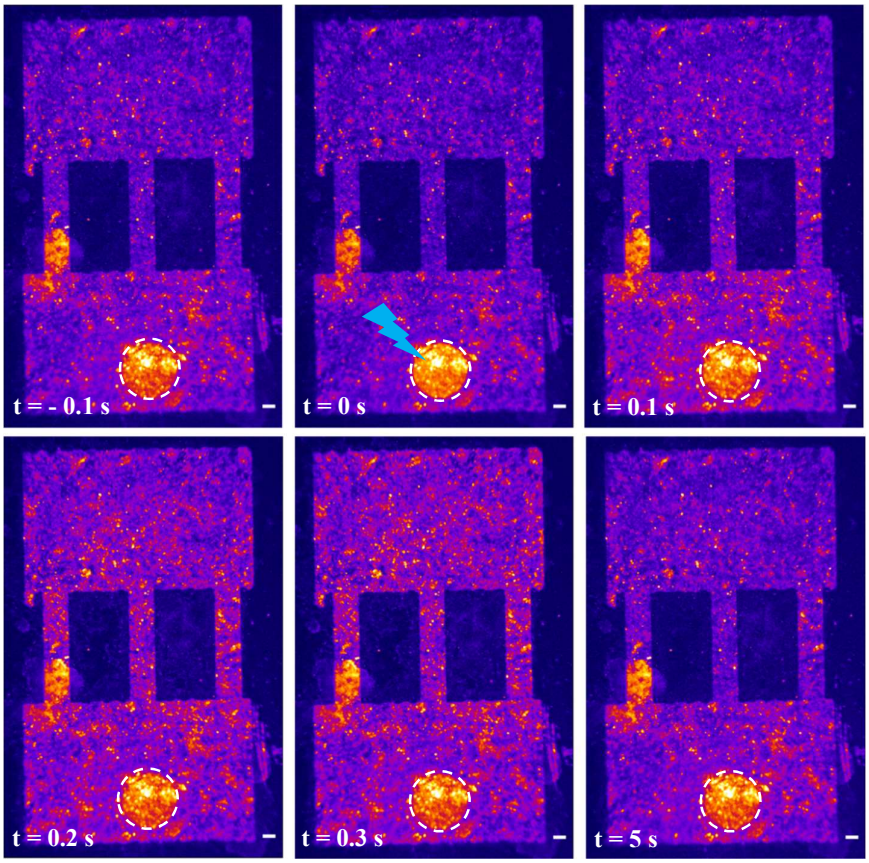

Fig. 37 Calcium Oscillations after Optogenetic Stimulation of HL-1 Cells

Time series of HL-1 cells and a propagating calcium wave on gold patterned glass cover slips after stimulation with blue light. The glass cover slips were gold sputtered and laser-treated to obtain the desired pattern (refer to 5.6). ChR2-HL-1 cells were seeded on the gold structures and kept at 37 °C for 72 h to ensure confluency and syncytium-formation. Then the cells were dyed with Cal-630 AM and imaging took place in HBSS + 10 mM Ca^{2+}. After blue light (blue flash) stimulation (t = 0) a calcium wave is expanding from bottom to top of the laser-generated structure. After 5 s of the stimulation pulse the fluorescence drops down to its basal level again. Scale bar indicates 100 µm.

7 Discussion and Outlook

This thesis addresses the hypothesis, if neurons of different origin are capable of forming functional connections and if so, whether this can be combined with directed cell growth to establish a neuronal-tandem trigger-system. The use of an optogenetic trigger-response system allowed verifying communication between spiral ganglion neurons and hippocampal, as well as cortical neurons. The results serve for an exploitation in the development of biohybrid systems used for treatment of hearing loss. In the following section, key aspects of the obtained results during this thesis are discussed and possible future clinical applications in the deafened cochlea are indicated.

To establish the neuronal-tandem trigger-system the following work packages were processed:

Establishment of an Optogenetic Stimulus-Response System

As a first step, a stimulus-response system consisting of an optogenetic actuator and a calcium-imaging sensor, namely CheRiff and jRCaMP1a, needed to be established. For first verification, patch-clamp measurements of optogenetic N2a cells showed successful light-driven stimulation. Optogenetic stimulation in cell lines like N2a, but also other cell lines is well described in the literature and has already been shown by many working groups[156,157,158]. Based on the positive patch-clamp results with N2a cells, the stimulation experiments were further performed with primary neurons. To yield more information about network dynamics optogenetic stimulation experiments were performed with an MEA device. The data obtained from cell experiments presented large interfering signals from other devices and, although the transduction efficiency should be sufficient for successful stimulation, no action potentials were recorded. Due to the usage of a relatively large LED fiber, the illuminated area was quite big (0.63 mm^2). Due to this, direct illumination of electrodes could not be prevented. That, and the relatively high illumination intensity of 0.25 mW/mm^2 lead to measuring artifacts, evoked by a photo electrochemical effect, called the Becquerel effect. Light artifacts in neural signal recordings are still a major issue in optogenetics with MEA[159,160,161]. Taken together, fiber-based stimulation of optogenetic neuronal populations with electrophysiological measurements like patch-clamping and MEA are challenging and not suitable for the research question of this thesis. Calcium imaging on the other hand is a well-established method for qualitative measurements of neuronal populations[162,163] as well as in combination with optogenetics[164,95]. Thus, a stimulus-response system consisting of an optogenetic actuator CheRiff[79] and the calcium sensor Cal-630 AM was established next in PC 12 cells[165]. Transduction of HEK but also PC 12 cells with CheRiff showed a strong GFP-signal (~ 50 % in HEK; ~ 80 % in PC 12)

in both cell lines. The GFP-signal was more profound at the membrane of the cells, indicating correct transportation of the CheRiff to the membrane (**Fig. 21** and **Fig. 22**). Unfortunately, stimulation experiments by light did not result in observable calcium signals in the PC 12 cells (**Fig. 23**). Notably, PC 12 cells are quite sensitive and can generally detach quite easily if handled rigorously. Addition of the all-*trans* retinal to the media for example lead to retraction of neurites and partial detachment of cells, indicating metabolic stress and thus unsuitable conditions to perform optogenetic experiments. Due to these negative results and the relatively time-consuming transduction and subsequent differentiation process of PC 12 cells, stimulation experiments were continued with HEK Na_v 1.3 K_{IR} 2.1 cells. The function and activation of CheRiff could lastly be demonstrated by calcium imaging in HEK Na_v 1.3 K_{IR} 2.1 cells (**Fig. 24**). Some of the analyzed cells showed an answer to the stimulation with the laser. However, most cells showed only bleaching of Cal-630 AM and no change of cytosolic Ca^{2+} concentration. Since an activation of CheRiff is evident in cells not treated with all-*trans* retinal (**Fig. 26**) and the used media has no retinal derivate that the cells can use directly, it is possible that they synthesize a retinal-like derivate from the existing vitamins and amino acids. However, incubation with all-*trans* retinal helped to increase Ca^{2+} signal acquisition. CheRiff activation was observed more frequently in the images at increased calcium concentration than in Tyrode's solution. This is probably because the threshold for calcium release by RyR was reached more often and thus resulted in higher activation. However, the fact that the recorded cells showed no time delay between calcium peaks, leads to the assumption that cells were probably stimulated by the reflection of the light in the medium rather due to propagating signals. This hypothesis is supported by the fact that CheRiff requires comparatively low light intensities to be activated[79,145] and that many cells showed no calcium oscillations, no matter if they were near or further away from the stimulated cell. The used calcium dye Cal-630 AM was also very unevenly distributed within the cells and the fact that the cells needs to be discarded after one measurement, makes it unhandy to work with primary neurons, especially if long-term measurements are desired. That is why it was decided to continue the work with a GECI, namely jRCaMP1a, as an indicator of activity within primary neurons.

A Neuronal-Tandem Approach to stimulate Spiral Ganglion Neurons

After the successful establishment of an optogenetic stimulus-response system in HEK Na_v 1.3 K_{IR} 2.1 cells, the next step was to transfer it to primary neurons. With CheRiff and jRCaMP1a, this study followed an all-optical approach to probe connectivity between spatially separated cells, cultured from spiral ganglion, hippocampal, and cortical tissue, where grafted light-

sensitive cells would drive spiral ganglion neurons and could thus form a hybrid interface to the auditory nerve. Jia et al. 2011 already performed a similar approach with a tandem cell unit in cardiovascular research for the establishment of a new generation of light-driven cardiac pacemakers and muscle actuators, where a ChR2 expressing cell line was used as a cell delivery system. For the first time, optical excitation and optical imaging was combined to capture light-triggered muscle contractions and high-resolution propagation maps of light-triggered electrical waves[166]. The cardiac tissue electromechanical function requires synchrony of excitation waves, achieved by cell-cell coupling via gap junction channels created by Connexin43. This is a fundamental different stimulus transmission system compared to neuronal signal transmission, where axons propagate a signal to adjacent neurons via dendrites. Nevertheless, the tandem principal, if proven successful, has potential safety advantages over viral transduction methods used in other optogenetic studies and may be applicable for study and treatment of neurologic disorders like hearing loss. However, SGN activity depends upon Ca^{2+}-dependent presynaptic exocytosis of glutamate from IHCs[167,168,169]. It can therefore be assumed, that glutamatergic communication between optogenetically activated excitatory hippocampal, or cortical neurons, to spiral ganglion neurons, with potential exploitation in the development of biohybrid systems used for the treatment of hearing loss, is feasible. For better understanding, **Fig. 38** shows a schematic drawing of the neuronal-tandem approach.

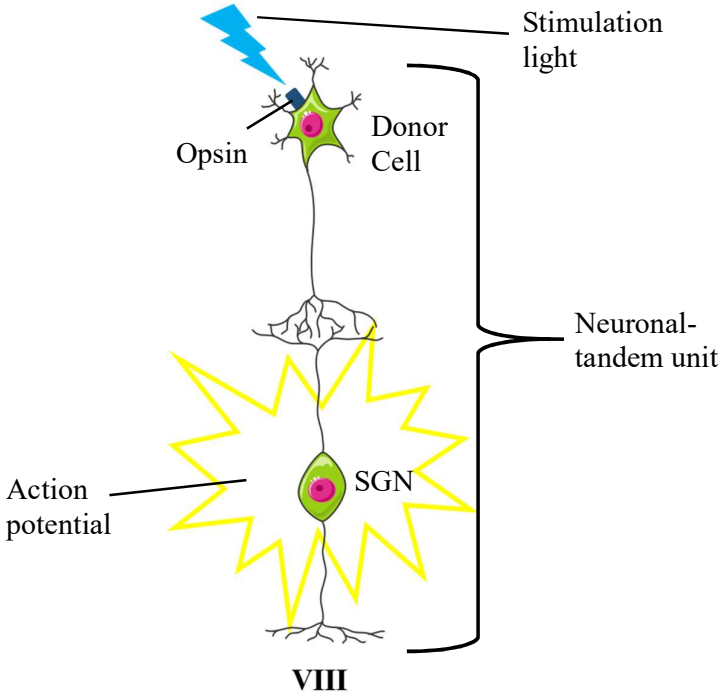

Fig. 38 Schematic Drawing of the Neuronal-Tandem Unit

A donor cell is transduced to express a light-sensitive ion channel for example ChR2. When coupled via synapses to excitable SGNs, they form an optically controllable functional neuronal-tandem unit, i.e. the SGNs will generate an action potential upon light-triggered opening of the depolarizing CheRiff in the donor neuron. The axons of the SGNs project to the central nervous system, to the cochlear nuclei, forming the acoustic portion of the VIII nerve.

The results of the experiments within this thesis showed that spiral ganglion cells are activated when nearby populations of cortical or hippocampal cultured neurons are stimulated with light, proving first: that the cells are inter-connected and second: that glutamatergic communication takes place between them. The results also indicate, that the stimulation efficiency of the SGNs generally increases with the stimulation length and reaches a plateau at 250 ms. This finding implicates, that longer stimuli do not result in stronger calcium signals. But the plateau formation could also be due to an effect called excitotoxicity, where strong stimulus and thus Ca^{2+} activity can lead to calcium-induced neuronal damage[170]. The findings within this thesis proved that it is possible to trigger SGNs with optogenetic activated neurons of other functional units, for example, the hippocampus or cortex. This might pave the way to use already optogenetically activated neurons, for instance, embedded in a hydrogel, as an implant. However, on the way to a neuronal-tandem cochlear implant, many obstacles must be overcome. Speaking of the long-term stability of the viral delivered opsin, it has to be said, that no whole lifespan animal studies have been performed until now. But it could already be shown,

that direct delivery of f-Chrimson to SGNs results in stable expression and robust optical evoked acoustic responses for 9 months in mice[141]. One major advantage of the neuronal-tandem approach over direct targeting the SGNs with light-driven opsins is that it is a non-viral strategy that does not rely on embryogenesis speaking of heterogeneity in expression level. The neuronal-tandem approach promises a more controlled way of opsin delivery since the transduction part can be performed *ex vivo*, under laboratory conditions. This means there is no risk of off-target transduction and the multiplicity of infection (MOI) can be adjusted in a way that no harmful effects occur. Nevertheless, the donor cells in the neuronal-tandem approach need to take up the opsin and in order to do so, the method of choice is still viral delivery. Adeno-associated viruses (AAV) appears to be highly promising candidates, since they have little potential for virus-related harm in the transduced cells while having a very high neuronal tropism with high expression levels and long-term availability of the desired transgene[171,172]. But besides the method of transduction, another problem is the stable long-term expression and trafficking of the microbial opsin to the plasma membrane[24,138]. There have been several improvements in the past years, like adding an export signal derived from inward rectifying potassium channels (K_{ir}), which resulted in enhanced export of the synthesized protein from the endoplasmic reticulum and increased the number of proteins integrated into the cell membrane[173]. Another improvement has been made by adding a K_{ir} family-derived trafficking signal, leading to an increase in membrane localization of the synthesized protein[174].

The opsin CheRiff used for stimulation within this thesis was chosen because of its blue shifted excitation maximum and to have as minimal crosstalk as possible with the calcium dye jRCaMP1a. However, for a clinical translation, the opsin of choice should show fast kinetics (to enable for physiological firing rates), red-shifted action spectrum (to reduce phototoxicity), large ion conductance (to allow for robust photocurrents) and confer high light sensitivity to the stimulating neurons (to reduce energy requirements and radiation). The temporal limitation of high frequency spiking is mainly caused by the closing kinetics of the channel. To date, some of the fastest known opsins are Chronos ($\tau_{off} < 1$ ms under physiological conditions) and vf-Chrimson ($\tau_{off} < 1.6$ ms under physiological conditions)[30]. But fast closing comes always with reduced neuronal light sensitivity since a shorter lifetime of the open channel leads to smaller photocurrents[141]. Thus, in order to enable optogenetic control of neurons at natural firing rates of SGNs and reasonable light thresholds future studies will be needed to balance between channel kinetics and light sensitivity. Besides the biosafety aspects, also long-term safety and stability of optical stimulation need to be evaluated. Stimulation rates of hundreds of Hz over years or even decades might lead to phototoxicity, or even changes in neural properties such as

long-term potentiation[175]. To date, irradiances of up to ~75 mW/mm² are considered to be safe for optogenetic applications *in vivo*, but there are also studies proving that there are no phototoxic effects such as apoptosis or cell loss at irradiances up to 600 mW/mm² with relatively long illumination times of 5 ms[176]. Nevertheless, safety limits depend also heavily on the wavelength needed to excite the opsin of choice since blue light for example has a higher potential of phototoxicity than red light. Data from eye restoration studies with orange light indicate that light of this wavelength is three orders of magnitude safer compared with blue light, enabling optogenetic stimulation at higher intensities when using red-shifted ChRs[177,178].

This thesis focused on the fundamental work for a neuronal-tandem approach and used glutamatergic neurons for this purpose. But for a clinical approach, future work could for example focus on autologous stem-cell transplantation. Exogenous stem cell transplantation within the cochlea into the inner ear is already possible[179]. One way to do it involves cell transplantation into the scala tympani via the round window, or through a cochleostomy and then stimulating them to move through the basilar membrane or surrounding tissue into the organ of Corti where the hair cells normally reside. The second approach involves directly injection of the cells into the scala media[179]. These routes could also be addressed for the delivery of the biohybrid implant. The combination with a hydrogel, for example, Matrigel enriched with neurotrophic factors like BDNF could have a positive effect on the integration of the implant, since BDNF is known to stimulate the neurite outgrowth from SGNs[180,181]. Matrigel, a solubilized basement membrane protein that begins to form a three-dimensional gel above 10 °C, is not only known to promote the differentiation of many cell types[182,183] but can also facilitate the outgrowth of differentiated cells from tissue explants[184]. In a transected rat spinal cord, a matrigel scaffold enriched with Schwann cells not only promoted axonal outgrowth in the vicinity of the grafts but also from neurons rostral to the explant[185]. Matrigel is liquid at low temperatures (< 4 °C) and becomes solid at a biological temperature (> 10 °C). Therefore, the liquid matrigel can be mixed with the optogenetic active donor neurons and injected into the scala tympani or the scala media as mentioned above. As the temperature increases, the Matrigel gradually solidifies, and the neurons are evenly distributed making it an ideal candidate for a biohybrid implant approach. Unfortunately, due to its murine origin, so far a clinical translation of Matrigel is not possible. However, a logical next step would be the transition from 2D to 3D *in vitro* studies. Optogenetic modified neurons could be co-cultured with the spiral ganglion of the inner ear, which would be transduced with jRCaMP1a for example. Preliminary experiments examine the feasibility of culturing the spiral ganglion within Matrigel and transduction of jRCaMP1a was already performed during this thesis (data

not shown). An explanted spiral ganglion was embedded in Matrigel and transduced with jRCaMP1a as described before and kept in growth media for one week. It could be clearly seen that the cord has formed long neurites. The fluorescence image also showed a very high level of expression of jRCaMP1a, which indicates a good transduction rate of the AAV particles, even in a Matrigel.

Structured Cell growth for directional signal transmission

One major drawback of the chosen method of spatial separation of the populations of HNs, CNs, and SGNs in a dish by silicone chambers is the somewhat undirected signal transmission. Therefore, defined gold-coated surfaces for structured cell growth were created to ultimately have directional signal transmission. As a first step, two different methods for applying the structures to the gold surfaces were compared; sputtering with a 3D printed mask vs. laser ablation of the gold film. In both cases, a glass cover slip was first sputtered with a thin gold nano layer and subsequently treated with mPEG, a polymer with a sulfur group that covalently binds to gold. The mPEG prevents cells from attaching to the gold layer. The 3D printing approach enables a rapid and inexpensive manufacturing process with customized designs. But, the thickness of the PLA mask and the resulting angles of incidence during the sputtering process lead to a blurry print (**Fig. 34**), which would impair the desired cell-repellent effect. With laser ablation, it was possible to yield more sharp patterns of ablated gold in a robust, fast, and repeatable way (**Fig. 35**). With a laser power of 50 mW and a scanning speed of 5 mm/s, robust patterns in the gold layer could be generated. A thickness of the gold layer of 30 nm allows still for optical experiments like calcium imaging. To ensure selective cell growth, the gold layer was further treated with mPEG to generate a cell repellent surface. Different concentrations (0 µM (H_2O); 0.01 µM; 0.1 µM; 1 µM and 5 µM) and sizes of mPEG (1 kDa; 6 kDa; 30 kDa) were evaluated to find the best parameters in terms of long-term stability and cell-repellency (**Fig. 36**). The mPEG size itself seemed to have no impact in terms of long-term stability. It was also observed, that with increasing mPEG concentration, the density of the cells within the laser-ablated areas increase, recognizable by the higher confluency. Finally, at a concentration of 5 µM, no single cells are distinguishable anymore by fluorescence signal of the GFP. It has been reported before, that the distance between adhered cells influences cell fusion and therefore the differentiation of cells[186]. Hence, it is likely, that due to the limited space of adherence, the cells reach a critical number, fuse together and form a syncytium. Taken

together, these results strongly support the hypothesis that mPEG in combination with thin gold layers and laser patterning, allows for structured cell growth.

Structured cell growth can be combined with calcium imaging and optogenetics to enable spatially directed signal generation

Finally, the gold-mPEG mediated structured cell growth approach was combined with optogenetics and calcium imaging to further validate the feasibility of this method. It could be shown, that stimulation by light leads to propagating calcium waves within the designated structure (**Fig. 37**). This technique could simply be applied to the neuronal-tandem approach to probe signal transmission from the donor-neurons to the SGNs. Another great advantage of the gold-mPEG method is that the distances between the cells can be set as desired easily by varying the laser-ablated regions. In that way, the signal transmission between the neurons could be studied under specified distances in a very robust and repeatable manner. However, other areas of application would also be conceivable. The thin gold film is able to conduct electricity as we figured out in capacitance measurements in our lab. Thus, it could be used to stimulate cells growing on AuCS electrically for example[187]. Electrical stimulation has been shown to play a crucial role in the differentiation process of human pluripotent stem cells into cardiomyocytes[188]. The gold-mPEG method developed within this thesis may be adapted in a way to combine architectural and electrical cues to generate a conductive microenvironment for the maturation of human embryonic and induced pluripotent stem cells to create *in vitro* models of healthy and diseased human cardiac tissues, which would be useful for screening new therapeutic agents efficacy. Recently it could be shown, that femtosecond laser fabricated micro through-holes in biodegradable polymer films enhance myoblast adhesion, and accelerates proliferation and differentiation of C2C12 cells[189]. Combining the AuCS method with micro through-holes, would probably enhance cell adhesion along the arrays and therefore induced a high-cell alignment, which is necessary to fabricate a tissue with arbitrary properties for tissue engineering applications.

8 Conclusion

This thesis was designed to establish a test-system for probing glutamatergic communication between optogenetically activated excitatory hippocampal neurons or cortical neurons to spiral ganglion neurons (SGN) with a potential exploitation in development of a biohybrid systems used for treatment of hearing loss. For the first time it could be shown, that it is possible to trigger SGNs with optogenetic activated neurons of other functional units for example hippocampus or cortex. Even very short stimulation pulses of 10 ms resulted in a stimulation efficiency of the SGNs reached roughly 60 % for both, HNs and CNs. The overall stimulation efficiency of the SGNs, triggered by the HNs, reached over 90 % with 250 ms and 500 ms pulses respectively. This indicates the feasibility of a neuronal-tandem approach as a tool to activate SGNs in an optogenetic manner. It could also be carried out, that the stimulation efficiency of the SGNs generally increases with the stimulation length and reaches a plateau at 250 ms. Longer stimuli resulted in plateau formation, indicating potential excitotoxicity. Stimulation of SGNs triggered by CNs showed slightly lower efficiency with the same parameters as used for HNs.

In order to achieve a more directed signal transmission, a laser structured cell growth system based on a thin gold layer and cell repellent mPEG-coating was established. The feasibility of this system was proven by combining optogenetic stimulation and calcium imaging in HL-1 cells.

The presented findings here are limited to a 2D *in vitro* environment and therefore cannot be translated directly to *in vivo* studies within the cochlea. An important next step would be feasibility studies on explanted spiral ganglion strands in a suitable 3D matrix like Matrigel. Optogenetic neurons could be co-cultured with the spiral ganglion of the inner ear, which could be transduced with jRCaMP1a for example. The activation by light could be then measured directly in an intact bundle of nerves. For a future clinical approach, work could focus on autologous stem-cell transplantation for example into the scala tympani via the round window.

This study indicates the great potential of a neuronal-tandem approach to generate a light-driven biohybrid cochlear implant. Compared to other optogenetic approaches to restore hearing, it promises a more controlled way of opsin delivery, since the transduction part can be performed under laboratory conditions. Also regarding safety issues, the neuronal-tandem approach offers the advantage of genetic modification outside of the patient.

9 Appendix

Supplementary video

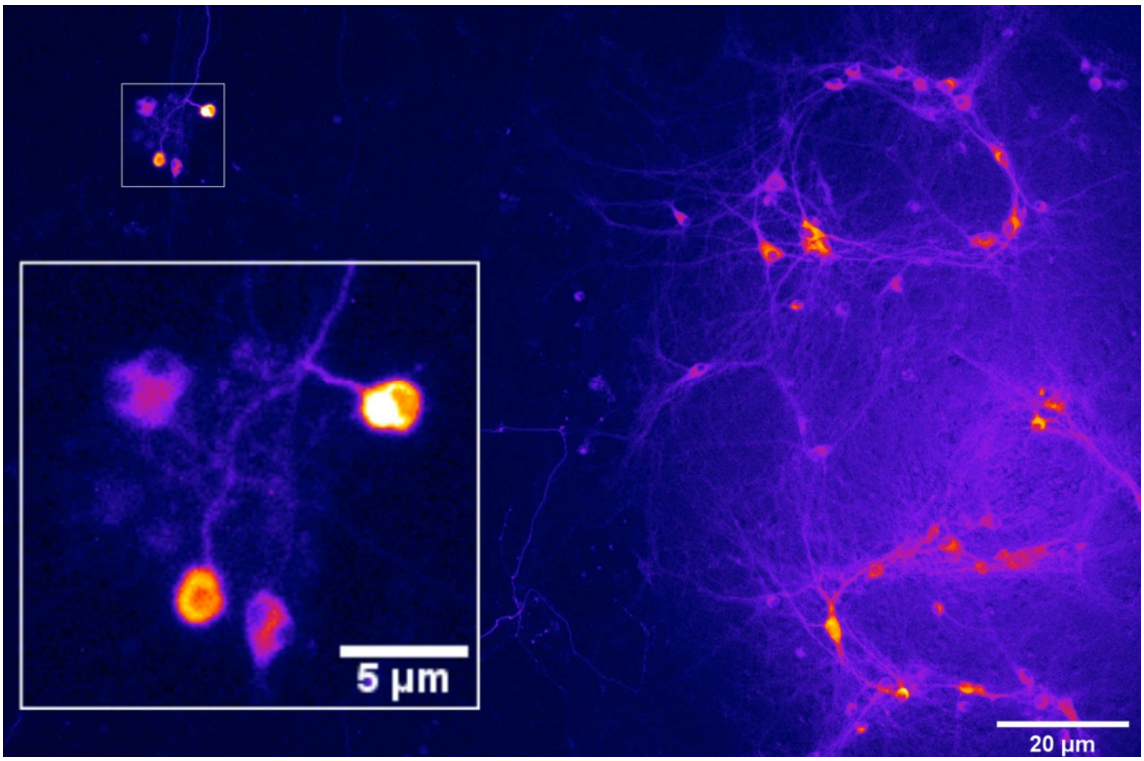

Video S 1: Fluorescence series of spiral ganglion neurons activated by light-triggered cortex neurons

Example video of the neuronal-tandem trigger approach between SGNs (left, white box) and optogenetic modified CNs (right). The stimulation LED fiber is located directly above the CNs and two blue light pulse of 250 ms are applied with a gap of 5 s in between.

The video is available on:

https://onlinelibrary.wiley.com/action/downloadSupplement?doi=10.1002%2Ftbio.202100002&file=tbio202100002-sup-0002-VideoS1.mp4

References

1. P. Mazzarello, D. E. Haines, and M. U. Manto, “Camillo Golgi on cerebellar granule cells,” in Cerebellum **11**(1), pp. 5–24 (2012) [doi:10.1007/s12311-012-0372-8].

2. A. DEWULF, “[The significance of the works of Ramón y Cajal carried out with Golgi’s method],” Acta Neurol. Psychiatr. Belg. **54**(7), 545—555 (1954).

3. K. A. Id et al., “The Human Brain Project — Synergy between neuroscience , computing , informatics , and brain-inspired technologies,” PLoS Biol, 1–7 (2019).

4. S. J. van Albada et al., “Performance Comparison of the Digital Neuromorphic Hardware SpiNNaker and the Neural Network Simulation Software NEST for a Full-Scale Cortical Microcircuit Model,” Front. Neurosci. **12**, 291 (2018) [doi:10.3389/fnins.2018.00291].

5. J. F. Storm et al., “Consciousness regained: Disentangling mechanisms, brain systems, and behavioral responses,” in Journal of Neuroscience **37**(45), pp. 10882–10893 (2017) [doi:10.1523/JNEUROSCI.1838-17.2017].

6. N. Takahashi et al., “Active cortical dendrites modulate perception,” Science (80-.). **354**(6319), 1587–1590 (2016) [doi:10.1126/science.aah6066].

7. F. Gentile et al., “Approaching the ground truth: Revealing the functional organization of human multisensory STC using ultra-high field fMRI,” J. Neurosci. **37**(42), 10104–10113 (2017) [doi:10.1523/JNEUROSCI.0146-17.2017].

8. “The Human Connectome Project,” <http://www.humanconnectomeproject.org/>.

9. D. C. Van Essen et al., “The Human Connectome Project: A data acquisition perspective,” Neuroimage **62**(4), 2222–2231 (2012) [doi:https://doi.org/10.1016/j.neuroimage.2012.02.018].

10. “lifespan-studies @ www.humanconnectome.org.”

11. “disease-studies @ www.humanconnectome.org.”

12. A. P. Alivisatos et al., “The Brain Activity Map Project and the Challenge of Functional Connectomics,” Neuron **74**(6), 970–974 (2012) [doi:10.1016/j.neuron.2012.06.006].

13. A. M. Stamatakis et al., “Simultaneous optogenetics and cellular resolution calcium imaging during active behavior using a miniaturized microscope,” Front. Neurosci. **12**(JUL), 1–16 (2018) [doi:10.3389/fnins.2018.00496].

14. N. C. Klapoetke et al., “Independent optical excitation of distinct neural populations,” Nat. Methods **11**(3), 338–346 (2014) [doi:10.1038/nmeth.2836].

15. J. Akerboom et al., “Genetically encoded calcium indicators for multi-color neural activity imaging and combination with optogenetics,” Front. Mol. Neurosci. **6**(FEB), 1–29 (2013) [doi:10.3389/fnmol.2013.00002].

16. S. W. Flavell and M. E. Greenberg, “Expression and Plasticity of the Nervous System,” Annu Rev Neurosci, 563–590 (2008) [doi:10.1146/annurev.neuro.31.060407.125631.Signaling].

17. E. Hanse and A. Konnerth, “Calcium and Activity-Dependent Synaptic Plasticity,” in Integrative Aspects of Calcium Signalling, pp. 333–358 (1998) [doi:10.1007/978-1-4899-1901-4_16].

18. T. Knöpfel and C. Song, “Optical voltage imaging in neurons: moving from technology development to practical tool,” Nat. Rev. Neurosci. **20**(12), 719–727 (2019) [doi:10.1038/s41583-019-0231-4].

19. C. Nguyen et al., “Simultaneous voltage and calcium imaging and optogenetic stimulation with high sensitivity and a wide field of view,” Biomed. Opt. Express **10**(2), 789 (2019) [doi:10.1364/boe.10.000789].

20. T. Bruegmann et al., “Optogenetic control of heart muscle in vitro and in vivo,” Nat. Methods **7**(11), 897–900 (2010) [doi:10.1038/nmeth.1512].

21. M. Jeschke and T. Moser, “Considering optogenetic stimulation for cochlear implants,” Hear. Res. **322**, 224–234, Elsevier B.V (2015) [doi:10.1016/j.heares.2015.01.005].

22. J. Tønnesen and M. Kokaia, “Epilepsy and optogenetics: can seizures be controlled by light?,” Clin. Sci. (Lond). **131**(14), 1605–1616, England (2017) [doi:10.1042/CS20160492].

23. R. Marc, R. Pfeiffer, and B. Jones, “Retinal prosthetics, optogenetics, and chemical photoswitches,” in ACS Chemical Neuroscience **5**(10), pp. 895–901 (2014) [doi:10.1021/cn5001233].

24. C. Wrobel et al., “Optogenetic stimulation of cochlear neurons activates the auditory pathway and restores auditory-driven behavior in deaf adult gerbils,” Sci. Transl. Med. **10**(449) (2018) [doi:10.1126/scitranslmed.aao0540].

25. V. H. Hernandez et al., “Optogenetic stimulation of the auditory pathway,” J. Clin. Invest. **124**(3), 1114–1129, The American Society for Clinical Investigation (2014) [doi:10.1172/JCI69050].

26. Y. Shu et al., “Identification of Adeno-Associated Viral Vectors That Target Neonatal and Adult Mammalian Inner Ear Cell Subtypes.,” Hum. Gene Ther. **27**(9), 687–699 (2016) [doi:10.1089/hum.2016.053].

27. A. Roemer et al., “Biohybrid cochlear implants in human neurosensory restoration.,” Stem Cell Res. Ther. **7**(1), 148 (2016) [doi:10.1186/s13287-016-0408-y].

28. S. Kateriya et al., “‘ Vision ’ in Single-Celled Algae,” Am. J. Obstet. Gynecol., 1–5 (2021).

29. G. Nagel et al., “Channelrhodopsin-1: a light-gated proton channel in green algae.,” Science **296**(5577), 2395–2398, United States (2002) [doi:10.1126/science.1072068].

30. L. A. Gunaydin et al., “Ultrafast optogenetic control.,” Nat. Neurosci. **13**(3), 387–392, United States (2010) [doi:10.1038/nn.2495].

31. E. S. Boyden et al., “Millisecond-timescale, genetically targeted optical control of neural activity,” Nat. Neurosci. **8**(9), 1263–1268 (2005) [doi:10.1038/nn1525].

32. G. Nagel et al., “Light activation of channelrhodopsin-2 in excitable cells of Caenorhabditis elegans triggers rapid behavioral responses.,” Curr. Biol. **15**(24), 2279–2284, England (2005) [doi:10.1016/j.cub.2005.11.032].

33. D. Oesterhelt, “The structure and mechanism of the family of retinal proteins from halophilic archaea,” Curr. Opin. Struct. Biol. **8**(4), 489–500 (1998) [doi:https://doi.org/10.1016/S0959-440X(98)80128-0].

34. F. Braun and P. Hegemann, “Two Light-Activated Conductances in the Eye of the Green Alga Volvox carteri,” Biophys. J. **76**(March), 1668–1678 (1999).

35. G. Nagel et al., “Channelrhodopsin-2, a directly light-gated cation-selective membrane channel.,” Proc. Natl. Acad. Sci. U. S. A. **100**(24), 13940–13945 (2003) [doi:10.1073/pnas.1936192100].

36. A. Bi et al., “Ectopic Expression of a Microbial-Type Rhodopsin Restores Visual Responses in Mice with Photoreceptor Degeneration,” Neuron **50**(1), 23–33 (2006) [doi:https://doi.org/10.1016/j.neuron.2006.02.026].

37. X. Li et al., “Fast noninvasive activation and inhibition of neural and network activity by vertebrate rhodopsin and green algae channelrhodopsin,” Proc. Natl. Acad. Sci. **102**(49), 17816–17821, National Academy of Sciences (2005) [doi:10.1073/pnas.0509030102].

38. T. Ishizuka et al., “Kinetic evaluation of photosensitivity in genetically engineered neurons expressing green algae light-gated channels.,” Neurosci. Res. **54**(2), 85–94, Ireland (2006) [doi:10.1016/j.neures.2005.10.009].

39. J. G. Bernstein and E. S. Boyden, “Optogenetic tools for analyzing the neural circuits of behavior,” Trends Cogn. Sci. **15**(12), 592–600 (2011) [doi:https://doi.org/10.1016/j.tics.2011.10.003].

40. A. Adamantidis et al., “Optogenetics: 10 years after ChR2 in neurons—views from the community,” Nat. Neurosci. **18**(9), 1202–1212 (2015) [doi:10.1038/nn.4106].

41. Y. Chen, M. Xiong, and S.-C. Zhang, “Illuminating Parkinson’s therapy with optogenetics,” Nat. Biotechnol. **33**(2), 149–150 (2015) [doi:10.1038/nbt.3140].

42. D. Huber et al., “Sparse optical microstimulation in barrel cortex drives learned behaviour in freely moving mice.,” Nature **451**(7174), 61–64 (2008) [doi:10.1038/nature06445].

43. F. Zhang et al., “Channelrhodopsin-2 and optical control of excitable cells.,” Nat. Methods **3**(10), 785–792, United States (2006) [doi:10.1038/nmeth936].

44. J. Y. Lin, “A user’s guide to channelrhodopsin variants: features, limitations and future developments.,” Exp. Physiol. **96**(1), 19–25 (2011) [doi:10.1113/expphysiol.2009.051961].

45. F. Zhang et al., “Red-shifted optogenetic excitation: a tool for fast neural control derived from Volvox carteri.,” Nat. Neurosci. **11**(6), 631–633 (2008) [doi:10.1038/nn.2120].

46. O. Yizhar et al., “Neocortical excitation/inhibition balance in information processing and social dysfunction.,” Nature **477**(7363), 171–178 (2011) [doi:10.1038/nature10360].

47. F. Zhang et al., “Multimodal fast optical interrogation of neural circuitry,” Nature **446**(7136), 633–639 (2007) [doi:10.1038/nature05744].

48. V. A. Lórenz-Fonfría and J. Heberle, “Channelrhodopsin unchained: Structure and mechanism of a light-gated cation channel,” Biochim. Biophys. Acta - Bioenerg.

1837(5), 626–642, Elsevier B.V. (2014) [doi:10.1016/j.bbabio.2013.10.014].

49. K. Nikolic et al., "Photocycles of channelrhodopsin-2," Photochem. Photobiol. **85**(1), 400–411 (2009) [doi:10.1111/j.1751-1097.2008.00460.x].

50. V. A. Lórenz-Fonfría et al., "Transient protonation changes in channelrhodopsin-2 and their relevance to channel gating," Proc. Natl. Acad. Sci. U. S. A. **110**(14) (2013) [doi:10.1073/pnas.1219502110].

51. M. J. Berridge, P. Lipp, and M. D. Bootman, "The versatility and universality of calcium signalling," Nat. Rev. Mol. Cell Biol. **1**(1), 11–21 (2000) [doi:10.1038/35036035].

52. A. F. Dulhunty, "EXCITATION – CONTRACTION COUPLING FROM THE 1950s INTO THE NEW MILLENNIUM," Clin. Exp. Pharmacol. Physiol.(January), 763–772 (2006) [doi:10.1111/j.1440-1681.2006.04441.x].

53. S. Orrenius, B. Zhivotovsky, and P. Nicotera, "REGULATION OF CELL DEATH : THE CALCIUM – APOPTOSIS LINK," Nat. Rev. Mol. Cell Biol. Vol. **4**(July), 552–565 (2003) [doi:10.1038/nrm1150].

54. E. Neher and T. Sakaba, "Multiple Roles of Calcium Ions in the Regulation of Neurotransmitter Release," Neuron **59**(6), 861–872 (2008) [doi:https://doi.org/10.1016/j.neuron.2008.08.019].

55. R. S. Zucker, "Calcium- and activity-dependent synaptic plasticity," Curr. Opin. Neurobiol. **9**(3), 305–313 (1999) [doi:https://doi.org/10.1016/S0959-4388(99)80045-2].

56. M. R. Lyons and A. E. West, "Mechanisms of specificity in neuronal activity-regulated gene transcription," Prog. Neurobiol. **94**(3), 259–295 (2011) [doi:https://doi.org/10.1016/j.pneurobio.2011.05.003].

57. B. Schwaller, "Cytosolic Ca 2," 1–21 (2021).

58. M. J. Higley and B. L. Sabatini, "Calcium Signaling in Dendrites and Spines: Practical and Functional Considerations," Neuron **59**(6), 902–913 (2008) [doi:https://doi.org/10.1016/j.neuron.2008.08.020].

59. S. Fucile, "Ca2+ permeability of nicotinic acetylcholine receptors," Cell Calcium **35**(1), 1–8 (2004) [doi:https://doi.org/10.1016/j.ceca.2003.08.006].

60. M. J. Berridge, M. D. Bootman, and H. L. Roderick, "Calcium signalling: dynamics,

homeostasis and remodelling," Nat. Rev. Mol. Cell Biol. **4**(7), 517–529 (2003) [doi:10.1038/nrm1155].

61. M. R. Duchen, "Topical Review Contributions of mitochondria to animal physiology : from homeostatic sensor to calcium signalling and cell death," J. Physiol., 1–17 (1999).

62. J. P. Rickgauer, K. Deisseroth, and D. W. Tank, "Simultaneous cellular-resolution optical perturbation and imaging of place cell firing fields," Nat. Neurosci. **17**(12), 1816–1824 (2014) [doi:10.1038/nn.3866].

63. O. A. Shemesh et al., "Temporally precise single-cell-resolution optogenetics," Nat. Neurosci. **20**(12), 1796–1806 (2017) [doi:10.1038/s41593-017-0018-8].

64. M. Scanziani and M. Häusser, "Electrophysiology in the age of light," Nature **461** (2009) [doi:10.1038/nature08540].

65. N. Ji et al., "Advances in the speed and resolution of light microscopy," Curr. Opin. Neurobiol. **18**(6), 605–616 (2008) [doi:https://doi.org/10.1016/j.conb.2009.03.009].

66. B. A. Wilt et al., "Advances in Light Microscopy for Neuroscience," Annu. Rev. Neurosci. **32**(1), 435–506 (2009) [doi:10.1146/annurev.neuro.051508.135540].

67. X. Han and E. S. Boyden, "Multiple-Color Optical Activation, Silencing, and Desynchronization of Neural Activity, with Single-Spike Temporal Resolution," PLoS One **2**(3), 1–12, Public Library of Science (2007) [doi:10.1371/journal.pone.0000299].

68. R. A. Stepnoski et al., "Noninvasive detection of changes in membrane potential in cultured neurons by light scattering," PNAS **88**(November), 9382–9386 (1991).

69. A. Grinvald and R. Hildesheim, "VSDI : A NEW ERA IN FUNCTIONAL IMAGING OF CORTICAL DYNAMICS," Nat. Rev. Neurosci. **5**(November), 874–885 (2004) [doi:10.1038/nrn1536].

70. B. M. Salzberg et al., "Optical recording of action potentials from vertebrate nerve terminals using potentiometric probes provides evidence for sodium and calcium components," Nature **306**(5938), 36–40 (1983) [doi:10.1038/306036a0].

71. M. Djurisic et al., "Voltage Imaging from Dendrites of Mitral Cells: EPSP Attenuation and Spike Trigger Zones," J. Neurosci. **24**(30), 6703–6714, Society for Neuroscience (2004) [doi:10.1523/JNEUROSCI.0307-04.2004].

72. A. Arieli et al., “Dynamics of Ongoing Activity : Explanation of the Large Variability in Evoked Cortical Responses,” Science (80-.).(4).

73. M. S. Siegel and E. Y. Isacoff, “A Genetically Encoded Optical Probe of Membrane Voltage,” Neuron **19**(4), 735–741 (1997) [doi:https://doi.org/10.1016/S0896-6273(00)80955-1].

74. H. Tsutsui et al., “Improving membrane voltage measurements using FRET with new fluorescent proteins.,” Nat. Methods **5**(8), 683–685, United States (2008) [doi:10.1038/nmeth.1235].

75. B. Chanda et al., “A hybrid approach to measuring electrical activity in genetically specified neurons,” Nat. Neurosci. **8**(11), 1619–1626 (2005) [doi:10.1038/nn1558].

76. F. St-Pierre et al., “High-fidelity optical reporting of neuronal electrical activity with an ultrafast fluorescent voltage sensor,” Nat. Neurosci. **17**(6), 884–889 (2014) [doi:10.1038/nn.3709].

77. L. Sjulson and G. Miesenböck, “REVIEWS Optical Recording of Action Potentials and Other Discrete Physiological Events : A Perspective from Signal Detection Theory,” Am. Physiol. Soc., 47–55 (2021).

78. C. A. Werley, M.-P. Chien, and A. E. Cohen, “Ultrawidefield microscope for high-speed fluorescence imaging and targeted optogenetic stimulation,” Biomed. Opt. Express **8**(12), 5794–5813, OSA (2017) [doi:10.1364/BOE.8.005794].

79. D. R. Hochbaum et al., “All-optical electrophysiology in mammalian neurons using engineered microbial rhodopsins,” Nat. Methods **11**(8), 825–833 (2014) [doi:10.1038/nmeth.3000].

80. C. Grienberger and A. Konnerth, “Imaging Calcium in Neurons,” Neuron **73**(5), 862–885 (2012) [doi:https://doi.org/10.1016/j.neuron.2012.02.011].

81. J. R. Berlin, J. W. Bassani, and D. M. Bers, “Intrinsic cytosolic calcium buffering properties of single rat cardiac myocytes,” Biophys. J. **67**(4), 1775–1787 (1994) [doi:https://doi.org/10.1016/S0006-3495(94)80652-6].

82. T. Nagai et al., “Expanded dynamic range of fluorescent indicators for Ca2+ by circularly permuted yellow fluorescent proteins,” Proc. Natl. Acad. Sci. **101**(29), 10554–10559, National Academy of Sciences (2004) [doi:10.1073/pnas.0400417101].

83. M. L. Fletcher et al., “Optical Imaging of Postsynaptic Odor Representation in the Glomerular Layer of the Mouse Olfactory Bulb,” J. Neurophysiol., 817–830 (2021) [doi:10.1152/jn.00020.2009.].

84. S. H. Chalasani et al., “Dissecting a circuit for olfactory behaviour in Caenorhabditis elegans,” Nature **450**(7166), 63–70 (2007) [doi:10.1038/nature06292].

85. D. A. Dombeck et al., “Functional imaging of hippocampal place cells at cellular resolution during virtual navigation,” Nat. Neurosci. **13**(11), 1433–1440 (2010) [doi:10.1038/nn.2648].

86. J. Nakai, M. Ohkura, and K. Imoto, “A high signal-to-noise Ca2+ probe composed of a single green fluorescent protein,” Nat. Biotechnol. **19**(2), 137–141 (2001) [doi:10.1038/84397].

87. T. Chen et al., “Ultrasensitive fluorescent proteins for imaging neuronal activity,” Nature [doi:10.1038/nature12354].

88. S. Peron, T.-W. Chen, and K. Svoboda, “Comprehensive imaging of cortical networks,” Curr. Opin. Neurobiol. **32**, 115–123 (2015) [doi:https://doi.org/10.1016/j.conb.2015.03.016].

89. K. Svoboda and S. M. Block, “BIOLOGICAL APPLICATIONS OF OPTICAL FORCES,” Annu. Rev. Biochem. (1994).

90. S. Kredel et al., “mRuby, a Bright Monomeric Red Fluorescent Protein for Labeling of Subcellular Structures,” PLoS One **4**(2), 1–7, Public Library of Science (2009) [doi:10.1371/journal.pone.0004391].

91. N. C. Shaner et al., “Improving the photostability of bright monomeric orange and red fluorescent proteins.,” Nat. Methods **5**(6), 545–551 (2008) [doi:10.1038/nmeth.1209].

92. H. Dana et al., “Sensitive red protein calcium indicators for imaging neural activity,” Elife **5**(MARCH2016), 1–24 (2016) [doi:10.7554/eLife.12727].

93. S. Kerruth et al., “The kinetic mechanisms of fast-decay red-fluorescent genetically encoded calcium indicators,” J. Biol. Chem. **294**(11), 3934–3946 (2019) [doi:https://doi.org/10.1074/jbc.RA118.004543].

94. A. M. Packer et al., “Simultaneous all-optical manipulation and recording of neural circuit activity with cellular resolution in vivo,” Nat. Methods **12**(2), 140–146 (2015)

[doi:10.1038/nmeth.3217].

95. V. Emiliani et al., "All-Optical Interrogation of Neural Circuits," J. Neurosci. **35**(41), 13917–13926 (2015) [doi:10.1523/JNEUROSCI.2916-15.2015].

96. S. Nirenberg and C. Pandarinath, "Retinal prosthetic strategy with the capacity to restore normal vision.," Proc. Natl. Acad. Sci. U. S. A. **109**(37), 15012–15017 (2012) [doi:10.1073/pnas.1207035109].

97. J. N. Fayad et al., "Cochlear and Brainstem Auditory Prostheses 'Neural Interface for Hearing Restoration: Cochlear and Brain Stem Implants,'" Proc. IEEE **96**(7), 1085–1095 (2008) [doi:10.1109/JPROC.2008.922577].

98. R. B. North, "Neural Interface Devices: Spinal Cord Stimulation Technology," Proc. IEEE **96**(7), 1108–1119 (2008) [doi:10.1109/JPROC.2008.922558].

99. K. L. Noblett and L. A. Cadish, "Sacral nerve stimulation for the treatment of refractory voiding and bowel dysfunction.," Am. J. Obstet. Gynecol. **210**(2), 99–106, United States (2014) [doi:10.1016/j.ajog.2013.07.025].

100. K. Warwick et al., "The application of implant technology for cybernetic systems.," Arch. Neurol. **60**(10), 1369–1373, United States (2003) [doi:10.1001/archneur.60.10.1369].

101. M. Andy and R. Emma, "The Medicalization of Cyberspace," J. Information, Commun. Ethics Soc. **7**(2/3), 211–213, Emerald Group Publishing Limited (2009) [doi:10.1108/14779960910955918].

102. G. Santhanam et al., "A high-performance brain-computer interface.," Nature **442**(7099), 195–198, England (2006) [doi:10.1038/nature04968].

103. A. Y. Chow, A. K. Bittner, and M. T. Pardue, "The artificial silicon retina in retinitis pigmentosa patients (an American Ophthalmological Association thesis).," Trans. Am. Ophthalmol. Soc. **108**, 120–154 (2010).

104. A. B. Schwartz et al., "Brain-Controlled Interfaces: Movement Restoration with Neural Prosthetics," Neuron **52**(1), 205–220 (2006) [doi:https://doi.org/10.1016/j.neuron.2006.09.019].

105. A. J. Young and D. P. Ferris, "State of the Art and Future Directions for Lower Limb Robotic Exoskeletons," IEEE Trans. Neural Syst. Rehabil. Eng. **25**(2), 171–182 (2017)

[doi:10.1109/TNSRE.2016.2521160].

106. B. S. Wilson, “Cochlear Prosthesis☆,” in Reference Module in Neuroscience and Biobehavioral Psychology, Elsevier (2017) [doi:https://doi.org/10.1016/B978-0-12-809324-5.02025-3].

107. Y. A. Connie Rye, Robert Wise, Vladimir Jurukovski, Jean DeSaix, Jung Choi, “Biology,” OpenStax (2016).

108. A. Vaiserman, O. Lushchak, and D. Purves, *Neuroscience: Third Edition*, in Encyclopedia of Biomedical Gerontology (2019) [doi:10.1016/B978-0-12-801238-3.62132-3].

109. O. Ropshkow, “Cochlea-crosssection,” 2004, <https://commons.wikimedia.org/wiki/File:Cochlea-crosssection.png>.

110. Madhero88, “Organ of Corti,” 2009, <https://commons.wikimedia.org/wiki/File:Organ_of_corti.svg>.

111. R. Fettiplace, “Hair Cell Transduction, Tuning, and Synaptic Transmission in the Mammalian Cochlea.,” Compr. Physiol. **7**(4), 1197–1227 (2017) [doi:10.1002/cphy.c160049].

112. OpenStax, “Frequency Coding in The Cochlea,” 2016, <https://commons.wikimedia.org/wiki/File:1408_Frequency_Coding_in_The_Cochlea.jpg>.

113. A. Vavakou, N. P. Cooper, and M. van der Heijden, “The frequency limit of outer hair cell motility measured in vivo,” Elife **8**, A. J. King et al., Eds., e47667, eLife Sciences Publications, Ltd (2019) [doi:10.7554/eLife.47667].

114. T. Moser and C. Vogl, “New insights into cochlear sound encoding.,” F1000Research **5** (2016) [doi:10.12688/f1000research.8924.1].

115. L. Lagnado and F. Schmitz, “Ribbon Synapses and Visual Processing in the Retina.,” Annu. Rev. Vis. Sci. **1**, 235–262, United States (2015) [doi:10.1146/annurev-vision-082114-035709].

116. A. Kurabi et al., “Cellular mechanisms of noise-induced hearing loss,” Hear. Res. **349**, 129–137 (2017) [doi:https://doi.org/10.1016/j.heares.2016.11.013].

117. “No Title,” <https://www.who.int/news-room/fact-sheets/detail/deafness-and-hearing-loss>.

118. R. J. H. Smith, J. F. Bale, and K. R. White, “Sensorineural hearing loss in children,” Lancet **365**(9462), 879–890 (2005) [doi:https://doi.org/10.1016/S0140-6736(05)71047-3].

119. A. Sharma, M. F. Dorman, and A. J. Spahr, “A sensitive period for the development of the central auditory system in children with cochlear implants: implications for age of implantation.,” Ear Hear. **23**(6), 532–539, United States (2002) [doi:10.1097/00003446-200212000-00004].

120. J. G. Clark, “Uses and abuses of hearing loss classification.,” ASHA **23**(7), 493–500, United States (1981).

121. R. T. Ramsden, “Cochlear implants and brain stem implants.,” Br. Med. Bull. **63**, 183–193 (2002) [doi:10.1093/bmb/63.1.183].

122. A. Kral and A. Sharma, “Developmental neuroplasticity after cochlear implantation.,” Trends Neurosci. **35**(2), 111–122 (2012) [doi:10.1016/j.tins.2011.09.004].

123. R. K. Shepherd and N. A. Hardie, “Deafness-induced changes in the auditory pathway: Implications for cochlear implants,” Audiol. Neuro-Otology **6**(6), 305–318 (2001) [doi:10.1159/000046843].

124. H. H. Lim, M. Lenarz, and T. Lenarz, “Auditory midbrain implant: a review.,” Trends Amplif. **13**(3), 149–180 (2009) [doi:10.1177/1084713809348372].

125. S. R. Otto et al., “Audiologic outcomes with the penetrating electrode auditory brainstem implant.,” Otol. Neurotol. Off. Publ. Am. Otol. Soc. Am. Neurotol. Soc. [and] Eur. Acad. Otol. Neurotol. **29**(8), 1147–1154, United States (2008) [doi:10.1097/MAO.0b013e31818becb4].

126. G. Kohlberg et al., “Does Cochlear Implantation Restore Music Appreciation ?,” 2013–2014 (2014) [doi:10.1002/lary.24171].

127. T. Lenarz, “Cochlear implant - state of the art.,” GMS Curr. Top. Otorhinolaryngol. Head Neck Surg. **16**, Doc04 (2017) [doi:10.3205/cto000143].

128. J. J. 3rd Galvin, Q.-J. Fu, and R. V Shannon, “Melodic contour identification and music perception by cochlear implant users.,” Ann. N. Y. Acad. Sci. **1169**, 518–533 (2009)

[doi:10.1111/j.1749-6632.2009.04551.x].

129. A. Kral et al., “Spatial resolution of cochlear implants: the electrical field and excitation of auditory afferents,” Hear. Res. **121**(1), 11–28 (1998) [doi:https://doi.org/10.1016/S0378-5955(98)00061-6].

130. J. Lee, J. Nadol J.B., and D. K. Eddington, “Depth of Electrode Insertion and Postoperative Performance in Humans with Cochlear Implants: A Histopathologic Study,” Audiol. Neurotol. **15**(5), 323–331 (2010) [doi:10.1159/000289571].

131. J. C. Middlebrooks and R. L. Snyder, “Auditory Prosthesis with a Penetrating Nerve Array,” J. Assoc. Res. Otolaryngol. **8**(2), 258–279 (2007) [doi:10.1007/s10162-007-0070-2].

132. A. K. Wise et al., “Evaluation of focused multipolar stimulation for cochlear implants in long-term deafened cats,” J. Neural Eng. **12**, 1–26 (2015) [doi:10.1088/1741-2560/12/3/036003].

133. V. H. Hernandez et al., “Optogenetic stimulation of the auditory nerve.,” J. Vis. Exp.(92), e52069 (2014) [doi:10.3791/52069].

134. A. Dieter, D. Keppeler, and T. Moser, “Towards the optical cochlear implant: optogenetic approaches for hearing restoration.,” EMBO Mol. Med. **12**(4), e11618 (2020) [doi:10.15252/emmm.201911618].

135. A. D. Izzo et al., “Selectivity of neural stimulation in the auditory system: a comparison of optic and electric stimuli.,” J. Biomed. Opt. **12**(2), 21008, United States (2007) [doi:10.1117/1.2714296].

136. N. Kallweit et al., “Optoacoustic effect is responsible for laser-induced cochlear responses.,” Sci. Rep. **6**, 28141 (2016) [doi:10.1038/srep28141].

137. T. Moser and A. Dieter, “Towards optogenetic approaches for hearing restoration,” Biochem. Biophys. Res. Commun. **527**(2), 337–342 (2020) [doi:10.1016/j.bbrc.2019.12.126].

138. C. Wrobel et al., “Optogenetic stimulation of cochlear neurons activates the auditory pathway and restores auditory-driven behavior in deaf adult gerbils.,” Sci. Transl. Med. **10**(449), United States (2018) [doi:10.1126/scitranslmed.aao0540].

139. M. J. Duarte et al., “Ancestral Adeno-Associated Virus Vector Delivery of Opsins to

Spiral Ganglion Neurons : Implications for Optogenetic Cochlear Implants," Mol. Ther. **26**(8), 1931–1939, Elsevier Ltd. (2018) [doi:10.1016/j.ymthe.2018.05.023].

140. T. Moser, "Optogenetic stimulation of the auditory pathway for research and future prosthetics.," Curr. Opin. Neurobiol. **34**, 29–36, England (2015) [doi:10.1016/j.conb.2015.01.004].

141. T. Mager et al., "High frequency neural spiking and auditory signaling by ultrafast red-shifted optogenetics," Nat. Commun., Springer US (2018) [doi:10.1038/s41467-018-04146-3].

142. O. Kaiser et al., "TGF-beta superfamily member activin A acts with BDNF and erythropoietin to improve survival of spiral ganglion neurons in vitro," Neuropharmacology **75**, 416–425 (2013) [doi:https://doi.org/10.1016/j.neuropharm.2013.08.008].

143. A. Landy, "Dynamic, structural, and regulatory aspects of lambda site-specific recombination.," Annu. Rev. Biochem. **58**, 913–949, United States (1989) [doi:10.1146/annurev.bi.58.070189.004405].

144. A. Landy, "MultiSite Gateway ® Three- Fragment Vector Construction" (2012).

145. F. Schmieder et al., "Optogenetic Stimulation of Human Neural Networks Using Fast Ferroelectric Spatial Light Modulator—Based Holographic Illumination," Appl. Sci. **8**(7) (2018) [doi:10.3390/app8071180].

146. W. A. Saber et al., "All-optical assay to study biological neural networks," Front. Neurosci. **12**(JUL), 1–12 (2018) [doi:10.3389/fnins.2018.00451].

147. P. Hydrogels et al., "Surface Patterning of Gold Nanoparticles on," Polymers (Basel). (2017) [doi:10.3390/polym9050154].

148. M. Schomaker et al., "Characterization of nanoparticle mediated laser transfection by femtosecond laser pulses for applications in molecular medicine," J. Nanobiotechnology **13**(1), 10 (2015) [doi:10.1186/s12951-014-0057-1].

149. W. C. Claycomb et al., "HL-1 cells: A cardiac muscle cell line that contracts and retains phenotypic characteristics of the adult cardiomyocyte," Proc. Natl. Acad. Sci. U. S. A. **95**(6), 2979–2984 (1998) [doi:10.1073/pnas.95.6.2979].

150. A. Rita Costa et al., "Guidelines to cell engineering for monoclonal antibody

production.," Eur. J. Pharm. Biopharm. Off. J. Arbeitsgemeinschaft fur Pharm. Verfahrenstechnik e.V **74**(2), 127–138, Netherlands (2010) [doi:10.1016/j.ejpb.2009.10.002].

151. K. Kogure et al., "A tissue culture assay for tetrodotoxin, saxitoxin and related toxins," Toxicon **26**(2), 191–197 (1988) [doi:https://doi.org/10.1016/0041-0101(88)90171-7].

152. M. A. Dichter, A. S. Tischler, and L. A. Greene, "Nerve growth factor-induced increase in electrical excitability and acetylcholine sensitivity of a rat pheochromocytoma cell line," Nature **268**(August) (1977).

153. J. Park et al., "Screening Fluorescent Voltage Indicators with Spontaneously Spiking HEK Cells," PLoS One **8**(12), Public Library of Science (2014) [doi:10.1371/journal.pone.0085221].

154. W. Haiss et al., "Determination of size and concentration of gold nanoparticles from UV-Vis spectra," Anal. Chem. **79**(11), 4215–4221 (2007) [doi:10.1021/ac0702084].

155. A. G. Kléber and Y. Rudy, "Basic mechanisms of cardiac impulse propagation and associated arrhythmias.," Physiol. Rev. **84**(2), 431–488, United States (2004) [doi:10.1152/physrev.00025.2003].

156. J. Yang et al., "Coupling optogenetic stimulation with NanoLuc-based luminescence (BRET) Ca++ sensing," Nat. Commun. **7**(1), 13268 (2016) [doi:10.1038/ncomms13268].

157. Y. K. Cho and G. Zheng, "Use of optogenetic technology in cell culture models Use of optogenetic technology in cell culture models," J. Phys., 0–4 (2016) [doi:10.1088/1742-6596/741/1/012067].

158. S. Johannsmeier et al., "Optical cell stimulation for neuronal excitation (Conference Presentation)," in Optogenetics and Optical Manipulation **10052**, S. K. Mohanty, N. V Thakor, and E. D. Jansen, Eds., p. 36, SPIE (2017) [doi:10.1117/12.2252017].

159. S. O. J. Ohannsmeier et al., "Light-cell interactions in depth-resolved optogenetics," Biomed. Opt. Express **11**(11), 6536–6550 (2020).

160. D.-W. Park et al., "Graphene-based carbon-layered electrode array technology for neural imaging and optogenetic applications," Nat. Commun. **5**(1), 5258 (2014) [doi:10.1038/ncomms6258].

161. W. Lee et al., “Transparent, conformable, active multielectrode array using organic electrochemical transistors,” Proc. Natl. Acad. Sci. **114**(40), 10554–10559, National Academy of Sciences (2017) [doi:10.1073/pnas.1703886114].

162. D. Smetters, A. Majewska, and R. Yuste, “Detecting Action Potentials in Neuronal Populations with Calcium Imaging,” Methods **18**(2), 215–221 (1999) [doi:https://doi.org/10.1006/meth.1999.0774].

163. O. L. AU - Barreto-Chang and R. E. AU - Dolmetsch, “Calcium Imaging of Cortical Neurons using Fura-2 AM,” JoVE(23), e1067, MyJoVE Corp (2009) [doi:doi:10.3791/1067].

164. J. H. Simpson and L. L. Looger, “Functional Imaging and Optogenetics in Drosophila,” Genet. Methods **208**(April), 1291–1309 (2018).

165. R. H. S. Westerink and A. G. Ewing, “The PC12 cell as model for neurosecretion,” Acta Physiol, 273–285 (2008) [doi:10.1111/j.1748-1716.2007.01805.x].

166. Z. Jia et al., “Stimulating cardiac muscle by light cardiac optogenetics by cell delivery,” Circ. Arrhythmia Electrophysiol. **4**(5), 753–760 (2011) [doi:10.1161/CIRCEP.111.964247].

167. D. Robertson and B. Paki, “Role of L-type Ca2+ channels in transmitter release from mammalian inner hair cells. II. Single-neuron activity.,” J. Neurophysiol. **87**(6), 2734–2740, United States (2002) [doi:10.1152/jn.2002.87.6.2734].

168. J. Platzer et al., “Congenital deafness and sinoatrial node dysfunction in mice lacking class D L-type Ca2+ channels.,” Cell **102**(1), 89–97, United States (2000) [doi:10.1016/s0092-8674(00)00013-1].

169. W. F. Sewell, “The relation between the endocochlear potential and spontaneous activity in auditory nerve fibres of the cat.,” J. Physiol. **347**, 685–696 (1984) [doi:10.1113/jphysiol.1984.sp015090].

170. L. P. Mark et al., “Pictorial review of glutamate excitotoxicity: Fundamental concepts for neuroimaging,” in American Journal of Neuroradiology **22**(10), pp. 1813–1824 (2001).

171. E. Hudry and L. H. Vandenberghe, “Therapeutic AAV Gene Transfer to the Nervous System: A Clinical Reality.,” Neuron **101**(5), 839–862, United States (2019)

[doi:10.1016/j.neuron.2019.02.017].

172. K. Willett and J. Bennett, “Immunology of AAV-Mediated Gene Transfer in the Eye.,” Front. Immunol. **4**, 261 (2013) [doi:10.3389/fimmu.2013.00261].

173. D. Ma et al., “Role of ER export signals in controlling surface potassium channel numbers.,” Science **291**(5502), 316–319, United States (2001) [doi:10.1126/science.291.5502.316].

174. C. Stockklausner et al., “A sequence motif responsible for ER export and surface expression of Kir2.0 inward rectifier K(+) channels.,” FEBS Lett. **493**(2–3), 129–133, England (2001) [doi:10.1016/s0014-5793(01)02286-4].

175. Y.-P. Zhang and T. G. Oertner, “Optical induction of synaptic plasticity using a light-sensitive channel.,” Nat. Methods **4**(2), 139–141, United States (2007) [doi:10.1038/nmeth988].

176. S. Senova et al., “Experimental assessment of the safety and potential efficacy of high irradiance photostimulation of brain tissues.,” Sci. Rep. **7**, 43997 (2017) [doi:10.1038/srep43997].

177. J. Duebel, K. Marazova, and J.-A. Sahel, “Optogenetics.,” Curr. Opin. Ophthalmol. **26**(3), 226–232 (2015) [doi:10.1097/ICU.0000000000000140].

178. A. Sengupta et al., “Red-shifted channelrhodopsin stimulation restores light responses in blind mice , macaque retina , and human retina,” EMBO Mol Med **8**(11) (2016).

179. C. R. Waqas M., *Approaches to Regenerate Hair Cell and Spiral Ganglion Neuron in the Inner Ear*, Springer, Cham (2020).

180. A. K. Wise et al., “Resprouting and survival of guinea pig cochlear neurons in response to the administration of the neurotrophins brain-derived neurotrophic factor and neurotrophin-3,” J. Comp. Neurol. **487**(2), 147–165 (2005) [doi:https://doi.org/10.1002/cne.20563].

181. L. N. Gillespie et al., “LIF is more potent than BDNF in promoting neurite outgrowth of mammalian auditory neurons in vitro,” Neuroreport **12**(2) (2001).

182. J. A. Engbring and H. K. Kleinman, “The basement membrane matrix in malignancy.,” J. Pathol. **200**(4), 465–470, England (2003) [doi:10.1002/path.1396].

183. P. E. Hall et al., “Laminin enhances the growth of human neural stem cells in defined culture media.,” BMC Neurosci. **9**, 71 (2008) [doi:10.1186/1471-2202-9-71].

184. H. K. Kleinman and G. R. Martin, “Matrigel: Basement membrane matrix with biological activity,” Semin. Cancer Biol. **15**(5), 378–386 (2005) [doi:https://doi.org/10.1016/j.semcancer.2005.05.004].

185. X. M. Xu et al., “Axonal regeneration into Schwann cell-seeded guidance channels grafted into transected adult rat spinal cord.,” J. Comp. Neurol. **351**(1), 145–160, United States (1995) [doi:10.1002/cne.903510113].

186. T. Asano, T. Ishizua, and H. Yawo, “Optically controlled contraction of photosensitive skeletal muscle cells.,” Biotechnol. Bioeng. **109**(1), 199–204, United States (2012) [doi:10.1002/bit.23285].

187. J. C. Schulze, “Structured cell growth on laser-generated patterns for optogenetic stimulation,” Leibniz University Hannover (2019).

188. S. S. Nunes et al., “Biowire : a new platform for maturation of human pluripotent stem cell derived cardiomyocytes,” Nat Methods **10**(8), 781–787 (2014) [doi:10.1038/nmeth.2524.Biowire].

189. N. Kondo et al., “Myoblast adhesion and proliferation on biodegradable polymer films with femtosecond laser-fabricated micro through-holes,” J. Biophotonics(February) (2020) [doi:10.1002/jbio.202000037].

190. P. Heeger, J. Harre, and A. Warnecke, “Probing interneuronal cell communication via optogenetic stimulation,” Transl. Biophotonics(February), 1–6 (2021) [doi:10.1002/tbio.202100002].

Curriculum vitae

Patrick Heeger, M.Sc.

Stenhusenstraße 25, 30625 Hannover

+49 177 4427849

heeger@iqo.uni-hannover .de

Personal Information

Date of birth	January16th, 1986
Place of Birth	Gehrden, Germany

Education

2014 – to date	**Leibniz University Hannover, Germany**
	PhD student in physics at the Institute for Quantum Optics
2012 – 2014	**University of Veterinary Medicine Hannover**
	Animal Biology and Biomedical Science
	Degree: Master of Science
2009 – 2012	**Technical University of Braunschweig**
	Undergraduate Studies in Biology
	Degree: Bachelor of Science

Work Experience

2019 – to date	CEO of Pasimo
2018 – 2020	Freeletics Coach at Leibniz University Hannover
2014 – to date	Scientific Employee of the State of Lower Saxony
2009 – 2013	Postman at Deutsche Post AG (part-time)

Declaration

Herewith, I confirm that I have written the present thesis myself and independently,

in accordance with the policy of Leibniz University Hannover § 6 Abs. 1 Promotionsordnung.

Parts of this thesis have already been published elsewhere[190].

_____

Hannover, 05 Juli 2021

Acknowledgements

First, I would like to thank my supervisor Alex for giving me the possibility to work at such an exciting interdisciplinary topic of biology and physics. My way of thinking changed a lot during the last years and to question things critically has become commonplace for me. Thank you for giving me the opportunity to grow up to be a real scientist!

A special thank you goes to my colleague Stefan, without you, this thesis would not have been possible! Also all the other NIFE colleagues who supported me either scientifically or with profound discussions in the coffee corner or the get-togethers – Thank you!

In addition, a big thank you to my collaboration partners around the group of Prof. Dr. med. Athanasia Warnecke. Especially Jenny and Jasmin for providing the rat puppies and the spiral ganglion neurons.

Thank you Prof. Dr. Anaclet Ngezahayo for teaching me how to patch-clamp and the general support in the first year of my PhD, I really enjoyed my time in your institute!

Dominik, I would like to thank you from the bottom of my heart for the time in our office! You have helped me countless times to bring light into the dark and to find my focus again! For me you have become an irreplaceable part of my life. Thank you so much for being my friend!

A person I would not want to miss anymore and who has helped me out of a mess countless times is Fiene. Thank you for always listening to me, no matter what nonsense I was talking about. I will never forget our time together #Lockdownbuddies.

Und zu guter Letzt möchte ich noch meinen Großeltern danken dafür, dass ihr immer für mich da seid. Diese Doktorarbeit habe ich in häufigen Gedanken an Euch erarbeitet. Ich bin sehr froh, dass es euch gibt!

- Von dem, was einer ist -